

ESTIMATING BIOLOGICAL CHANGES IN HUMAN BY DIFFERENT
MARKERS FROM RF EXPOSURE USING MODELING AND MEASUREMENTS

by

Niyazi Korkut Uluaydın

B.S., Electrical and Electronics Engineering, Boğaziçi University, 1995

M.S., Electrical and Electronics Engineering, Boğaziçi University, 1998

Submitted to the Institute of Graduate Studies in
Science and Engineering in partial fulfillment of
the requirements for the degree of
Doctor of Philosophy

Graduate Program in Electrical and Electronics Engineering
Boğaziçi University

2020

ACKNOWLEDGMENTS

I would like to thank to my Ph.D supervisor Prof. Selim Ş. Şeker for his guidance, his sincere help, and his perseverance in motivating me through out this thesis. He has given me rich perspectives on many obstacles I have met on the way, and only by his insights, I was able to pull through the hard times with my health and with my life.

I am thankful to my successor Ph.D supervisor Prof. Oğuzhan Çiçekođlu. His efforts were much appreciated especially in chaotic pandemic period when nothing was as before and he needed to double-check each and every procedure.

I would like to thank to the rest of my defense jury academicians who have provided precious feedbacks and comments to my Ph.D research. It was invaluable to sift through possible misunderstandings in my research before its finalization.

I am grateful to Prof. Taylan Kabalak (R.I.P) for his motivation and guidance in my interest in electromagnetic effects on intracranial endocrine glands. My friends, İbrahim Kolacı, Cahit Erdoğan, Mehmet Ali Ünver, Assoc. Prof. Fuat Karakaya have provided unprecedented support all through my Ph.D research. I would like to sincerely thank to everyone whom I have missed to mention who has supported me in this period.

And finally, I am grateful to my family, my mother, Suzan Uluaydın, my father, Ali Turgay Uluaydın, and my brother, Burak Uluaydın, who have supported me when I had almost fully collapsed with health problems. With their love, support, and motivation, I was able to recover back and complete my Ph.D journey.

ABSTRACT

ESTIMATING BIOLOGICAL CHANGES IN HUMAN BY DIFFERENT MARKERS FROM RF EXPOSURE USING MODELING AND MEASUREMENTS

This thesis dissertation reviews the works of academia on natural occurring electrical, magnetic, and electromagnetic (EM) phenomena and their subtle relations with living organisms. It also investigates the artificial electromagnetic waves from different generations of mobile technology radio frequency (RF) exposure with their possible paths of impact.

It proposes new scenarios of mobile technology usage through finite element method (FEM) simulations with new radio possibilities of mobile terminals and base stations in view of new antenna technologies. The model theoretical limitations are cross-checked by Mie Theory. The FEM simulations are first time oriented according to organ specific effect investigations in IEEE SAM phantom model. The simulations are also improved in terms of organ details such as eye-based ones with detailed initial conditions. This dissertation also first time projects the known EM effects on salivary glands by biological markers over hypothalamus-pituitary-adrenal (HPA) axis and pineal glands, which are similar in biological and electrical properties and cannot be studied without invasive methods. This is a solid non-thermal effect proposition on the homeostasis of human beings.

This dissertation proposes a detailed measurement of the multi-operator multi-technology urban base stations with spectrum and antenna aware methodology. Combining this with the statistics of mobile radio network maintenance activities with their periodicity and duration, which have never been reported before in academia, it provides a totally different perspective for occupational RF exposure and increased risks. Result of both probable non-thermal and thermal risks are clear findings new to the academia.

ÖZET

İNSANDA RADYO SIKLIK MARUZİYETİ KAYNAKLI BİYOLOJİK DEĞİŞİKLİKLERİN MODEL VE ÖLÇÜMLER KULLANILARAK FARKLI BELİRTEÇLERLE TAHMİN EDİLMESİ

Bu tez, akademinin doğal oluşan elektrik, manyetik ve elektromanyetik (EM) olaylar ve bunların canlı organizmalarla ince ilişkileri üzerine çalışmalarını gözden geçirir. Buna ek olarak, farklı nesil mobil teknoloji radyo frekansı (RF) maruziyetinden gelen yapay elektromanyetik dalgaları, olası etki yollarını araştırır.

Yeni anten teknolojilerini, mobil terminallerin ve baz istasyonlarının yeni radyo olanaklarını göz önünde bulundurularak mobil teknoloji kullanımının yeni senaryolarını sonlu elemanlar yöntemi (FEM) simülasyonları üzerinden inceler. Modelin teorik sınırlamalarını Mie Teorisi üzerinden çapraz kontrol eder. IEEE SAM fantom modelinde ilk kez organa özgü etki araştırmalar için FEM simülasyonları kurgulanmıştır. Simülasyonlar, göz örneğinde olduğu gibi organ detayları açısından ilk kez ayrıntılı başlangıç koşulları ile de geliştirilmiştir. Bu tezde tükürük bezleri üzerindeki biyolojik belirteçler aracılığıyla bilinen EM etkileri de ilk kez, biyolojik ve elektriksel özelliklerde benzer olan ve müdahalesel yöntemler olmadan çalışılmayan hipotalamus-hipofiz-adrenal (HPA) eksenini ve epifiz bezleri üzerine yansıtılmıştır. Bu, insanların sağlamlığı (homeostasis) üzerinde ciddi bir ısısal-olmayan etki önermesidir.

Bu tez, ayrıca çok operatörlü çok teknoloji kentsel baz istasyonlarının spektrum ve anten farkındalık metodolojisi ile ayrıntılı bir ölçümünü önermektedir. Bunu, mobil telsiz şebekesi bakım faaliyetlerinin istatistikleriyle birleştirerek, akademik çevrelerde daha evvel hiç rapor edilmemiş periyotları ve süreleri ile birleştirerek mesleki RF maruziyet ve artan riskler için bambaşka bir bakış açısı sağlar. Hem ısısal-olmayan hem de ısısal risklerin olası sonuçları, akademik çevreler için yeni olduğu kesin bulgulardır.

TABLE OF CONTENTS

ACKNOWLEDGEMENTS	ii
ABSTRACT	iii
ÖZET	iv
LIST OF FIGURES	vii
LIST OF TABLES	xii
LIST OF SYMBOLS/ABBREVIATIONS	xiii
1. INTRODUCTION	1
1.1. Research Path and Contributions	4
1.2. Thesis Outline	4
2. NATURAL OCCURRING EM PHENOMENA	6
2.1. Geomagnetic Field	6
2.2. Schumann Resonances	7
2.3. Solar Irradiation	7
2.4. Atmospheric Electricity and Telluric Currents	8
3. BIOELECTROMAGNETISM IN HUMAN	10
3.1. Electrical Properties of Cells	10
3.2. Bioelectrical Fields	11
3.3. Biomagnetic Fields	12
4. ARTIFICIAL EM SOURCES	15
4.1. Spectrum Components of UE and BS	16
5. OVERVIEW OF ELECTROMAGNETIC THEORY FOR BIOELECTROMAGNETISM ..	21
5.1. Maxwell's Equations	21
5.2. Homogeneous Vector Wave Equations	22
5.3. Reciprocity	22
5.4. Modeling the Problem with Finite Element Method	24
5.5. Finite Element Method	27
5.6. FEM versus FDM Comparison	30
5.7. Mie Theory – Multilayer Spherical Dielectric Model	33
6. UE SIMULATIONS AND BS FIELD MEASUREMENTS	38
6.1. Multilayer Brain Model	38
6.2. Human Head Model and Tissue Parameters	41
6.3. Multi-Radio Supporting UE Simulation – Nominal	43
6.4. Multi-Radio Supporting UE Simulation – across Face	47

- 6.5. Base Station EM Exposure Measurements 52
- 6.6. Occupational EM Exposure Risks in BS Maintenance 55
- 7. ORGAN SPECIFIC SIMULATIONS 58
 - 7.1. Multi-Radio Supporting UE Simulation – with Eyes 60
 - 7.2. Conventional Mobile Call’s Effect on HPA Axis 70
 - 7.3. Tumor Detection Possibility by UE Born EM 74
- 8. DISCUSSION OF RESULTS AND CONCLUSIONS 80
 - 8.1. Contributions 81
 - 8.2. Future Path 82
- REFERENCES 83

LIST OF FIGURES

Figure 4.1. (a) A combo antenna hosting 4 pairs of X-pol antennas namely red pair 710-960 MHz, blue pair 1710-2170 MHz and yellow pairs on both sides 1710-2690 MHz; (b) two of combo antennas operating in multiband configuration.....	20
Figure 5.1. Taxonomy of Bioelectromagnetism [61]	23
Figure 5.2. Theoretical view to define the subdivisions of bioelectromagnetism [61]	24
Figure 5.3. Visualization of the problem	25
Figure 5.4. Difference between FEM and FDM in simulation	28
Figure 5.5. Geometry, loads and finite element meshes	29
Figure 5.6. Difference between FEM and FDM in simulation	30
Figure 5.7. FEM supports non-coincident meshes	31
Figure 5.8. FEM defines complex geometries better	31
Figure 5.9. Example of FEM utilized in human skull [65]	32
Figure 5.10. A representation of human head with 6 layers	34
Figure 5.11. Our representation of human head model with 6 layers	34
Figure 5.12. Our representation of human head model in domain view	35
Figure 6.1. Wave direction in our model, TE x-y plane with pitch 90 degrees	38
Figure 6.2. Far field norm showing the bias of the rod orientation (Left to right and down in the sequence of height-radius of cylinder: 18-4; 16-4; 16-2; 12-2; 10-0.5;6-1)	39

Figure 6.3. Far field electrical field value showing the degree of the rod orientation (Left right and down in the sequence of height-radius of cylinder: 18-4; 16-4; 16-2; 12-2; 10-0.5; 6-1)	40
Figure 6.4. Far field 3D electrical norm of the 10-degree orientation rod 18-4	41
Figure 6.5. All simulations using the same MRI deducted brain tissue property interpolation [75]	43
Figure 6.6. First CDR simulation with blue biological tissue SAM relative to concurrent radios' position	44
Figure 6.7. First CDR simulation heat distribution on SAM over 60 minutes	44
Figure 6.8. First CDR simulation heat distribution on SAM in iso-surface representation	45
Figure 6.9. First CDR simulation's 1 st radio source born electric field norm in multi-slice representation	45
Figure 6.10. First CDR simulation's 2 nd radio source born electric field norm in multi-slice representation	46
Figure 6.11. Second CDR simulation with blue biological tissue SAM relative to concurrent radio position	48
Figure 6.12. Second simulation FEM mesh structure	48
Figure 6.13. Second CDR simulation's heat effect by 800 MHz radio born electric field norm at 25 cm	49
Figure 6.14. Second CDR simulation's heat effect by 900 MHz radio born electric field norm at 25 cm	49
Figure 6.15. Second CDR simulation's heat effect by 1800 MHz radio born electric field norm at 25 cm	50

Figure 6.16. Second CDR simulation's heat effect by 2100 MHz radio born electric field norm at 25 cm	50
Figure 6.17. Second CDR simulation's heat effect by 2600 MHz radio born electric field norm at 25 cm	51
Figure 6.18. Second CDR simulation heat distribution with 800 MHz radio at 5 cm distance from UE	51
Figure 6.19. Second CDR simulation heat distribution with 800 MHz radio at 5 cm distance from UE with iso-surface representation	52
Figure 6.20. The antenna measurement approach	53
Figure 6.21. The bird's view roof-top sketch with measurements in a site	54
Figure 6.22. The spectrum analyzer output in a site	54
Figure 6.23. A multi-operator multi-technology site	55
Figure 7.1. An oblique view to the 3D eye model used [71]	58
Figure 7.2. Third CDR simulation with 5cm distance radio sources and eyes in the phantom ..	61
Figure 7.3. Third CDR simulation sclera conductivity of the phantom with frequency	62
Figure 7.4. Third CDR simulation sclera permittivity of the phantom with frequency	62
Figure 7.5. Third CDR simulation temperature plot with concurrent 2450 and 2600 MHz sources	63
Figure 7.6. Third CDR simulation isosurface temperature plot with concurrent 2450 and 2600 MHz sources	63
Figure 7.7. Fourth CDR simulation isosurface temperature plot with concurrent 800 and	

2600 MHz sources with transparent view of face and eye domains	64
Figure 7.8. Fifth CDR simulation surface temperature plot with concurrent 800 and 2600 MHz sources of face and eye domains	64
Figure 7.9. Sixth CDR simulation translucent temperature plot with concurrent 800 and 2600 MHz sources of face and eye domains	65
Figure 7.10. Seventh CDR simulation translucent temperature plot with concurrent 2450 and 2600 MHz sources of face and eye domains	66
Figure 7.11. Eighth CDR simulation temperature plot with concurrent 2450 and 2600 MHz sources of eye domain with oblique antenna exposure	66
Figure 7.12. Temperature rise plot in human eye modelled as vitreous humour tissue exposed to 2600 MHz-2450 MHz EM sources at varying distances with centralized antennas	67
Figure 7.13. Temperature rise plot in human eye modelled as vitreous humour tissue exposed to 2600 MHz-2450 MHz EM sources at varying distances with side antennas	67
Figure 7.14. Transparent top-down view temperature rise plot in human eye as vitreous humour tissue exposed to 2600 MHz-2450 MHz EM sources on side at 3 cm	68
Figure 7.15. Side-view 25 slice iso-surface temperature rise plot in human eye as vitreous humour tissue exposed to 2600 MHz-2450 MHz EM sources on side at 3 cm	68
Figure 7.16. Logarithmic SAR values on x-y plane with $z=2.5$ cm by 2600 MHz-2450 MHz CDR with central antennas at 5 cm distance	69
Figure 7.17. Simulation model with conventional call position	70
Figure 7.18. Temperature elevation recordings from simulations	72
Figure 7.19. Electric field strength recordings from simulations	72

Figure 7.20. Logarithmic SAR recordings from simulations	73
Figure 7.21. Temperature elevation (K) in HP, pineal and salivary glands at 900 MHz	73
Figure 7.22. Modified IEEE SAR model with GBM tumor	76
Figure 7.23. Tissue temperature elevations with changing tumor depth at lower power EM exposure	76
Figure 7.24. Tissue temperature elevations with changing tumor depth at higher power EM exposure	77
Figure 7.25. Temperature elevation comparison with tumor above and without tumor below at higher power EM exposure	77
Figure 7.26. Breast model with tumor	78
Figure 7.27. Temperature elevation comparison in breast with tumor with higher power (above) and lower power (below) EM exposure	78

LIST OF TABLES

Table 6.1.	First CDR simulation's parameter set	46
Table 6.2.	Urban roof-top fault recovery and maintenance statistics	56
Table 7.1.	Tissue Conductivity Values (S/m)	59
Table 7.2.	Tissue Relative Permittivity Values	59

LIST OF SYMBOLS/ABBREVIATIONS

1D	One dimensional
3D	Three dimensional
2G	Second generation
3G	Third generation
4G	Fourth generation
5G	Fifth generation
B	Magnetic flux density vector
B	Blood perfusion coefficient
c	Specific heat capacity
D	Electric flux density vector
E	Electric field intensity vector
E_i	Incident electric field
E_r	Reflected electric field
E_t	Transmitted electric field
f	Frequency
H	Magnetic field intensity vector
Im	Imaginary function
j	Imaginary unit
J	Electric current density vector
K	Stiffness matrix
k_o	Wave number
m	Refractive index
M	Magnetic current density vector
Q_a	Absorption efficiency factor
Q_{met}	Metabolic heat generation rate
Q_s	Scattering efficiency factor
Q_t	Total efficiency factor
R	Reflection coefficient
Re	Real function
T	Thickness
x	Size parameter
∇^2	Laplace operator

∇	Gradient
$\nabla \cdot$	Divergence
$\nabla \times$	Curl
β	Blood perfusion coefficient
ϵ	Permittivity
ϵ_r	Relative permittivity
λ	Wavelength
μ	Permeability
μ_r	Relative permeability
ρ	Material density
ρ_c	Charge density
σ	Electric conductivity
ω	Blood perfusion rate
AC	Alternating Current
BBB	Blood Brain Barrier
BC	Boundary Condition
BEM	Boundary Element Method
BS	Base Station
BTB	Blood Tumor Barrier
CA	Carrier Aggregation
CAD	Computer Aided Design
CAPEX	Capital Expenditure
CDR	Concurrent Double Radio
COVID-19	Corona Virus Disease-2019
CSF	Cerebrospinal Fluid
DC	Direct Current
DUT	Device Under the Test
ECG	Electrocardiography
EEG	Electroencephalography
ELF	Extremely Low Frequency
EM	Electromagnetic
EMF	Electromagnetic Field
EMR	Electromagnetic Radiation
FCC	Federal Communications Commission
FDD	Frequency Division Duplexing
FDM	Finite Difference Method

FDTD	Finite Difference Time Domain
FEM	Finite Element Method
FIT	Finite Integration Technique
FVM	Finite Volume Method
GBM	Glioblastoma Multiforme
HbA1c	Glycated Hemoglobin
HPA	Hypothalamus-Pituitary-Adrenal (Axis)
ICNIRP	International Commission on Non-Ionizing Radiation Protection
ICR	Ion Cyclotron Resonance
IoT	Internet of Things
ISM	Industrial Scientific Medical (band)
LEO	Low Earth Orbit
LTE	Long Term Evolution
MCG	Magnetocardiography
MEG	Magnetoencephalography
MIMO	Multiple Input Multiple Output
MNO	Mobile Network Operator
MoM	Method of Moments
MRI	Magnetic Resonance Imaging
MRN	Mobile Radio Network
MS	Multiple Sclerosis
MT	Mobile Terminal
MW	Microwave
OFDMA	Orthogonal Frequency Division Multiple Access
OPEX	Operating Expenditure
PAPR	Peak to Average Power Ratio
PDE	Partial Differential Equation
pH	Power of Hydrogen
RADAR	Radio Detection and Ranging
RF	Radio Frequency
SAM	Specific Anthropomorphic Mannequin
SAR	Specific Absorption Rate
SC-OFDMA	Single Carrier - Orthogonal Frequency Division Multiple Access
SLF	Super Low Frequency
SQUID	Superconducting Quantum Interference Device
TDD	Time Division Duplexing

TTI	Transmit Time Interval
UE	Mobile User Equipment
ULF	Ultra Low Frequency
UMTS	Universal Mobile Telecommunications System
VLF	Very Low Frequency
WCDMA	Wide-band Code Division Multiple Access
WI-FI	Wireless Fidelity
WLAN	Wireless Local Area Network

1. INTRODUCTION

The most massive change among all the other changes that human kind has made in his environment through technology is the global electromagnetic (EM) environment that we live in today. Compared to other technology driven changes, the global EM environment has been so abruptly changed in such a short time without any second thought and any solid evidence that we do not still know the total possible span of the harmful effects of this alteration today. Secondly, the volume of this change is so devastating that it is totally incomparable with any of the other alternations in our environment in human history. It also spans areas, where natural EM frequencies have never existed before in our natural environment. Last but maybe the most important of all is that there is no way to sense or feel any of the EM waves and fields and observe their effects over us in a controlled manner by ourselves.

EM fields and waves have flooded all around us with ever increasing amounts with the spread of power grid network and wireless technology boom. Especially, wireless revolution in telecommunications has made huge contributions to the sea of EM waves, more and more in last three decades. Currently, we are at the dawn of 5th generation wireless services, where higher frequency spectrum will be used in a broader bandwidth-sense and with spatial modulations and with probable subtle effects on molecules such as oxygen O₂ our lives primarily depend on. In the meantime, the vertical wireless services through low earth orbit (LEO) satellites are also in deployment process.

With Internet of Things (IoT), sensors, controllers, devices and other machines are joining the ranks of communication service users with their increasing contributions. When all these changes are compared to the natural occurring EM waves and fields with their comparatively minute amounts, human kind has never played such a gamble in any of the external factors in his environment in such a short period of time taking into consideration of long adaptation of our own species.

Artificial EM exposure has generally been observed to have stimulating effects on organisms in its initial stage; while as the exposure time prolongs, it becomes a stress factor and a disrupting one. To understand negative effects of any external factor, the medical science utilizes many markers such as heat regulation parameters, blood circulation, blood parameters (pH, sugar level, hemoglobin counts, O₂, CO₂, and other molecular compositions, etc.), urinary chemistry, content, and conductivity analysis, endocrine response changes (especially hypothalamic-pituitary-adrenal (HPA) axis), and many others. These markers can be of the primary nature where the mechanism (cause) is directly affecting the marker itself such that injecting insulin into vein will decrease plasma blood sugar level (effect) by making cells absorb glucose from blood. Or it could be of a secondary nature when the higher blood sugar content makes the hemoglobin born iron comprising molecule to oxidize faster. HbA1c (glycated hemoglobin) is a form of hemoglobin used to measure the average plasma glucose concentration over prolonged periods of time. If the plasma glucose level increases, the oxidation rate of the glycated hemoglobin also linearly elevates. Since the normalization process of glycated hemoglobin to its nominal level takes long time, it serves as a marker for average blood glucose levels for the former months. There could be tertiary nature markers where the cause-effect relations can only be retrieved over long periods of time and in a statistically safe way. Changes in electroencephalogram (EEG), magnetoencephalogram (MEG), electrocardiography (ECG), magnetocardiography (MCG), nerve firing rate values and so on, are such examples where a certain cause, for example, a long duration phone usage triggers an effect on EEG and other bodily functions [1]. But it is not necessarily sufficient to prove this effect to be able to cause health related issues, in return.

To measure the electromagnetic radiation (EMR) exposure certain models have been developed. The physical models approximate the EMR effects of a subject source such as a mobile terminal (MT) over a biological target such as a human head by making use of saline solutions mimicking the biological tissue in the shape, and the usage in the form, respectively. Similarly, there are also simulation models such as IEEE phantom Specific Absorption Rate (SAR) head used by computational electromagnetics. The computational approach is not only used for double-check purposes against mistakes that can be done with physical models, but also provide insights for effects which cannot be studied in biological tissues without invasive methods. Different approaches such as Finite Difference Time Domain (FDTD) by Yee [2], Method of Moments (MoM) by Harrington [3], Finite

Integration Technique by Wieland [4], Finite Element Method (FEM) by Courant [5] or hybrid techniques may be used in simulations for projecting the behavior of Maxwell's equations in terms of partial differential equations (PDEs). PDEs are instrumental in solving analytically complex problems. FEM will be our choice in this thesis with its inherent advantages over complex structures.

EM exposure and its effects on health issues for the above reasons have not been an easy quest. The statistical approaches with epidemiological nature fail to isolate the other factors in an acceptable fashion. Even if we assume they do, since they are the derivative conclusions of the derivative results, they fail to convince all the stakeholders. And if the stakeholders are in conflict of interest with the probable outcomes, there can be scientifically tuned bias towards outcomes [6]. Secondly, the current scientific paradigm does not encourage an all occupying research methodology, which will be too expensive and too much time taking for EM related effects to be shown with all aspects. Instead, the incremental progress is much preferred over former accumulated research. This approach may have some drawbacks, too; for too much reductionism literally blocks any kind of deduction on a larger scale. Last but not the least, accuracy of measurement is a primary problem in EMR metrology. EMR is generally beyond organoleptic awareness, and requires specialized devices for its detection and measurement. Alas, these EMR measurements are still one of the least accurate among all physical measurements because of human factor in measurement process in terms of human errors such as near field far field misinterpretations, as well as, in terms of affecting the measured values by physically being there [7-10].

EM exposure related effects have been taken from thermal-only factor point of view for over 50 years in public health care standards. But with the advent of mobile telecommunication networks, both exposure and its domain have reached almost everyone and everywhere. The initial power outputs of mobile terminals of 10 Watts (W) have gradually decreased to 2 W, and then down to 0.8 W; and, the thermal effects became mostly negligible. Even over long phone conversations, the temperature increase was only limited to a few sub-degrees and it was mostly regulated by the ambient temperature gradient and by the body's own heat regulating mechanisms. As the research continued, certain other mechanisms affecting metabolism's circadian rhythm, stress response, endocrine fluctuations, intra/inter-organ communication effects, and cell-based responses such as ion

pump impacts and membrane leakages were found. But all those findings are not enough to make any deduction on a greater scale for public health protection.

Maybe, it is time to look for the answers from a different perspective.

1.1. Research Path and Contributions

This study seeks to find new approaches to estimate the possible biological effects of the rapid expansion of EM usage in many fields but especially in telecommunications by different markers. Natural occurring EM phenomena has shown to have subtle effects on our planet's biosphere and life on earth with their miniscule amounts [11-26]. Similarly, bioelectromagnetism in humans is a research field with many interesting areas to be explored [1, 27-43].

This study focuses on the telecommunications equipment, which has the greatest impact on humans in terms of exposed time EM radiation, both in terms of user equipment (UE) and base stations (BS). UEs with their latest morphosis the smartphones (SP) are like a digital organ added to our lives. On the BS side of the coin, multi-technology, multi-operator urban co-sited BSs are the apex of the EM radiation effect for most of the population [10]. Therefore, this study provides empirical data from field as well as derived data from computer EM simulations and uses them to estimate the possible outcomes, occupational or personal, on specific human organs and systems by modifying the IEEE SAR phantom head model for different exposure scenarios in light of the most recent findings of the academia.

The study includes first time introduction of multi-physics simulation of two concurrent EM FEM studies. It also expands the known EM non-thermal effects on salivary glands by means of simulation based derived values onto HPA axis and pineal glands, which could not be studied without invasive methods.

1.2. Thesis Outline

The rest of the thesis is organized as follows: In Chapter 2, natural occurring EM phenomena will be reviewed. This will provide a brief look at the naturally occurring EM

fields and waves and their subtle relations with the living organisms. Then in Chapter 3, we will carry on with the bioelectromagnetism in human beings. We will look for the connections on both naturally occurring and artificial EM waves and fields with human health, top-down and bottom-up, respectively. And in chapter 4, we will have a look at how new technologies pull us further into the depths of this human-made EM ocean. This chapter will cover both the base station and the mobile terminal side along the different mobile technology generations with the possible paths of their EM impacts.

Chapter 5 is dedicated to the Electromagnetic Theory and its utilization in bioelectromagnetism. Mie Theory is visited for multi-sphere tissue model approach. Then, Finite Element Method is explained for solving EM exposure over biological tissue with its advantages. Chapter 6 includes both user equipment and base station simulations and measurements, respectively. Concurrent double radio based simulations for different user equipment positions are shown followed by field measurements of urban base station environment. Chapter 7 contains the new approach to simulations in light of the new measurements and findings of the academia. And finally, Chapter 8 has the overall discussions and conclusions.

2. NATURAL OCCURRING EM PHENOMENA

There are many naturally occurring electromagnetic (EM) phenomena in our environment. Firstly, we live in the geomagnetic field of earth. The geomagnetic field acts as a shield against high energy charged particles from the sun. Although human beings are aware of the geomagnetic field for a long time, we were not knowledgeable of the geomagnetic field's profound and subtle effects on living beings until recent times.

2.1. Geomagnetic Field

Certain animal species such as birds use the geomagnetic field to arrive in their breeding grounds during seasonal migrations. Birds often use polarized light for their navigation, and they may also develop a visual map sense in addition to it. Bird species that migrate at night use the stars as a compass for the north-south orientation. Among the birds, pigeons have another back-up navigation system. They can navigate even in cloudy weather without polarized light and without visual map sense. Through tiny particles of magnetite crystals in their head, they use the earth's magnetic field to locate their approximate positions even in weathers with no clear visibility. The earth's magnetic field is stronger at the poles. It weakens in the direction of the equator. Accordingly, a bird may be able to follow its latitude by the strength of the geomagnetic field. The changes are miniscule in strength along a path, but homing pigeons show signs to reach the sensitivity to detect even these tiny changes [11].

Other species such as bees, sea mammals and ruminants also orient themselves using the geomagnetic field. We know it by the strong correlation of geomagnetic disturbances and storms with the whales running aground [12], as well as, by extremely low artificial alternating current (AC) magnetic fields' disruption of the ruminants north-south alignment at rest [13, 14, 15].

Geomagnetic field has a strong direct current (DC) component and a weaker alternating current (AC) component between 5 Hz and 20 Hz. There are also tidal

fluctuations on the geomagnetic field triggered by the moon [16]. These fluctuations can be detected by the living organisms, and they work as a clock signal for lunar day. Moreover, the moon is considered to play a critical role on the sustainability of the geomagnetic field [17]. The same geomagnetic field also gives birth to the magnetosphere, which protects all living beings on earth from solar wind comprising high energy particles. The magnetosphere is affected by the solar anomalies, too. All in all, the sun, the earth, and the moon have an interwoven life-sustaining relation. Now, let us investigate how this is related to human homeostasis.

2.2. Schumann Resonances

Professor Dr. W.O. Schumann, the German physicist of the Technical University of Munich, has predicted that there could have been electromagnetic standing waves in the atmosphere, in the cavity between the ionosphere and the earth [18]. Then, he and his students have calculated the frequency of these waves as 10 Hz. Dr. Schumann and his student Dr. König have later observed these resonances in their experimental set-up, where conductive spheres have been isolated by air, at a main frequency range of 7.8-10 Hz [19].

Electrical discharges such as thunder, excite and proceed within the cavity between the ionosphere and the earth. The low frequency component of electrical discharges induces EM waves spanning from the extremely low frequency (ELF) to the very low frequency (VLF) range, which form standing waves within the cavity with a frequency of about 7.8-10 Hz traveling in free space [20]. Interestingly, this range of frequencies is common in EEG of all animals beyond a certain encephalization. Human beings are differentiated from lower animals by having the peak at 7.8-10 Hz components in EEG as a higher form of life.

2.3. Solar Irradiation

Solar irradiation is the main energy source of the life and the main element of the total cycle of energy that everything depends solely on. The solar daily cycle is the base for biological slow rhythm. The rotation of earth and the solar irradiation forms the daily rhythm called circadian. The organisms, whose lives mainly depend on the sun such as plants, primarily use circadian rhythm. Organisms, whose lives depend on the tidal movement,

sense the lunar cycles. The experiments on human daily rhythm have interestingly shown it to be closer to one lunar day (24 hours 50 minutes) [21]. Thus, the human sleep cycle is rather associated with planetary daily cycle while human menstrual cycle is rather associated with lunar monthly cycle. Therefore, both solar irradiation and lunar activity directly affect the circadian rhythms and the human endocrine secretions. Similarly, diurnal variations in Schumann resonances are directly related with solar irradiation.

There is a high degree of correlation between the solar flux and the sunspot observations [22]. Similarly, the sunspot observations are negatively correlated with the geomagnetic field. An increase in cosmic rays has a negative correlation with the Schumann resonance power. It is interesting to note that the solar power fluctuations are interrelated with human heart rate variability and blood pressure changes directly or indirectly through changing geomagnetic activity [22, 23]. The geomagnetic field is directly under the effect of the solar irradiation factors and it is also fluctuating with the lunar tidal pattern [22]. The father of heliobiology, Alexander Tchijevsky, had claimed the 11-year sun spot peak activity and human mass excitability, which a term he coined to define historical events hosting mass people involvement, to be interrelated by means of negative ionization in the atmosphere. These 11-year cycles form an alternating cosmic ray cycle of 22 years, which is called Hale cycle. Verily, the solar irradiation seems to have subtle effects over human parasympathetic system, and intricate impact on the overall geomagnetic field.

2.4. Atmospheric Electricity and Telluric Currents

The cosmic ray from cosmos and mainly from sun with positive high energy particles shower earth, which is inherently negative. The ionosphere is charged positive relative to earth. Thus, there is constant electric current from sky to earth. There are also electrical currents thought to be caused by the earthquakes and transmigrating energy flow between the mantle and the crust flowing in the earth called telluric currents. This is discharged from time to time depending on the earth properties, humidity, voltage difference between the sky and the subject ground by means of thunderstorms. The effect of the electrical mechanisms of the sky and of the earth on weather and hurricanes is an interesting topic [24]. There are also studies on the relation of the atmospheric electricity difference and multiple sclerosis [25, 26].

The naturally occurring EM phenomena is densely interwoven with the life itself. A variety of living organisms from single cellular oceanic bacteria to fruit flies, from potato to cattle, and finally the most advanced organisms, the human beings, were found to exhibit subtle responses to these cyclic events with minute amounts of electromagnetism. Most of the time, this is vital for their very existence.

Now then let us continue with bioelectromagnetism in human beings.

3. BIOELECTROMAGNETISM IN HUMANS

In the early 20th century, the doctrine of *Wissenschaftliches Medicine* has become the dominant paradigm in western medical science and has utterly promoted the focus on physiochemical interactions in the human body with a mechanistic point of view. This in turn, has dramatically decreased the studies on the electrical and magnetic components of human biology finishing the vitalism versus mechanistic discussion. Later, Albert Szent-Gyorgyi believed that just the biochemistry alone was not sufficient to explain cellular life since cell should have inherited a mechanism to regulate biochemistry by means of electricity and magnetism. He has first time proposed the biological semi-conduction currents over the known ionic ones in 1944. Similarly, Dr. Aleksandr Pressman has proven interactions of electromagnetic fields and living organisms [27]. Altogether, Tchijevsky, Gyorgyi, and Pressman have established the electromagnetic alignment of mechanisms from macro cosmos down to their effects on life processes on the earth's biosphere. With reciprocity, one can deduct living organisms use electromagnetic interactions for information transfer, organization, restoration, and growth control. So, this requires the cell to have mechanisms to sense, store, and flow this form of energy in its basic form, electricity. Even water alone, which the body of an adult consist of around 60%, has changing properties depending on its electrical charge and potential according to a recent study [28].

3.1. Electrical Properties of Cells

The human cells have two-layer membrane structure. This membrane has positive charge outside and negative charge inside with an average membrane potential of -70 mV making the cell interior negative with a range potential of -30 mV to -90 mV. The cell membrane has positive and negative ion channels such as calcium and potassium channels built-in as well as ion pumps such as sodium-potassium pump. These ion channels and ion pumps help cell metabolism synthesize required energy and other biological processes by inflow and outflow of ions arranging the necessary electro-bio-chemical medium both by active and passive processes. The changes in the membrane potentials because of an anomaly may trigger influx-outflux of ions changing the chemical structure inside the cell as well as

outside in the tissue in terms of chemical changes such as power of Hydrogen (pH) [29]. Similarly, such changes in pH and in membrane resting potentials can also be used to detect the illnesses such as cancer [30, 31, 32]. It is equally important to note now that the cell membrane potential, ion channels, ion pumps, cell interior proteins are prone to the effects of electrostatic, electrical, and electromagnetic exterior effects [32, 33]. For example, protein calmodulin has an internal jitter in the MHz range, by which it is easy to deduct that it can be entrained with a similar frequency, externally [34]. Therefore, a thermal-only effect approach is obviously inadequate in EM radiation studies on biological matter.

3.2. Bioelectrical Fields

There are different charge carrying mechanism in the human body. The first found conduction mechanism is the ion conduction. Neurons' transferring electric information through axon by a mechanism called *action potential* is of this type. Action potential ripple is achieved by polarizing the cell membrane by active ion channel pumps. A quick depolarization triggers a chain depolarization forming a wave of opposite polarity as a message moving along the axon and transferring the necessary information of related type: sensory or motor. Then the cells repolarize themselves to their nominal resting potentials.

The second charge carrying mechanism in the human body is of semi-conducting nature. There is a DC current flowing through nerve fibers. This perineural current is also one of the mechanisms that form the voltage gradient between cells for intercellular communication together with action potentials [35, 36]. The polarity in the head is positive relative to limbs. The current flows from brain to the body through motor nerves and this circuit is completed through sensory nerves back to brain. Physical activity increases the voltage difference as if it is charging the bio-battery, whereas sleep decreases it and anesthesia neutralizes it or may even reverse the polarity.

The cell membrane potentials are critical for cell proliferation, migration, differentiation, and dedifferentiation (as in wound regeneration). If a wound is inflicted on the body, the damaged cells leak their ions causing a short-circuit, which reverses the polarity of the area in the DC circuit. This voltage is critical in wound healing and regeneration. And with the lack of this positive voltage healing is halted.

The cell transmembrane potentials, the currents, polarities, voltages, and voltage gradients in the body are the research and the application area of the electro-medicine: electroceuticals. These conditions can be changed electrically or non-electrically. For the electrical example, by applying 0.9 V over non-healing bone fracture wounds positive on the wound and negative on its counter side, it is possible to restart and stimulate bone healing. For non-electrical example, by using transmembrane potentiators such a *tricide* or *lyserin*, which alters the transmembrane potential of bacteria by altering ion-protein bridging, it is possible to penetrate the antibiotics into the glycocalyx shielded penicillin resistant bacteria. It is equally possible to change transmembrane potentials of tumor cells selectively to use chemotherapy in target-oriented manner while minimizing the collateral damage on healthy cells from side effects [32].

3.3. Biomagnetic Fields

The human magnetic fields could only be detected with the advent of very sensitive magnetometers such as superconducting quantum interference device (SQUID). The DC currents in the brain, in the perineural system, and in the heart generate their own magnetic fields by Ampere's law.

The heart has a special role among the other organs. It provides a continuous periodic signal to the whole body in terms of magnetic, electrical, motion, sound, heat, and light. Blood is the main conductor of these signals to the body. Since blood is also a good electrical conductor, the heart entrains the whole body with electrical and magnetic pulses. The semiconducting nature of perineural DC currents are sensitive to external magnetic fields.

The brain is also found to have magnetic properties but much weaker compared to the heart. SQUID and similar very sensitive magnetometers can make magnetic measurements in the brain called magnetoencephalography. This measurement provides information about the overall electrical and magnetic activity in the brain.

There is a molecule called neuromelanin in the brain. This molecule has the highest ratio in humans compared to other primates like the encephalization factor. Neuromelanin chelates iron and serves as iron depot. Interestingly, it shows anti-magnetic properties in big

grains, whereas it is superparamagnetic in small grains [37]. It has been found that the superparamagnetic small grains are less in size and number on Parkinson's disease [37]. Let us note that neuromelanin also exists in the eye and in the ear for optical shielding and acoustic absorption purposes, respectively [38].

Another interesting link weaving all the aspect we have mentioned before has been proposed by F. Ivanhoe. He relates the increased geomagnetic field periods with the human major cultural advances [39, 40]. He has done this by making a statistical survey of paleolithic human skulls and has found leaps in brain-size evolution of humans. Following this, he has completed the loop through the growth hormone pathways in the hippocampus of the brain. There is a one-way nerve based current flow in the hippocampus, which may detect the geomagnetic field strength and trigger pituitary gland that secretes growth hormone. Growth hormone amounts in pregnancy have a direct relation with the fetus cerebral cortex size and the amount of the nerve cells [41, 42].

There can be other factors generating other biomagnetic fields such as water molecules in the body energizing from geomagnetic field by nuclear magnetic resonance (NMR) or special proteins, which operate in a wide range of conductance like integrin [43]. It is possible to generate an amplified magnetic field with a relatively miniscule current with integrin that is located on the outer wall of the cell membrane. This could very well be a mechanism for the information transfer or the bio-field generation among tissues, organs, and systems.

Integrin is also calcium binding protein, and there are different ion pumps in the cell membrane such as K^+ , Ca^{++} , Na^+ , Mg^{++} . Liboff has proposed ion cyclotron resonances (ICR) to be instrumental in the effectiveness of the pumps in the presence of static geomagnetic field [44]. Since static geomagnetic field does not directly affect the organic tissue, the ion cyclotronic processes in living things are tuned according to the static geomagnetic field. It is no coincidence that only the cations can benefit the ICR [44-47].

ICR exposure of living tissue has also been found to increase the overall conductivity and in return the proton hopping. Hydronium helical proton hopping has fundamental effect in biological expressions such as oxidative phosphorylation [44-47].

Now let us investigate artificial electromagnetic sources in our environment.

4. ARTIFICIAL EM SOURCES

In the urban life, the society is under constant exposure of fields and waves born out of the technologies. The power demand mainly supplied by the power grid for the residential and industrial usage could only be made available by a wide-spread distribution network. This itself alone contributes to most of the extremely low frequency (ELF) magnetic fields affecting us. In contribution to the grid, the electrical and electronics equipment, which we use in our daily life, can also be mentioned as a complementary cause.

Many other fields and waves add up to this sea of EM on the radio frequency (RF) and microwave (MW) bands of the EM spectrum. These are created by mobile telecommunications, Radio Detection and Ranging (RADAR) stations, machine-to-machine wireless communications, radio and TV broadcast stations, near field communications, satellite communications, long haul radio links, laser communications, and so on. But among those, mobile telecommunications is in the center of effect by Gauss's rule of big numbers, since the telecommunication base stations and their mobile terminals are far more than all the other EM sources both in number and in power impact.

With the expanse of the mobile communication for public usage by reasonable economical means, our way of living has transformed into a "mobile" only culture. As the mobile lives were more cultivated, so did the mobile networks. The mobile Internet and the social networks boom have boosted the investments into cellular networks and speeded up the roll-out of newer technologies as well as the capabilities of their interworking [10, 48].

With the increasing number of users and their increasing demand for wireless data, there is a strong push towards using new technologies. This trend, in turn, affects not only the technology upgrades but also the structure of the networks. From the second generation (2G) mobile technology's macro-cell, midi-cell, and micro-cell base station (BS) structures, the mobile networks evolved into a structure, where more spectrum utilizing technologies such as third generation (3G) and fourth generation (4G) mobile technologies are concurrently deployed. The Universal Mobile Telecommunications System (UMTS) based

on Wide-band Code Division Multiple Access (WCDMA – 3G) and Long Term Evolution (LTE – 4G, 5G and beyond) based on Orthogonal Frequency Division Multiple Access (OFDMA) utilize even smaller pico-cell and femto-cell architectures with enhanced spectral efficiency. The main motivation behind this is to decrease the distance between the base station and the user terminal and to have a higher throughput. Additionally, offloading from the cellular networks onto, say, WI-FI (Wireless Fidelity/Wireless Local Area Network (WLAN)) is a side-benefit [10, 48]. Thus, mobile operators must lay out denser networks in order to confront the demand for broadband data. The frequent utilization of smaller cells further down in the scale such as nano-/pico-/femto-cells is the inevitable result of this motivation in the urban areas. In short, almost every house will soon have its own base station [10, 48, 49].

Similarly, mobile user equipment (UE) has evolved into a hybrid multi-band multi-technology device. Comprising style with the faster customer demand for more services converges onto a single device, namely, smartphone (SP). Remarkable improvements in the user interface and in the capability set of these SP mobile devices have turned subscribers into prodigious consumers of mobile data services [48]. As of latest figures, three people out of four have a UE in the world.

4.1. Spectrum Components of UE and BS

The EM exposure from a UE is far more than BS during active usage as a result of immediate proximity to user. So, let us have a look at the frequency components of UE first to understand the spectrum born out of that equipment according utilized technology.

In 2G, though surprising, there are ELF components at 0.5 Hz, 8.33 Hz and super low frequency (SLF) component at 216.7 Hz born respectively by discontinuous transmission, coding and protocol pulse, and pulse repetition rate of transmission by TDMA, respectively, the latest being the far stronger one [50]. It is worthwhile to note down that first two frequency components fall in the main theta and alpha brain wave range. In 3G, the power slow and fast control loops give rise to ELF and SLF 10-100 Hz and ultra low frequency (ULF) at 1500 Hz, respectively, latest being the far stronger one [51, 52]. A pulse repetition is not readily observable in 3G as in 2G.

In 4G, in order to manage the Peak to Average Power Ratio (PAPR) Single Carrier-OFDMA (SC-OFDMA) is being used by UE. For Time Division Duplexing (TDD) mode, the uplink and downlink are only separated in time domain and the minimum switching time is 5 ms [49]. So, possible on-off cycles of UE will trigger expected SLF and ELF frequencies at 200, 100, 66, 50, 40 Hz and so on, in decreasing strength order. But the random nature of the channel utilization will fade the dominance of a single frequency in long term usage. For Frequency Division Duplexing (FDD) mode, the transmit time interval (TTI) is 1 ms [48]. Since different spectrum blocks in carrier aggregation (CA) [47] (intra carrier aggregation only in Release 13 [54]) can be allocated as well as number of resource blocks can be changed, one can expect all kinds of ELF, SLF, ULF from near DC up to 1000 Hz range none being dominant from the TTI point of view. The modulation structure of SC-OFDMA contains closely positioned multiple carriers, and the spectrum of the baseband and passband signals are almost flat. The radio resource block that will be assigned to UE may differ from 1.4 MHz to 20 MHz (100 MHz with CA), the ELF components power and spread will be increasing with the increasing capacity utilized. Nonetheless, to seek a single dominant ELF frequency in FDD SC-OFDMA will still be a trivial pursuit.

The fifth-generation mobile technology (5G) makes use of spatial modulation by beam forming through multiple input multiple output (MIMO) antennas. The frequency range of 5G is both in lower segment such as 700 MHz, and it may use spectrum all the way up to 90 GHz range. Since the higher 5G spectrum standard beyond 6 GHz is still under discussion at this moment, it would be wise wait and see until it is set up.

In terms of output RF power, 2G and 3G UE can utilize 2 Watt (W) output power, which decreases down to 0.8 and 0.25, respectively for latter generations, while 4G UE cannot pass beyond 0.2 W (23 dBm +2 dB tolerance) even in a CA scenario [54]. The maximum outpower for UE is regulated to maximum 2 W in most countries. So, seeking UE based radiation exposures based on thermal effect would not be much fruitful in terms of novelty taking into consideration the accumulated works in this field with newer UEs at the first glance. But it is vital to note down that many UEs comply with the power and SAR limitations based on conservative one-dimensional (1D) scenarios with an average power approach. There may be UEs, which may not comply with the power and SAR limitations in another country if bought from a different country with a different standard. The second

important point is the different terminal positioning options as well as multi-technology concurrent usage scenarios such as 3G, 4G, 5G. Last but not the least, MIMO antennas and their output powers should be increased in order to provide the committed data throughputs in 5G, and 5G UEs will comply with the regulations only on the average output power constraint with their multiple antennas.

We will refer to base station/2G, NodeB/3G, evolved NodeB/4G, next generation NodeB/5G as simply base station (BS) not to get lost in the base station terminology. On BS side, a wireless network service provider has a motivation of achieving the coverage and capacity requirements based on expected revenue with optimum spending. It is a complicated utility function that depends on economic variables such as the pricing model for services, capital expenditure (CAPEX), operating expenditure (OPEX), expected revenues as well as competitive and governing variables such as regulatory conditions and competitive pressure, respectively [10, 48]. Since the newer technologies have better spectrum efficiencies and reduced OPEX, a wireless network operator tends to migrate on to the next technology based on its investment abilities while still complying with the regulatory requirements. These regulatory requirements are not always necessarily for the establishment of new technology expansions; on the contrary, they are mostly for the existing service continuation.

Contemporary cellular radio networks have layers of several mobile technologies with complex interworking structures. For that reason, it is even harder to make any serious modifications to the existing structures and each change may trigger unanticipated ripple effects throughout the network [55]. The base stations belonging to different generations of mobile technology, which are totally different from each other in system and architecture, are generally share the same locations benefitting from the same cabling, power and transmission infrastructure. Thus, it is also beneficial for the network operator to utilize the same base station footprint as much as possible to decrease additional site leasing, administration, site acquisition, legal permissions, maintenance and infrastructure investment costs.

Increasing public concerns on EM radiation from cellular installations have in time increased the regulatory control on cellular operators. Therefore, cellular operators

camouflage their installations as much as possible to avoid public unrest and follow strict regulatory rules on how antennas and radio base stations should be installed in urban areas [10, 55]. Therefore, mobile operators use combo antennas, which encapsulate multiple dipole antennas aimed at different frequency bands within a single radome. We can also generalize that antenna dipole structures change only with frequency band but not necessarily with technology for general telecom antennas. Technology agnostic licensing also helps the process in that trend and avails a softer transition. Whether for MIMO utilization or for multiband radio access, this minimalist approach of the footprint for antennas has made +/- 45° cross-polarized (XXXX-pol) combo antennas almost an industry standard.

At this moment, it would be wise to have a look at the electromagnetic irradiation security distance regulation in Turkey, as an example. The regulation [56] takes into account a(ny) measurement in the central azimuth of the antenna in a range of acceptable points for the calculation of security distance minimum. The calculation is made such that,

$$d=(30xPxG)^{1/2}/E_{lim} \quad (4.1)$$

where d is the minimum security distance, P is the transmitter output power, G is the antenna gain and E_{lim} is the maximum allowable electrical field component for a single source. The regulatory maximum allowed field strength values are 10.23 V/m, 14.47 V/m, and 15.00 V/m for 900 MHz, 1800 MHz and 2100 MHz, respectively. These values correspond to one fourth of the ICNIRP recommendations [54, 55]. For sources more than three, the ICNIRP recommendations are taken as maximum values [57, 58]. Taking into consideration the utilization of combo antennas with their similar gains and inherited property of four encapsulated antennas in our example, the possible field values may easily be boosted up to four times. It is also important to mention at this stage that the new 2020 ICNIRP recommendations have been released as of 2020 [58]. The new recommendations only add up more blur to the discussions by regulating 6 GHz and above spectrum for the new 5G frequency bands, and averaging the regulations to 6-minute periods and to total body exposures [58].

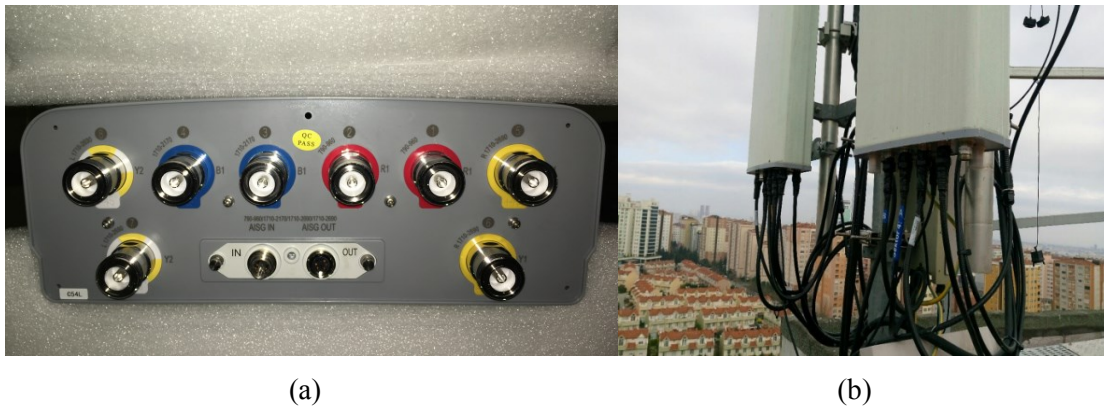


Figure 4.1. (a) A combo antenna hosting 4 pairs of X-pol antennas namely red pair 710-960 MHz, blue pair 1710-2170 MHz and yellow pairs on both sides 1710-2690 MHz; (b) two of combo antennas operating in multiband configuration.

As a result, the artificial EM exposure has increased in hundred thousand times in magnitude and has started raising a serious public health concern within last three decades. Sleep disorders, nausea, endocrinological anomalies such as melatonin and serotonin secretion decent and public awareness and unrest were on the rise [59].

5. OVERVIEW OF ELECTROMAGNETIC THEORY FOR BIOELECTROMAGNETISM

5.1. Maxwell's Equations

Electromagnetic phenomena deal with electric and magnetic fields with respect to space and time. Maxwell's equations [60] interconnect these time-varying electric and magnetic fields with their interrelations in their differential form as:

$$\nabla \cdot \mathbf{D} = \rho_c \quad (\text{Gauss's law}) \quad (5.1)$$

$$\nabla \cdot \mathbf{B} = 0 \quad (\text{Gauss's law - magnetic}) \quad (5.2)$$

$$\nabla \times \mathbf{H} = \partial \mathbf{D} / \partial t + \mathbf{J} \quad (\text{Maxwell - Ampere law}) \quad (5.3)$$

$$\nabla \times \mathbf{E} = -\partial \mathbf{B} / \partial t \quad (\text{Faraday's law}) \quad (5.4)$$

with the following essential relations:

$$\mathbf{D} = \epsilon \mathbf{E} = (\epsilon' - j\epsilon'') \mathbf{E} \quad (5.5)$$

$$\mathbf{B} = \mu \mathbf{H} = (\mu' - j\mu'') \mathbf{H} \quad (5.6)$$

$$\mathbf{J} = \sigma \mathbf{E} \quad (5.7)$$

where \mathbf{E} , the electric field strength in vector form; \mathbf{D} , the electric displacement in vector form; \mathbf{H} is the magnetic field strength in vector form; \mathbf{B} , the magnetic flux density in vector form; \mathbf{J} , the current density in vector form; ρ_c , the charge density; $\epsilon = \epsilon' - j\epsilon''$, the complex permittivity of the material; $\mu = \mu' - j\mu''$, the complex permeability of the material; and σ , the conductivity of the material.

From Equations (5.1) to (5.7) one can deduce that the responses of an electromagnetic material to electromagnetic fields are established by three essential parameters, namely permittivity ϵ , permeability μ , and conductivity σ . One can also use these essential parameters in order to calculate the extent of penetration of electromagnetic field into the material for a given frequency.

5.2. Homogeneous Vector Wave Equations

\mathbf{E} or \mathbf{H} can be obtained by use of Equations (5.1) and (5.2) with the essential relations given in Equation (5.5)-(5.7) by taking the curl,

$$\nabla \times \nabla \times \mathbf{E} = \nabla(\nabla \cdot \mathbf{E}) - \nabla^2 \mathbf{E} \quad (5.8)$$

$$\nabla \times \nabla \times \mathbf{H} = \nabla(\nabla \cdot \mathbf{H}) - \nabla^2 \mathbf{H} \quad (5.9)$$

and making use of the vector identity “ $\nabla \cdot (\nabla \times \mathbf{A}) = 0$ ” in the absence of \mathbf{J} current density in a source-free environment, the equations simplify into:

$$\nabla^2 \mathbf{E} = \mu\epsilon \frac{\partial^2 \mathbf{E}}{\partial t^2} \quad (5.10)$$

$$\nabla^2 \mathbf{H} = \mu\epsilon \frac{\partial^2 \mathbf{H}}{\partial t^2} \quad (5.11)$$

This form of the equations is called homogeneous vector wave equations or vector Helmholtz equations. These fields must also satisfy the boundary conditions (BC) for continuity of both normal and tangential components at medium changes.

5.3. Reciprocity

Bioelectromagnetism may be studied along with electric, electromagnetic, and magnetic phenomena into the conceptual dimension (horizontally in Figure 5.1.) with three domains, respectively: bioelectricity, bioelectromagnetism, and biomagnetism.

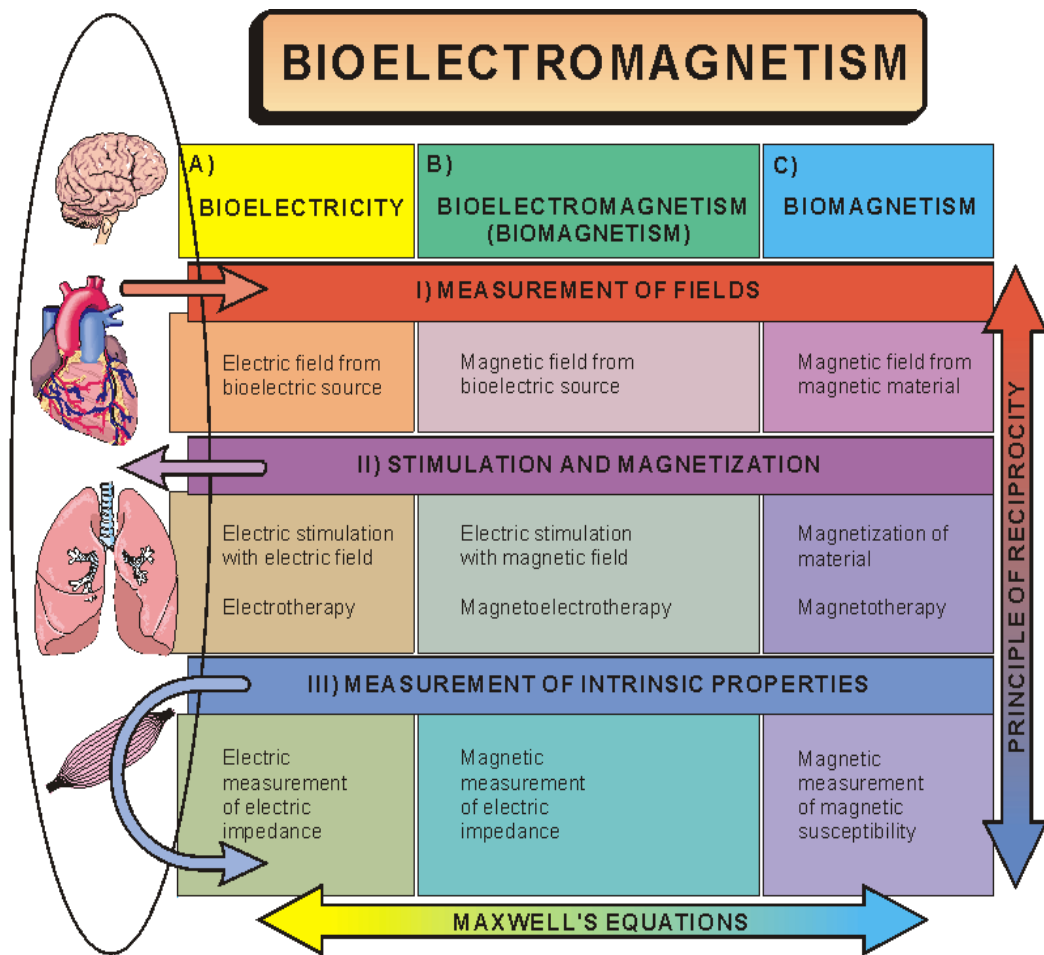


Figure 5.1. Taxonomy of bioelectromagnetism [61].

Bioelectricity is the study of electrical phenomena of processes of life. Biomagnetic fields are born out of bioelectric signals and bioelectric fields are born out of bioelectromagnetic and biomagnetic fields by reciprocity of Equations (5.3) and (5.4). So, we may classify bioelectromagnetism practices (vertically in Figure 5.1) as: field measurements born from bioelectromagnetic sources; fields born from electric or magnetic stimulation; and intrinsic tissue bioelectromagnetic property measurement [61]. The principles of reciprocity are shown with their applications and explanations in detail in Figure 5.2.

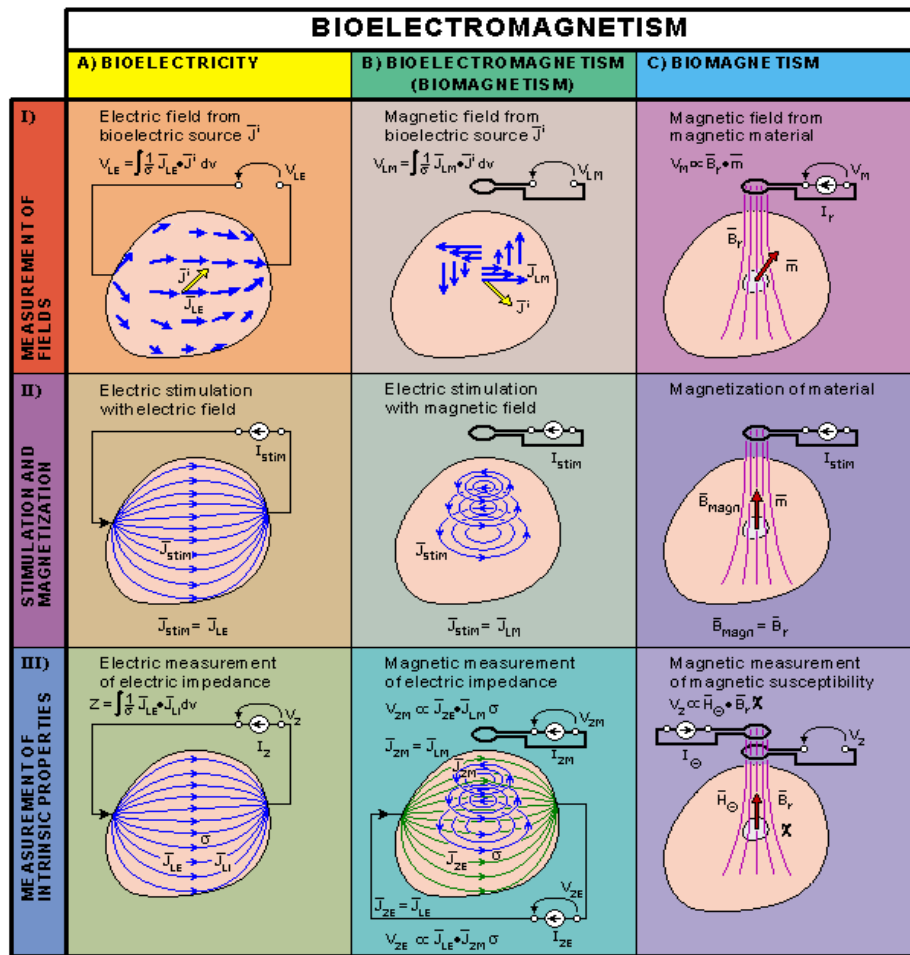


Figure 5.2. Theoretical view to define the subdivisions of bioelectromagnetism [61].

5.4. Modeling the Problem with Finite Element Method

Our study mainly aims to link EM effect of common radiofrequency exposure to one or more bio-markers focusing the skull in the human body. Following the thermal effects and their primary markers, our focus will be on electrical fields and its heat, voltage, and current inductions inside the skull, and their possible markers to bridge the relation in between. The problem can be visualized as in Figure 5.3, a human head exposed to an antenna.

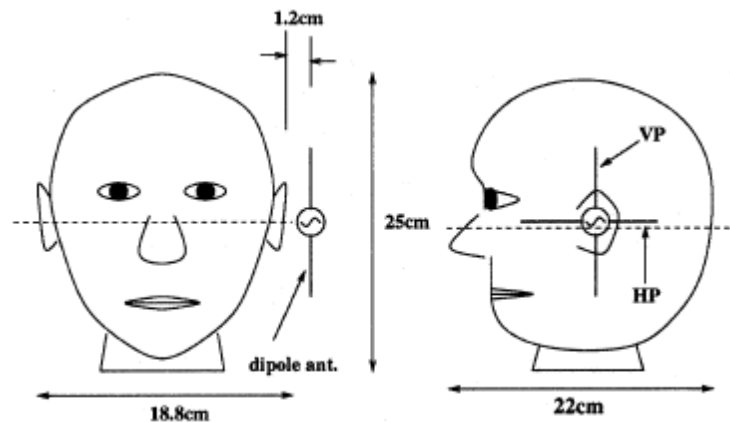


Figure 5.3. Visualization of the problem [62].

Firstly, we need to study the Finite Element Modeling (FEM) of the Specific Absorption Rate (SAR) distribution due to the radio frequency exposure in which vector Helmholtz equation and its partial time derivative will be studied in order to find the voltage induced into the tissue. SAR is defined as the measure of the rate at which radio frequency energy is transferred in the body. So, SAR is the energy change (dW) in an incremental mass (dm) by dissipation or absorption over an incremental volume element (dVol) with a known density in an incremental time.

In order to find the interactions between the biological tissues and electromagnetic fields dosimetric studies are performed. Since electromagnetic source versus body and head exposures are quite nonuniform in nature, SAR is the most appropriate form of metric to specify the safety limits agnostic to electric, magnetic or power density figures alone. It is also agnostic from the antenna distance whether it is far field or near field. It also serves as a measure for extrapolating the cell to tissue, tissue to organ, organ to animal, and animal to human exposures. Therefore, many national and international safety recommendations are based on figures in terms of SAR and its temperature increase [57, 58]. For lower SAR values, it would be instrumental to find the voltage and the current induced as well, in order to find a voltage and current gradient superimposed onto the tissue during exposures. Nonetheless, such inductions are limited to the very surface taking into consideration the utilization of higher band frequencies in mobile telecommunications.

SAR can be calculated from the induced electric field of strength \mathbf{E} inside a body together with the bulk conductivity σ and with the mass density ρ of tissue as given in Equation (5.12). It can be represented by averaging over the mass of 1g or 10 g of tissue.

$$\text{SAR} = \sigma \frac{\mathbf{E}^2}{\rho} \quad (5.12)$$

In order to calculate the SAR distribution values, one must solve the vector Helmholtz equation everywhere in the domain for the frequency of RF source. The vector Helmholtz equation, which is a translation of Maxwell's time-dependent curl equation, is given in Equation (5.13) for \mathbf{E} ,

$$\nabla \times \frac{1}{\mu_r} \nabla \times \mathbf{E} - k_0^2 \epsilon_r \mathbf{E} = 0 \quad (5.13)$$

where μ_r is the relative permittivity for the material, ϵ_r is the relative permittivity for the material, and k_0^2 is the freespace wave vector. Solution of this equation provides the required electric field value \mathbf{E} for SAR calculation. \mathbf{E} has the relation to V as in Equation (5.14)

$$\mathbf{E} = -\nabla V \quad (5.14)$$

For high exposure conditions, where serious temperature elevations are produced, SAR can also be calculated as the temperature rise over short exposure duration multiplied by the specific heat capacity of the tissue. For the long exposure duration, the heat transferred by the EM source will be calculated by the Pennes' bioheat equation:

$$\rho c \partial T / \partial t = \nabla \cdot (k \nabla T) + \rho Q_{\text{met}} + \rho(\text{SAR}) - \beta(T - T_{\text{blood}}) \quad (5.15)$$

$$\beta = \rho_{\text{blood}} c_{\text{blood}} \rho \omega \quad (5.16)$$

where the ρ [kg/m³] is the material density, c [J/(kg°C)] is the specific heat capacity, k [W/(m°C)] is the thermal conductivity, Q_{met} [W/kg] is the metabolic heat generation rate, β [W/m³°C] is the blood perfusion coefficient, ω [L/(s·kg)] is the blood perfusion rate, and T_{blood} is blood temperature [63].

5.5. Finite Element Method

Any engineering or scientific physical phenomenon can be expressed by partial differential equations. But classical analytical methods are too complex for solving these equations for arbitrary shapes. Therefore, electromagnetic scattering and radiation problems require numerical solutions to partial differential equations (PDEs) with different methods. Finite Element Method (FEM) is more popular compared to other techniques such as MoM, FIT, and FDTD for solution of complex electromagnetic solutions.

The finite element method (FEM) solves partial differential equations numerically with certain approximations. It was developed for the increasing demand of structural analysis challenges by aerospace and civil industries in mid 1950's. FEM dissects any given object, such as in Figure 5.3, with smaller geometrical divisions called finite element by virtue of triangles or tetrahedrals. The size and the shape of the finite element can be chosen depending on the accuracy or the convergence of the problem at hand. Then, an error minimizing algorithm is governed to establish a converged solution set, out of which a total solution is built [64].

Finite Difference Method (FDM), on the other hand, was developed by Yee in 1966 with the idea of using Taylor expansion approach on finite differences on an object dissecting into three dimensional cells of fixed size. FDTD technique belongs to the FDM family of discretization solutions. This method converts the partial derivative equations into difference equations, which in turn used to approximate derivative solutions. Although this method is rather easy to govern, it is not that easy to apply for complex objects [64].

Let us consider we would like to find the temperature distribution for Figure 5.4. The separation of variables approach is not going to work properly for an engine block even if one would write a heat balance equation that complicated geometry. That would require the usage of much finer cubic cells, which in turn, would increase the computational load. But FEM dissects such a problem into finite elements inter-linked by nodes. This construct enables a simpler approach as in Figure 5.4 and Figure 5.5. It is established by meshing the geometry with basic finite element of choice with flexibility of choosing mesh size along the different parts of the geometry. FEM algorithms govern a systematic methodology that is

easy in terms of computational effort. The equations are calculated and solved on mesh points and increasing the number of meshes decreases the error in the approximation. Having a flexible meshing capability, one can make a trade-off between accuracy and computational load according to the properties of the geometry [64].

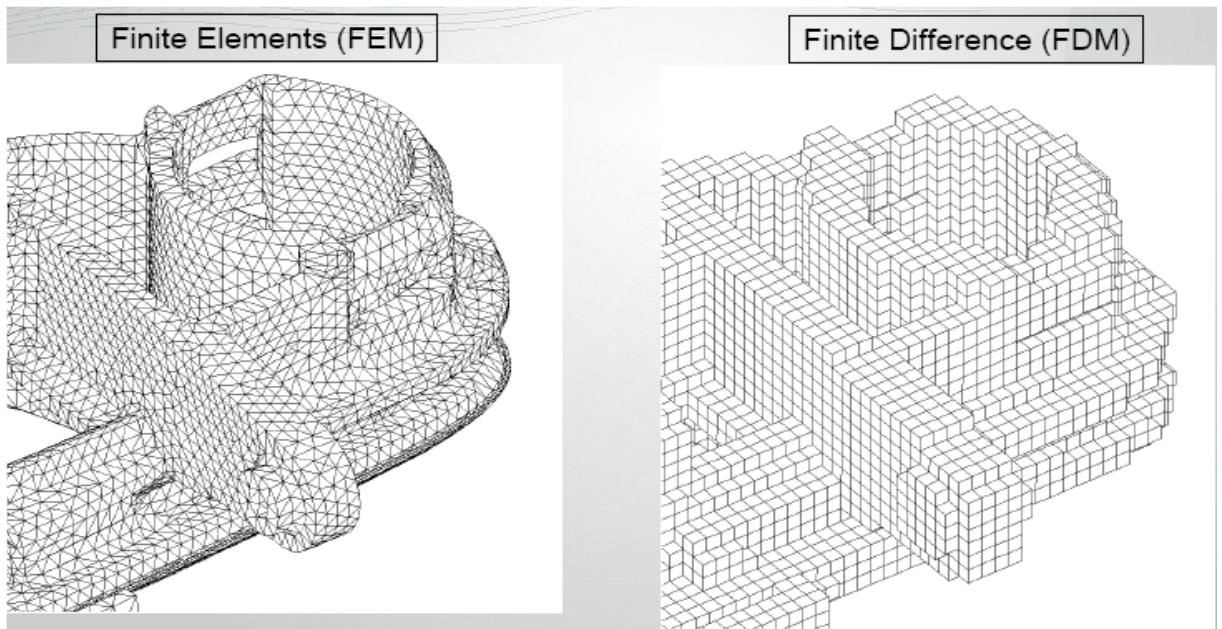


Figure 5.4. Difference between FEM and FDM in simulation.

Below definite steps constitute FEM in establishing a finite element analysis of a physical problem. These steps are:

- Identify the geometric domain of the problem.
- Define the element type(s) to be utilized.
- Define the elements material properties.
- Define the elements' geometric properties.
- Define the element mesh structure.
- Define the physical boundary conditions.
- Define the initial conditions and environmental constraints.

FEM softwares generally solve the underlying algebraic equations in matrix form and computes the unknown values of the primary variable at the meshes. These values are then fed back and summed up to compute the derivatives [64].

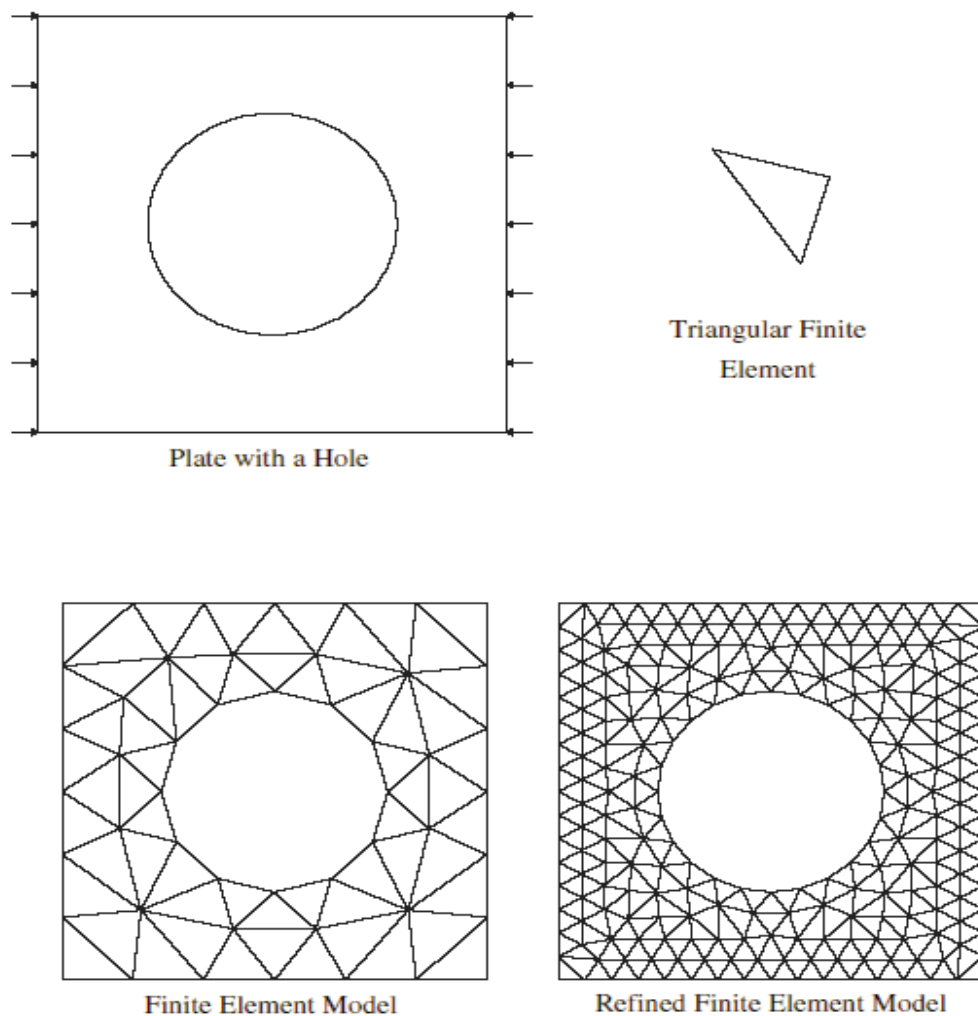


Figure 5.5. Geometry, loads and finite element meshes.

Finite elements are not limited to triangles or tetrahedrals, but can be defined on quadrilateral sub domains, too. Polynomial and even non-polynomial based shapes can also be used for higher orders. Analysis and evaluation of the solution results can be done based on the post processing capabilities of used FEM software. A typical software can perform the following:

- Sort element values in order of magnitude.
- Check equilibrium and implement probes for measurement.
- Calculate factors of safe operational margins.
- Plot structural shape with different expression of analysis data.
- Animate dynamic behavior of the model based on time and variable inputs.
- Generate color-coded temperature/stress/load/field strength plots.

5.6. FEM versus FDM Comparison

The differences of these two methods are as such:

- FEM expresses complicated geometries and boundaries with ease with dynamic meshing capabilities. FDM is supposed to use rectangular shapes. FEM handles geometries straightforward.
- FDM is very easy to implement. Its solution is also very easy to transfer to simple matrix forms.
- FDM can be considered as a simplified method of FEM approach. Basis functions can be selected as either piecewise constant functions or Dirac delta functions. The approximations of both approaches are valid on the entire domain, and need not be continuous.
- FEM approximations are of higher quality by the geometric enrichment and detailing, whereas FDM has a poorer quality of the approximation between grid points.

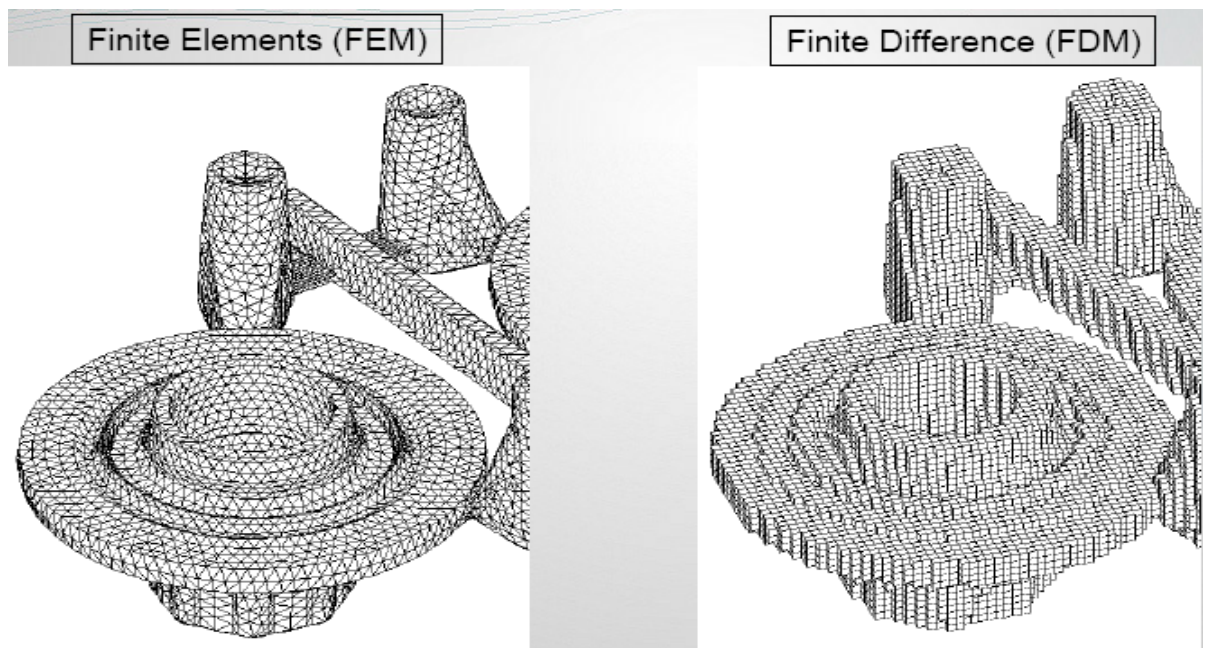


Figure 5.6. Difference between FEM and FDM in simulation.

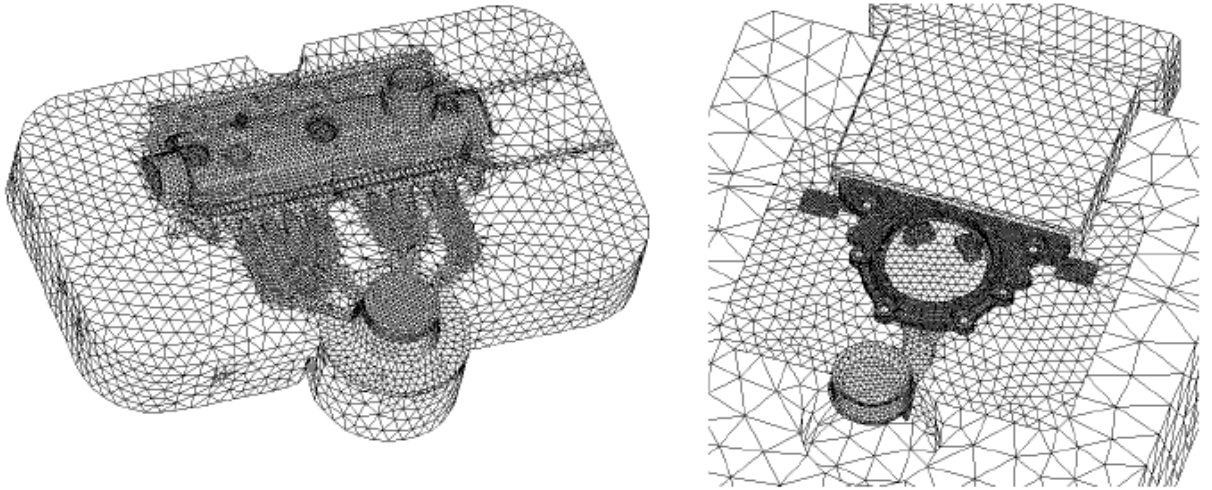


Figure 5.7. FEM supports non-coincident meshes.

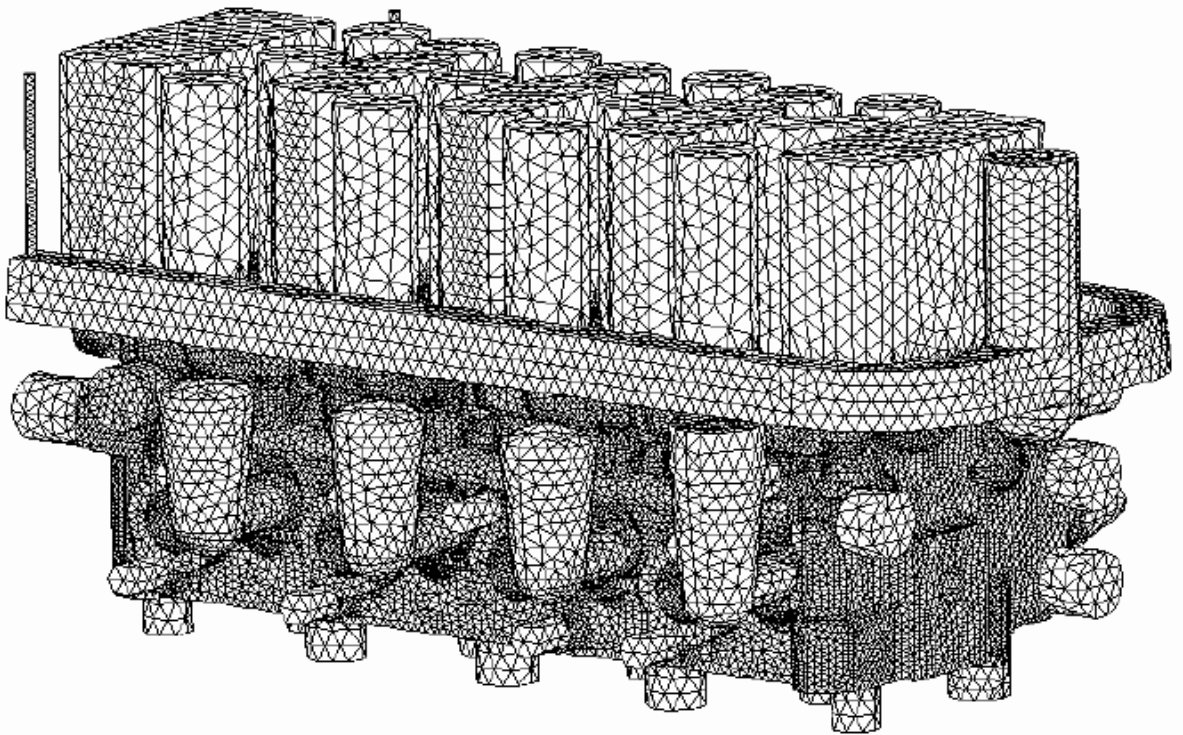


Figure 5.8. FEM defines complex geometries better.

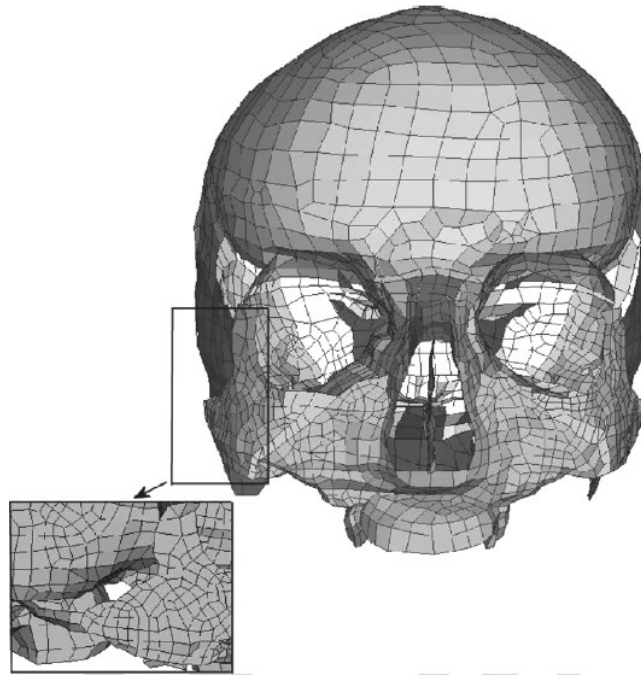


Figure 5.9. Example of FEM utilized in human skull [65].

Generally, FEM is favorite method for all types of electric field and potential distribution analysis. The shape and alignment of cells in a certain tissue can strongly affect the electric field strength and its potential distribution such as in muscle tissue, where there is strong orientation with additional layers or insulating structures.

In our case, the human skull has compact and sponge-like bones, cavities with air such as the frontal and sphenoidal sinuses and brain tissue with parts of different electrical and magnetic characteristics. FEM is the method of choice for anisotropic and abruptly changing parameters over FDM.

As a summary, FEM will be our method of choice in simulations because of its modeling strength of inhomogeneous and complex materials, complex geometries, and resonant cavities. The human skull has all three properties making FEM the choice over FDM.

5.7. Mie Theory – Multilayer Spherical Dielectric Model

In order to understand how EM waves behave, let us consider theory of multilayer dielectric models. Spherical models are good in terms of resembling the body curvatures into account. Therefore, these spherical models provide better approximations than planar multilayer models especially for the human head, which can be represented as a multilayer sphere.

Mie Theory becomes instrumental when transmitted and scattered fields interact in a multilayer sphere. An incident EM field is expanded in spherical vector harmonics by the boundary conditions (BC) at each layer of the multilayer spherical object in the Mie solution. The internal fields are then calculated as the sum of an infinite series of spherical harmonics.

In practice, it is impossible to solve for the exact calculations using the Mie solution. Thus, some simplifications are done through approximations and assumptions for a practical solution. By switching into the spherical coordinate system, one can benefit spherical symmetry of the multilayer spherical model, which in turn eases the equation solving process.

The human head has been modeled as a multilayer object, and the model used in this phase has six different tissues as layers. The innermost layer to the outermost layer is as follows: white matter, grey matter, cerebrospinal fluid (CSF), muscle, fat, skin.

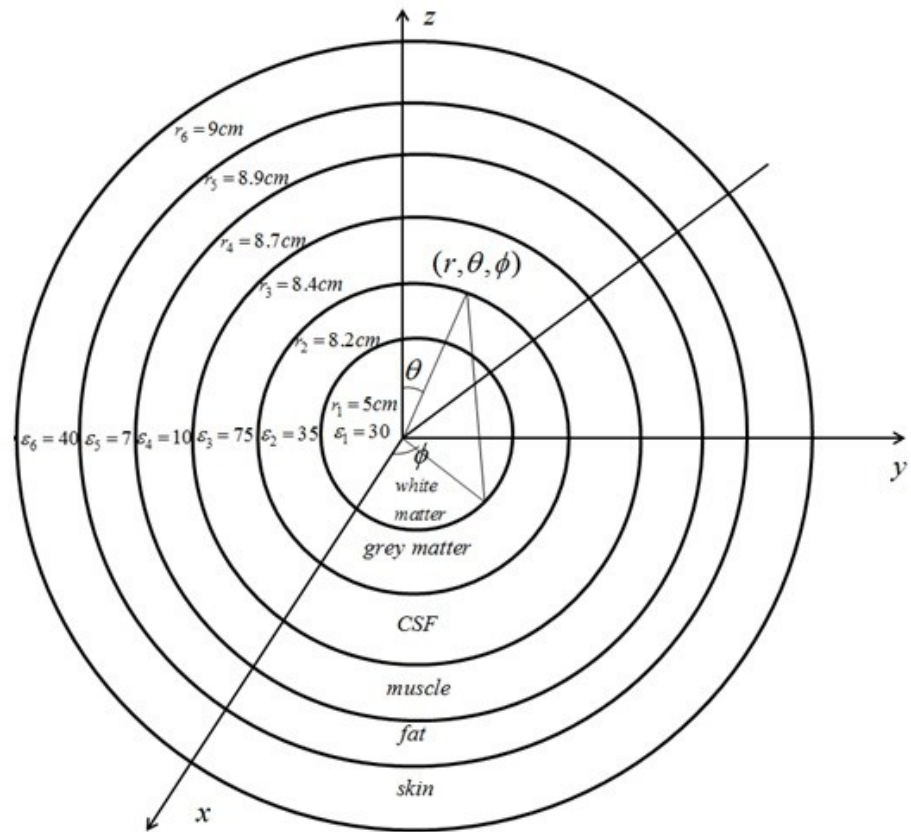


Figure 5.10. A representation of human head with 6 spherical layers [66].

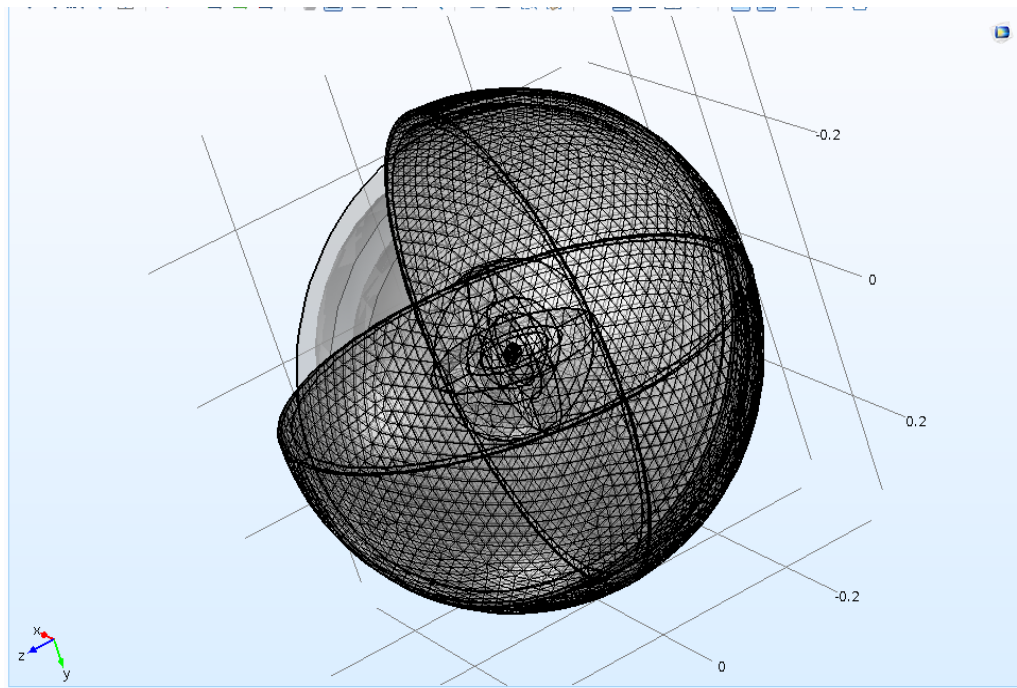


Figure 5.11. Our representation of human head model with 6 layers.

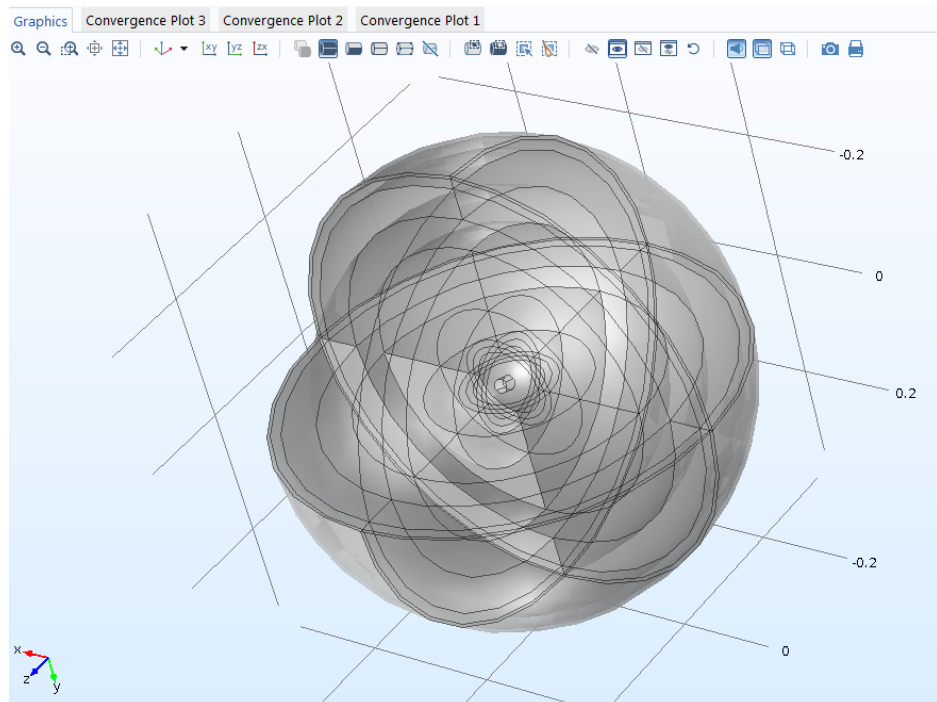


Figure 5.12. Our representation of human head model in domain view.

Stratton has formulated the solution of the electromagnetic problem on multilayer dielectric model based on the Mie Theory [67]. The incident and secondary (scattered and internally transmitted) fields are expanded into their respective vector spherical harmonics. Tangential components of electric and magnetic fields are equated at each regional boundary in order to determine the various unknown expansion coefficients, a_n^r , b_n^r , a_n^t , b_n^t for each region [66].

Incident Electric Field:

$$E_i = E_0 e^{-i\omega t} \sum_{n=1}^{\infty} i^n \frac{2n+1}{n(n+1)} (m_{01n}^{(1)} - i n_{e1n}^{(1)}) \quad (5.15)$$

Reflected Electric Field:

$$E_r = E_0 e^{-i\omega t} \sum_{n=1}^{\infty} i^n \frac{2n+1}{n(n+1)} (a_n^r m_{01n}^{(3)} - i b_n^r n_{e1n}^{(3)}) \quad (5.16)$$

Electric Field Induced within Sphere:

$$E_t = E_0 e^{-i\omega t} \sum_{n=1}^{\infty} i^n \frac{2n+1}{n(n+1)} (a_n^t m_{01n}^{(1)} - i b_n^t n_{e1n}^{(1)}) \quad (5.17)$$

Scattering Efficiency Factor:

$$Q_s = \frac{2\pi}{k_2^2} \sum_{n=1}^{\infty} (2n+1) (|a_n^r|^2 + |b_n^r|^2) \quad (5.18)$$

Total Efficiency Factor:

$$Q_t = \frac{2\pi}{k_2^2} \operatorname{Re} \sum_{n=1}^{\infty} (2n+1) (a_n^r + b_n^r) \quad (5.19)$$

Absorption Efficiency Factor:

$$Q_a = Q_t - Q_s \quad (5.20)$$

Size parameter:

$$x = ka = \frac{2\pi a}{\lambda} \quad (5.21)$$

Lorenz formulas can also be used to determine the absorption and scattering efficiency constants [68]. These formulas are identical to scattering formulas of Rayleigh.

$$Q_s = x^4 \frac{8}{3} \left| \frac{m^2 - 1}{m^2 + 2} \right|^2 + \dots \quad (5.22)$$

$$Q_a = -\operatorname{Im} \left\{ 4x \frac{m^2 - 1}{m^2 + 2} + \frac{4}{15} x^3 \left(\frac{m^2 - 1}{m^2 + 2} \right)^2 \frac{m^4 + 27m^2 + 38}{2m^2 + 3} \right\} \quad (5.23)$$

where $m = (\mu_r \epsilon_r)^{1/2}$ is the refractive index of the corresponding layer with respect to air.

Mie theory can be applied to multilayer dielectric models of cylindrical or spherical nature for scattered, reflected, absorbed or transmitted waves. In our model, we will investigate the Mie limitations of frequency at hand versus the biological tissue size. So, we will know the theoretical aspects, empirical values from other studies on EMF effects on biological tissues and our simulation model limitations in order to know when we can use our simulation results to bridge back with the results of the biological studies.

6. UE SIMULATIONS AND BS FIELD MEASUREMENTS

We have already mentioned the domination of BS and UE as sources of EMF in terms of utilization amounts as well as in terms of usage periods for human exposure. Therefore, it is vital to follow the changes in UE as the technologies evolve from 2G to 5G and beyond.

The connectivity of an all-technology-supporting UE has only certain radio utilization pathways in a mobile network with concurrent existence of all generations of mobile technologies. Among those pathways, there are certain scenarios of interest when multi-radio capable UE will irradiate at two different bandwidths at the same time. These are 2G with WI-FI (possible but rather obsolete), 3G/4G/5G and WI-FI, 3G with device to device (D2D), 4G and 5G with device to device connections. 3G, 4G, and 5G technologies rather utilize fall back protocols, and 2G and even 3G are obsolete in terms of data usage. D2D is just ramping up, and it may be possible to see 3 radio capable UEs in the market soon, but we will rather keep it out of our scope. Similarly, close proximity radio technologies such as Bluetooth is kept out of our scope because of its low power and similar frequency range.

6.1. Multilayer Brain Model

Our model utilizes six layers of dielectric layers and an anomaly in the center of the sphere and the model will be radiated with a TE wave in X-Y plane moving in Z direction in Figure 6.1. The scattered field will be used in order to understand the metallic cylindrical anomaly's orientation that we have implanted. The applied frequency is kept fixed at 1 GHz for the sake of controlled experimentation.

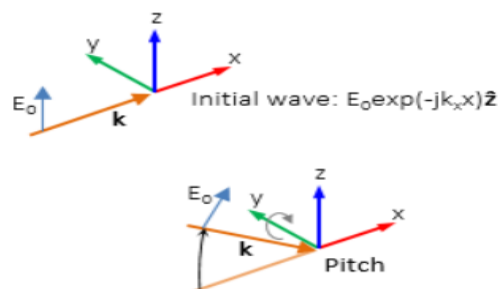


Figure 6.1. Wave direction in our model, TE x-y plane with pitch 90 degrees.

The far field norm can be seen in Figure 6.2 as the height and radius of cylinder decreases there is a certain moment, one cannot observe the bias. Far field norm is the first metric and we lose the orientation information. There is a more robust marker, which is the far electrical field value as in Figure 6.3.

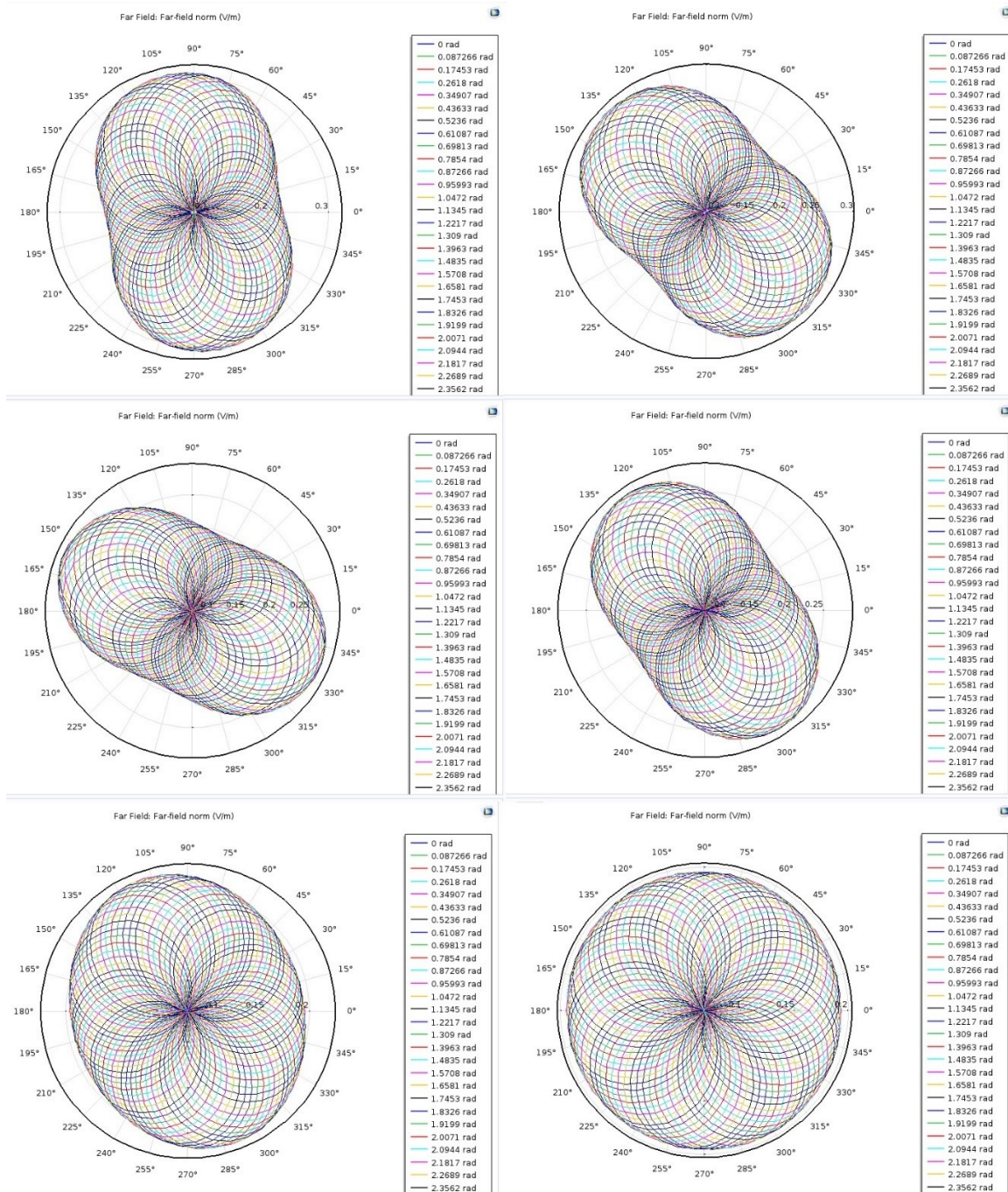


Figure 6.2. Far field norm showing the bias of the rod orientation (Left to right and down in the sequence of height-radius of cylinder: 18-4; 16-4; 16-2; 12-2; 10-0.5; 6-1).

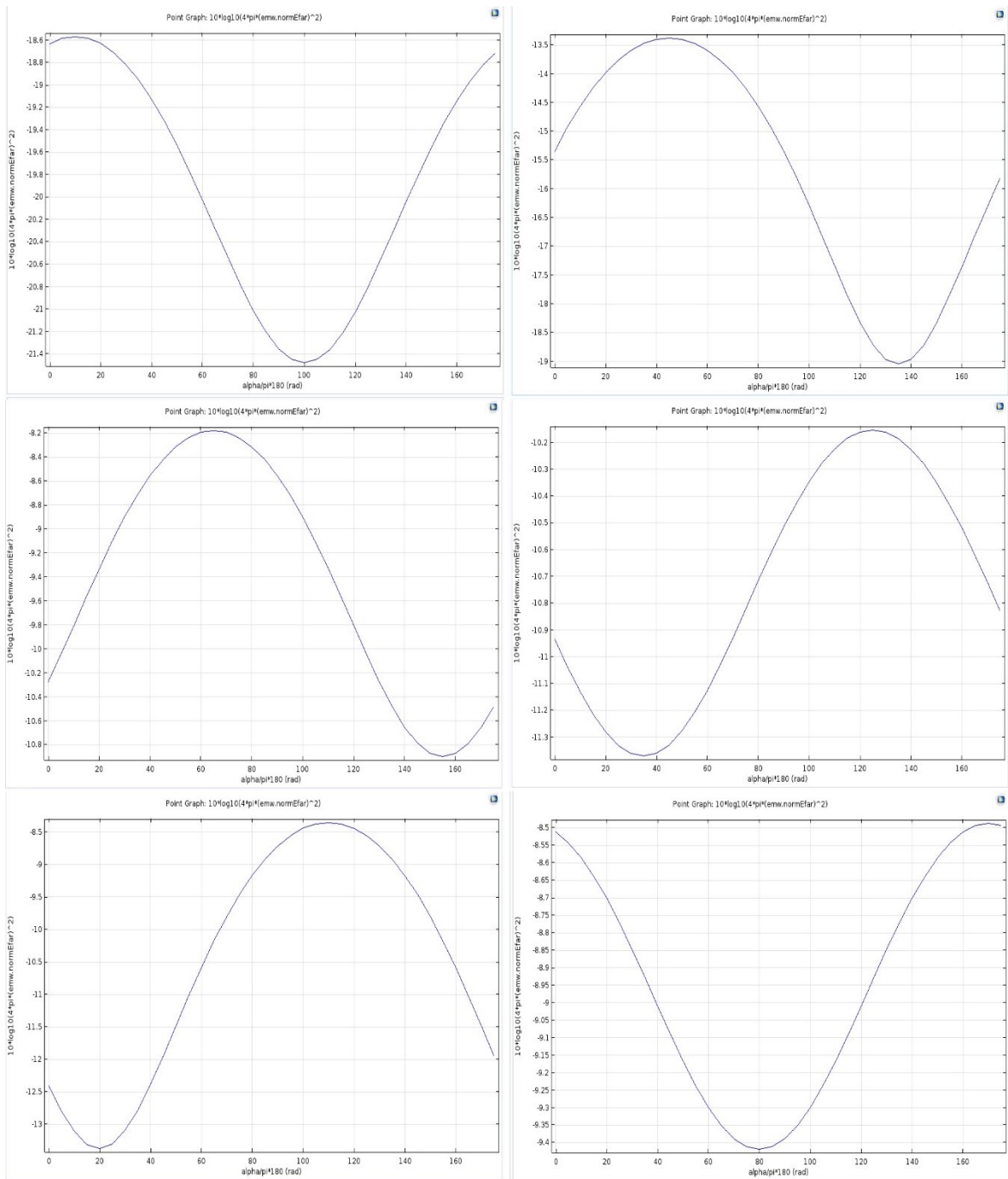


Figure 6.3. Far field electrical field value showing the degree of the rod orientation (Left right and down in the sequence of height-radius of cylinder: 18-4; 16-4; 16-2; 12-2; 10-0.5; 6-1).

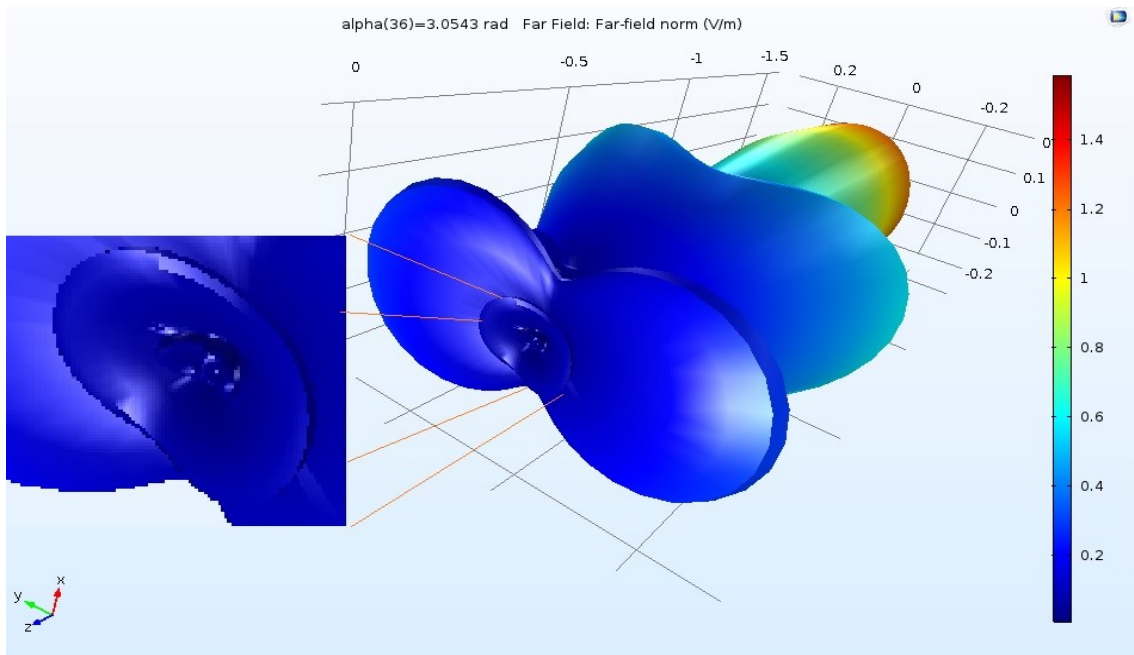


Figure 6.4. Far field 3D electrical norm of the 10 degree orientation rod 18-4.

The Figure 6.4 shows the 3D electrical far field norm and the 10 degree inclination of the rod can be observed by the slight shift in the central beam in the very core. Eventually, we lose the possibility of discrimination in the far field representations. Our simulation-based experience with the empirical value of the height and the radius of the rod was around 5-6 cm of the length for a reasonable radius. Taking into the Mie theoretical values which are around 0.01λ of the frequency at use, our value was 0.15λ . In order to have a better resolution one can surely go to higher frequencies for better resolution. Nonetheless, the higher frequencies will have less penetration power, that is, higher power levels should be used. In case when we need to assess not too dissimilar dielectrics from each other, the situation may be even more challenging. Now, let us recall that our aim in this part of the study is not to find a therapeutic or diagnostic utilization of EMF but just to understand how sharp the effects will be subtle from a detection point of view in order to back-up our assumption for linking back the findings to the simulation model.

6.2. Human Head Model and Tissue Parameters

The revised IEEE International Committee on Electromagnetic Safety Standard C95.1-2005 Standard for Safety Levels with Respect to Human Exposure to Radio

Frequency Electromagnetic Fields from 3 kHz to 300 GHz [69] and International Commission on Non-Ionizing Radiation Protection Guidelines for Limiting Exposure to Time-Varying Electrical, Magnetic, and Electromagnetic Fields (Up to 300 GHz) [57, 58] define 2 W/kg for 10 g locally averaged peak SAR along with the 0.08 W/kg for whole body average SAR limits. General exposure limits are relaxed by 5 times for occupational exposure.

Both above standards are based on measurement of the SAR in the specific anthropomorphic mannequin (SAM) head exposed to RF transmitting devices for the RF Energy Compliance of [70] the device under the test (DUT) in predefined positions.

SAM is a standardized phantom based on US army soldier head ensemble of different ethnicities. It is a homogeneous model resembling saline phantoms. Saline phantoms are homogeneous, and they have only a single value of conductivity and permittivity while the conductivity and permittivity of tissues change with frequency. Every tissue type has a different conductivity and permittivity and different tissues will absorb different amounts of energy. However, as frequency increases, especially above 100MHz, saline phantoms cannot perform as an accurate representation of the human head, because various materials behave differently. At very high frequencies, the high dielectric constant of water causes the electrical wavelength to be severely shortened within the phantom [71]. This introduces excessive errors of the electromagnetic field distributions when it is exposed on a biological system. It is necessary to take corrective actions at this phase. And the phantom should have the proper permittivity and conductivities to be equivalent to real tissues at the specified frequency of interest. The conductivity and permittivity of the human body has been well characterized from 10 Hz- 20 GHz by Camelia Gabriel in 1996 and once the frequency of interest is specified, the required permittivity and conductivity values can be identified in Federal Communications Commission (FCC) database recommended from the same study [72, 73].

The simulation software that we perform our FEM solutions, Comsol Multiphysics, utilizes the same SAM model. But we have introduced certain profound differences in our solutions. First of all, we perform multi-frequency concurrent analysis and for each frequency analysis different set of parameters are utilized according to FCC [72, 73] and

according to Schmid et al. [74]. Secondly, we utilize the Magnetic Resonance Imaging (MRI) deduced brain tissue mapping of SAM [75]. This greatly improves the frequency utilization scenarios based on current technology update as well as a higher resolution and accuracy of the heat distribution in the head tissue in order to analyze the aftermath.

6.3. Multi-Radio Supporting UE Simulation - Nominal

The basic SAR simulation of the UE usage in case of concurrent double radio (CDR) utilization is our first scenario. In this scenario, the first radio frequency is chosen as 2600 MHz a presumably 4G connection together with 2450 MHz WI-FI connection. In order to find the heat distribution in the most realistic way, the heat effect of both radios are calculated based on MRI deduced separation of different brain tissues and two radio exposures were solved simultaneously. Separate tissue conductivity and permittivity values are set for each radio effect. We have also simulated the time convergence of the model in order to observe possible steady state values. The simulation is run over a 60-minute period. The base temperature reference of the head is taken as 37 °C and the difference is given according to this reference.

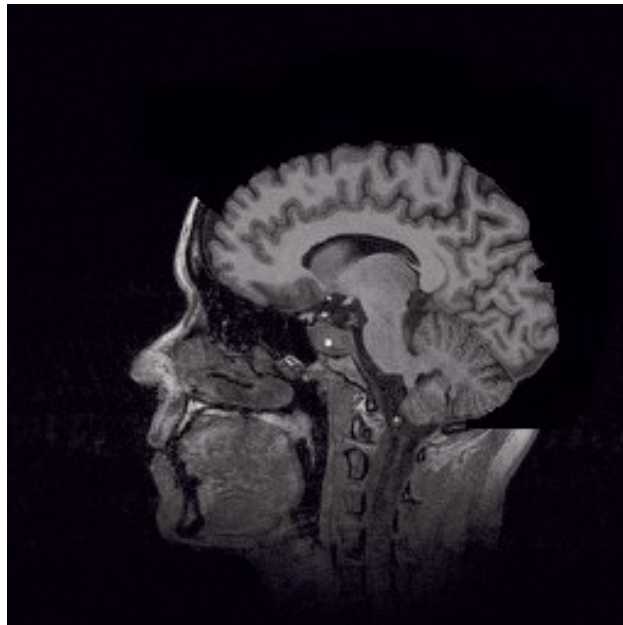


Figure 6.5. All simulations using the same MRI deduced brain tissue property interpolation [75].

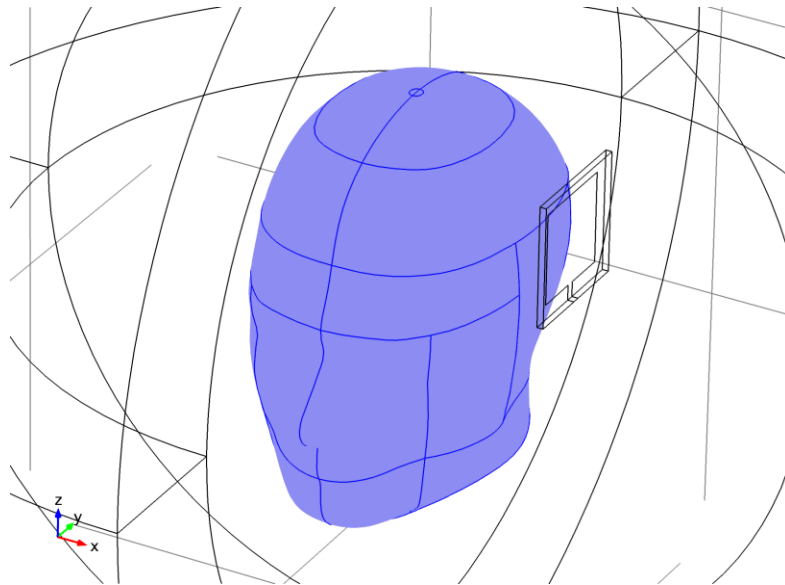


Figure 6.6. First CDR simulation with blue biological tissue SAM relative to concurrent radios' position.

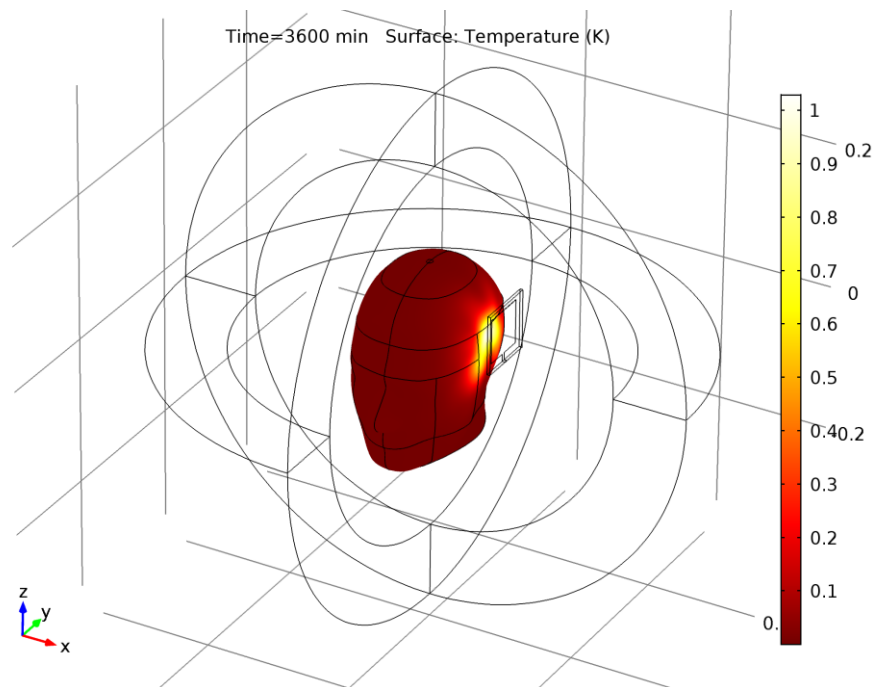


Figure 6.7. First CDR simulation heat distribution on SAM over 60 minutes.

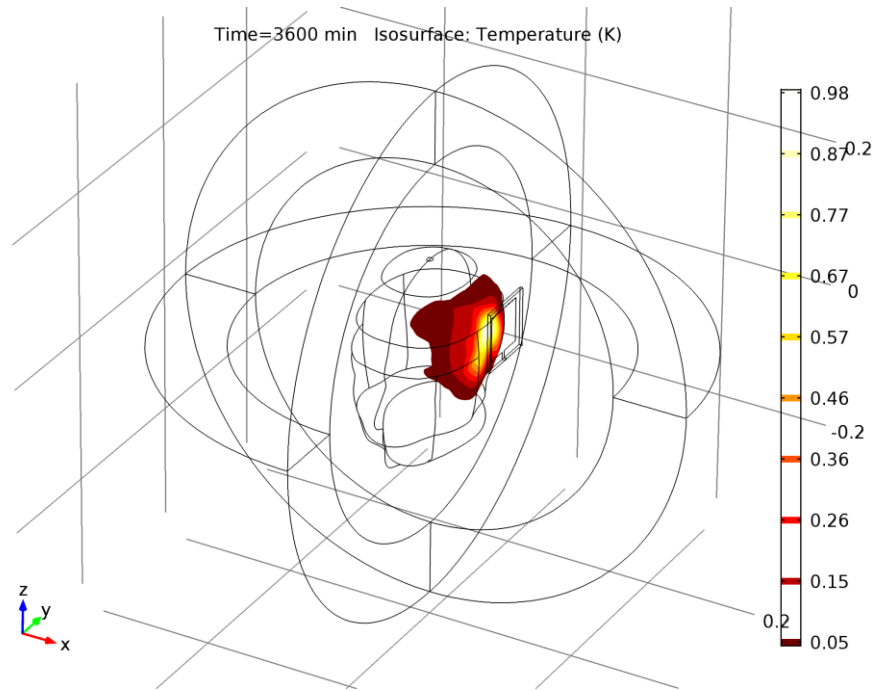


Figure 6.8. First CDR simulation heat distribution on SAM in iso-surface representation.

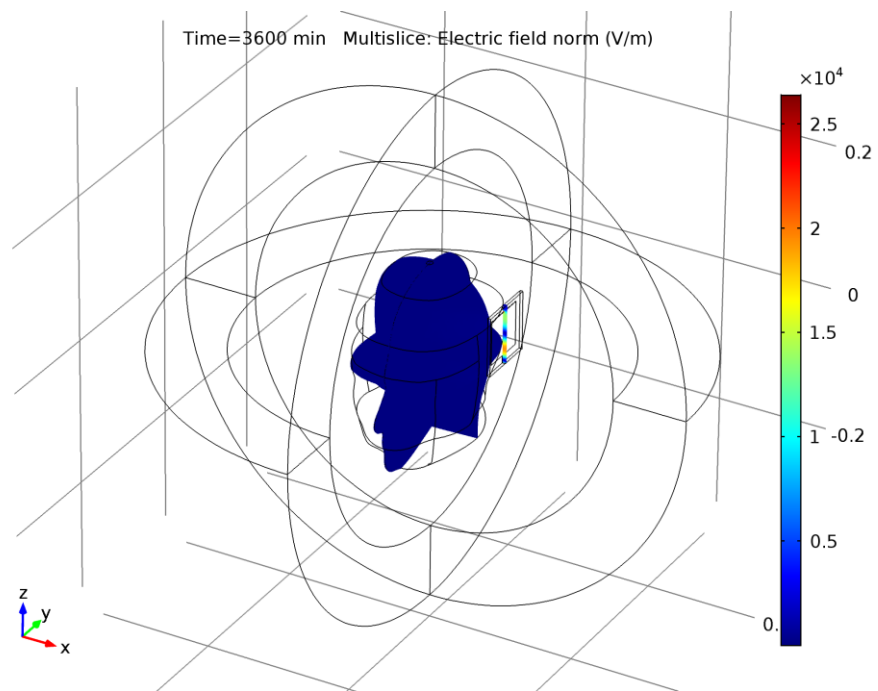


Figure 6.9. First CDR simulation's 1st radio source born electric field norm in multi-slice representation.

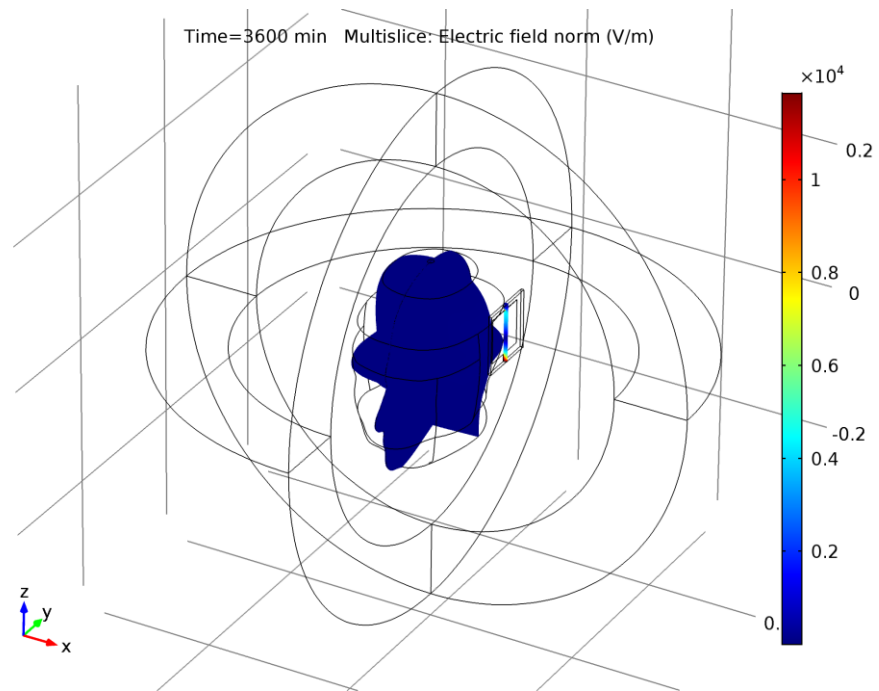


Figure 6.10. First CDR simulation's 2nd radio source born electric field norm in multi-slice representation.

Table 6.1. First CDR simulation's parameter set.

Name	Value	Description
epsilon _r _pcb	5.23	Permittivity for the patch antenna board
epsilon ₀ _brain	58.13	Permittivity for the brain tissue
sigma ₀ _brain	1.15 S/m	Conductivity for the brain tissue
rho_brain	1030 kg/m ³	Density of brain tissue
Sdamping	2000	Sampling parameter
Edamping	4000	Sampling parameter
Soffset	-1 S/m	Sampling parameter
offset	-50	Sampling parameter
c_blood	3639 J/(kg·K)	Heat capacity of blood
rho_blood	1000 kg/m ³	Density of blood
odamping	1.08 x 10 ⁻⁶ 1/s	Sampling parameter
offset	7.8 x 10 ⁻⁴ 1/s	Sampling parameter
freqwifi	2.45 x 10 ⁹ Hz	Frequency-I
freqgsm	2.6 x 10 ⁹ Hz	Frequency-II

As shown in Figure 6.6, the mobile positioned at 10 mm away from the SAM model. The concurrent double radio utilization has increased the surface temperature as high as 1 °C as in Figure 6.7. Although the surface temperature has saturated in the 15th minute to a final distribution as in Figure 6.7, the isothermal penetration has continued till 25th minute to a final distribution as in Figure 6.8. The separate radio effects can be viewed in Figure 6.10 and Figure 6.11 for WI-FI and 4G radio irradiations, respectively. The close values of frequencies result in almost the same electric field norm distributions although they are not.

The results of the first simulation was encouraging in the sense that there is a certain heat effect and also penetration into the brain tissue. Using the MRI deducted data as shown in Figure 6.5, we have achieved sensible results and more importantly it draws our attention to another real-life usage case. Therefore, in the second step, we want to investigate the effects when the UE is in front position at a distance of 25 cm right across the face.

6.4. Multi-Radio Supporting UE Simulation – across Face

The possible usage of UE in lateral position across the face is a plausible scenario when video call, video sharing or interactive gaming like applications are in use. 25 cm distance from face is also a generally recommended visual gap for concentrated visual tracking. As a second step for virtual reality (VR) headset usage, we have placed the UE at around 5 cm distance from the face. For both distances, once again concurrent radio utilization is solved but this time without time-dependence.

In this second simulation, the concurrent radio resources positioned at 25 cm distance have negligible heating effects as shown in Figure 6.13 through Figure 6.17 while when positioned at 5 cm distance front part of the face has elevated levels up to 0.5 °C as shown in Figure 6.18 and 6.19. This may be that much important but unlike other tissue elements, eyes are cooled by blinking and from the corneal area while almost all other tissues utilize blood perfusion as for cooling. For eyes blood perfusion is at almost a constant temperature and the eyes are more susceptible to the effects of elevated temperatures since they also utilize atmospheric oxygen intake from corneal surface.

Having covered the CDR UE simulations, let us carry on with BS field EM measurements.

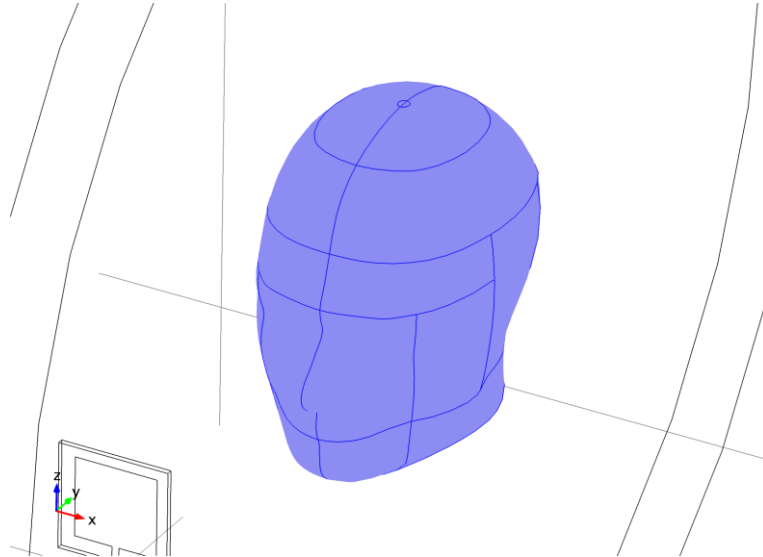


Figure 6.11. Second CDR simulation with blue biological tissue SAM relative to concurrent radio position.

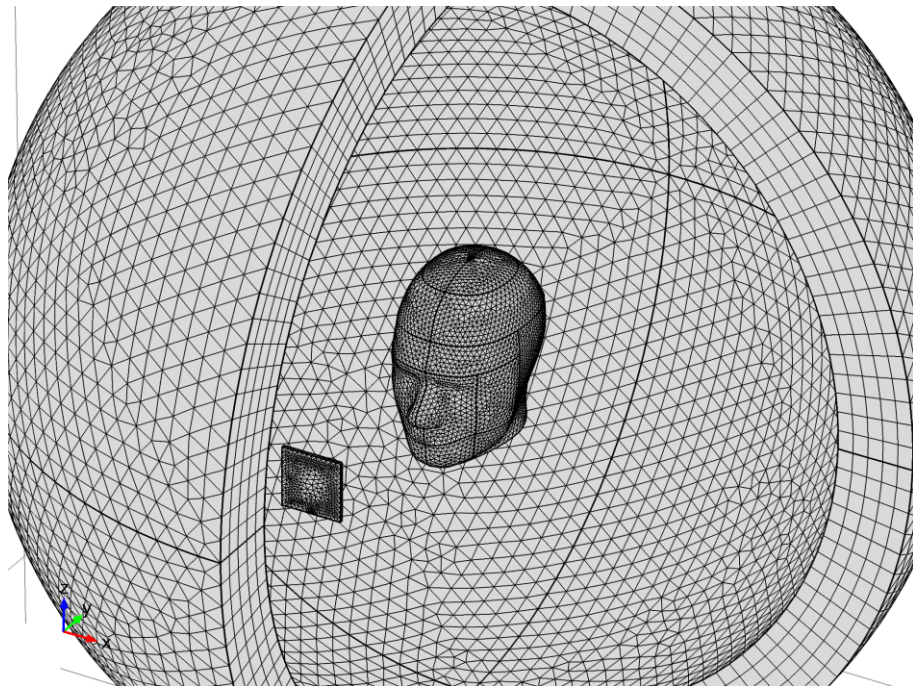


Figure 6.12. Second simulation FEM mesh structure.

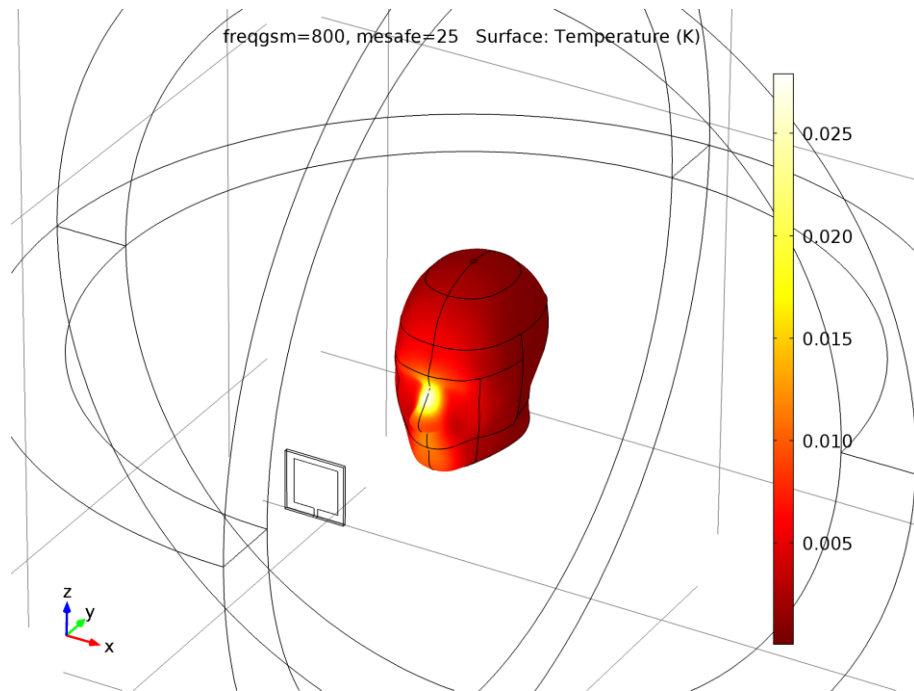


Figure 6.13. Second CDR simulation's heat effect by 800 MHz radio born electric field norm at 25 cm.

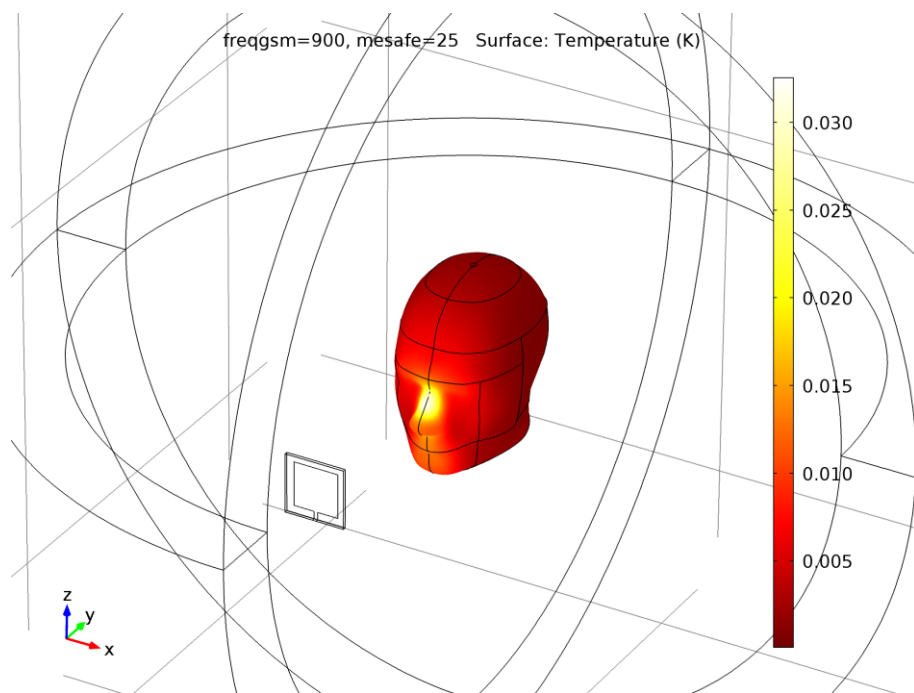


Figure 6.14. Second CDR simulation's heat effect by 900 MHz radio born electric field norm at 25 cm.

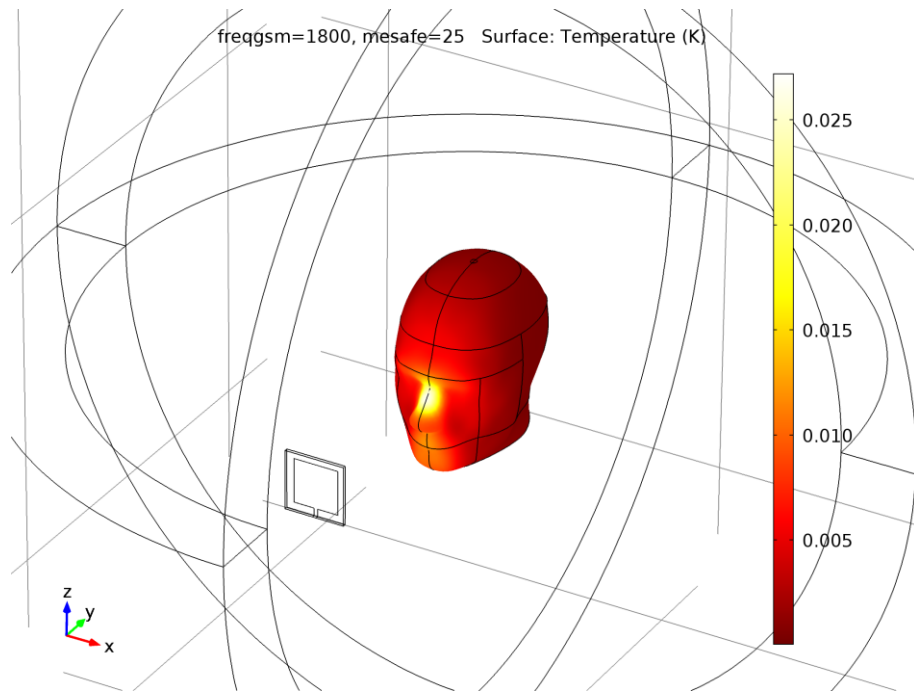


Figure 6.15. Second CDR simulation's heat effect by 1800 MHz radio born electric field norm at 25 cm.

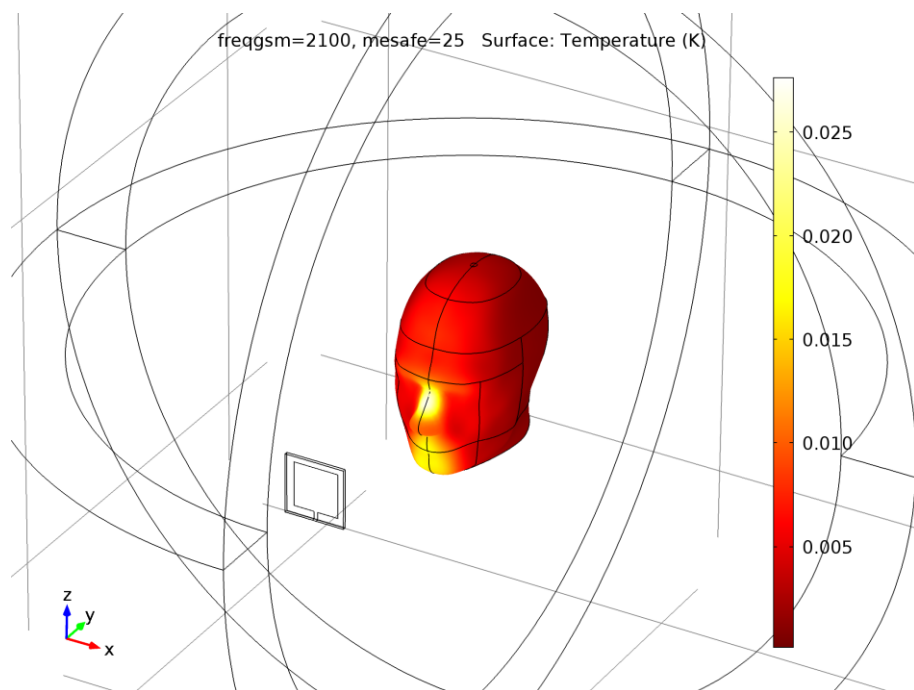


Figure 6.16. Second CDR simulation's heat effect by 2100 MHz radio born electric field norm at 25 cm.

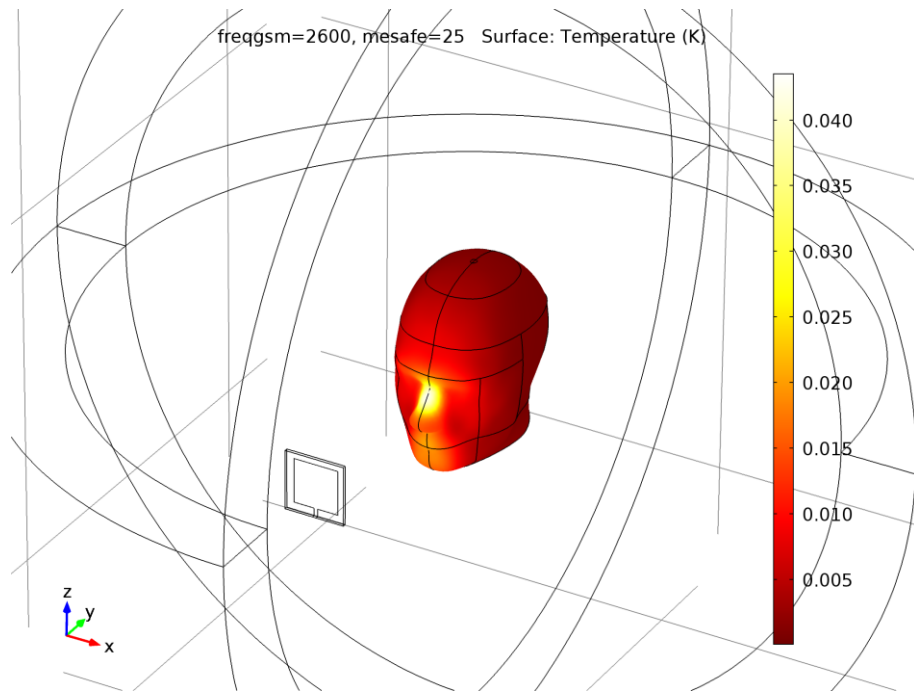


Figure 6.17. Second CDR simulation's heat effect by 2600 MHz radio born electric field norm at 25 cm.

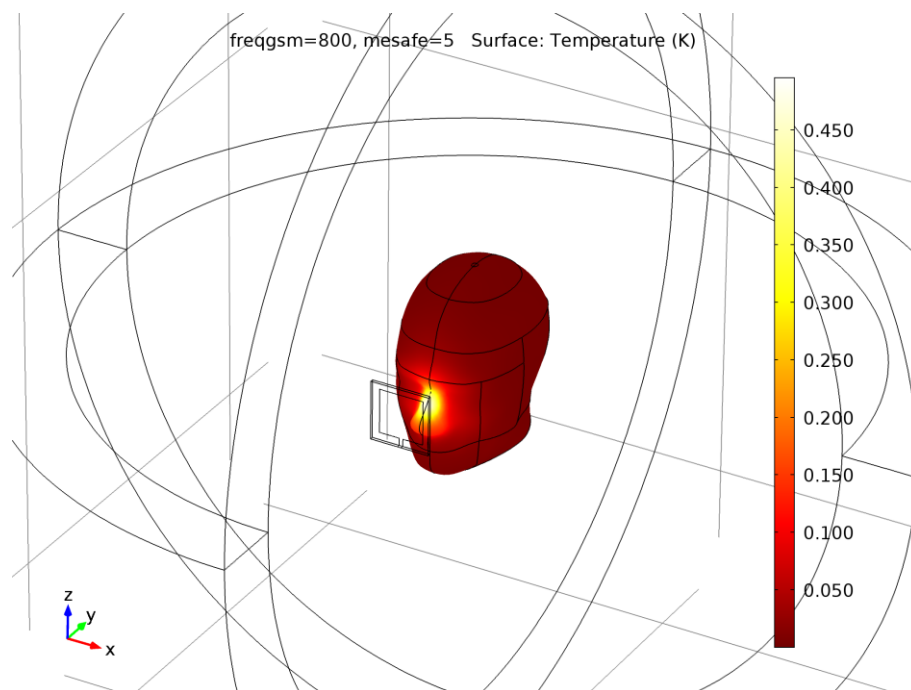


Figure 6.18. Second CDR simulation heat distribution with 800 MHz radio at 5 cm distance from UE.

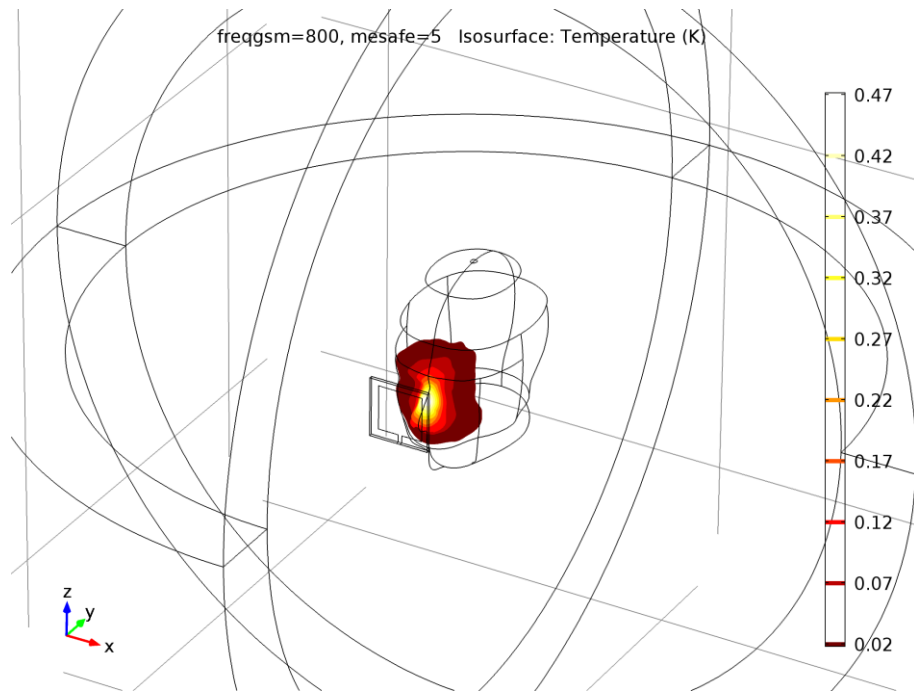


Figure 6.19. Second CDR simulation heat distribution with 800 MHz radio at 5 cm distance from UE with iso-surface representation.

6.5. Base Station EM Exposure Measurements

BS is one of the most critical nodes between the Mobile Telecommunication Network and the EU. The web of BSs forms the Mobile Radio Network (MRN) and it provides the wireless connectivity. Among the BSs, multi-operator co-sited urban sites are the apex of the EM exposure.

There are three active Mobile Network Operators (MNOs) in Turkey with all of them operating on 2G, 3G, and 4G licenses. For our measurements, 3 urban sites have been selected with all three MNOs co-exist with their 2G, 3G and 4G BSs operating at the same time. All operators could use 800 MHz 3G and 4G, 900 MHz 2G and 4G, 1800 MHz 4G, 2100 MHz 3G and 4G, and 2600 MHz 4G with minor frequency differences according to their bandwidth allocations [10].

Multiple measurements have been conducted in each site. The active bands were recorded and a cumulative electric field value was measured. All measurements were

conducted at 3 m in front of the antenna and 1 m behind the antenna, and the highest value was noted. We have also sampled horizontal readings to get some insight on the possible electrical tilts and reflections as shown in Figure 6.20 [10]. These horizontal samplings were instrumental to have an idea on electrical tilts and helped us develop an understanding of the reasons behind EM hot spots. Horizontal samplings over the antenna central axis were not required, since the electrical tilt antennas do not support upward tilts and the mechanical tilt apparatus for the older generation antennas do not have the mechanism for it [10].

The Narda SRM-3006 | 9 KHz-6 GHz Spectrum Analyzer with 3-Axis 27 MHz-3 GHz E-field antenna and the Narda NBM-520 | 100 KHz-6 GHz with EF0391 probe were the devices used for the measurements. The spectrum analyzer observations helped detect the active spectrum, while the E-field strength in V/m were measured by the probe-based device.

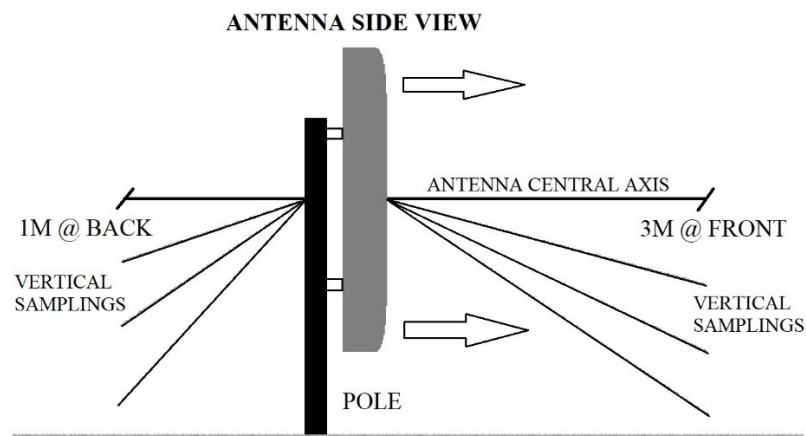


Figure 6.20. The antenna measurement approach.

The antennas are colored according to the operator designations. All antennas of a designated color must irradiate outwards from their monopole, which is represented with a circle, or out towards the nearest roof edge as in Figure 6.21. A sample spectrum analyzer output is provided in Figure 6.22, with active bands at 800 MHz, 900 MHz, 1800 MHz, and 2100 MHz with weaker signals at 2450 MHz and 1200, 1300, 1600 and 1750 MHz probable RADAR signals.

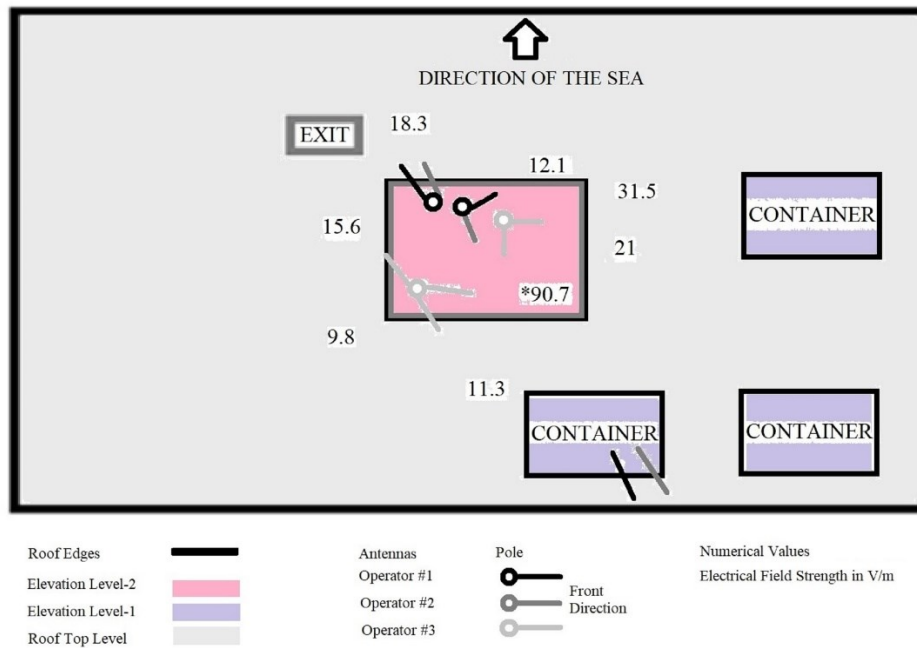


Figure 6.21. The bird's view roof-top sketch with measurements in a site.

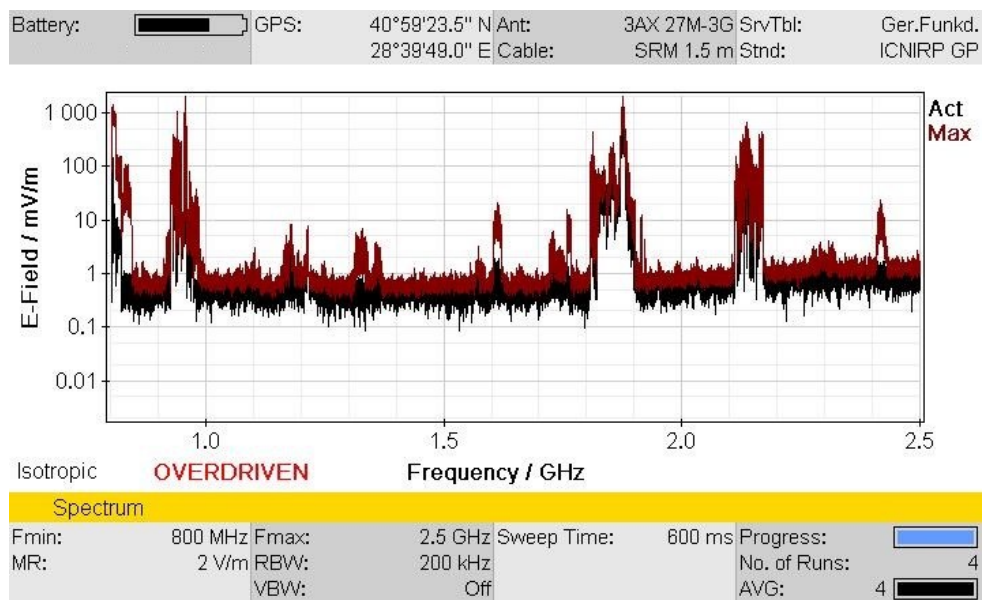


Figure 6.22. The spectrum analyzer output in a site.

It is important to note down that the all sampled sites had mostly combo antennas encapsulating up to 4 independent cross-polarized antennas. There were monopoles and multipoles hosting between 3 to 15 the antennas. There were also diverse differences between the roofs. Some roofs were flat; some other roofs had multiple elevations and

inclined surfaces [10]. 2G antennas had mechanical tilts, which could easily be detected visually. But it was not possible to detect the exact electrical tilt angles with external measurements alone. One can see the ultra-dense antenna environment in Figure 6.23 [10].



Figure 6.23. A multi-operator multi-technology site.

6.6. Occupational EM Exposure Risks in BS Maintenance

Our observation of dense antenna environment of multi-technology multi-operator BS sites in very close proximities and high level of electric field strengths has led us to investigate the operation and maintenance cycles of such BSs. In Table 6.2, typical roof-top maintenance and operation statistics are provided for top seven activities. The maintenance people who work in this EM environment perform these mentioned tasks that require between 5 to 40 min of dedicated effort inside the antenna cluster. Therefore, it is not possible to calculate exposure without the statistics of the roof-top maintenance works.

Since MNOs do not have coordinated maintenance activities and there is a strong regulatory pressure for MRN availability, it is vital to provide an occupational EM exposure guidance for the maintenance people. Recalling from our measurements, and considering the increased data traffic demand of customer, it is quite reasonable to expect electric field strengths above 100 V/m on certain occasions. In our simulations, 100 V/m electric field

strength-based EM exposure had induced 10.35 W/kg SAR value over 1 g for an exposure duration of 15 minutes on the IEEE SAR model at 2.45 GHz [10].

Table 6.2. Urban roof-top fault recovery and maintenance statistics.

Fault Type	Instance	Maintenance duration
Antenna	0.1/site/year	40 min
Connector	20/site/year	5 min
Feeder cable	2/site/year	40 min
Remote radio unit (RRU)	50/site/year	20 min
RRU power	0.3/site/year	30 min
Minor civil works	2/site/year	90 min
Major civil works	1/site/year	180 min

There was no prior academic study on the roof-top antenna close vicinity EM exposure. In one study, Baltrėnas et al. measured flux density changes at 15 m with an empirical probe governing far-field distance deduction from antenna front lobe radiation [76]. In another study, Haipeng et al. mentioned BS's EMR exposure to be limited and regulated by taking frequency, distance, main and minor lobe ranges, surroundings, tilt angle, and time of relevant factors into consideration such as traffic demand and co-site [77]. Therefore, the exposure guidance should have certain factors. We have set these factors as antenna spread, number of elevations on the roof, and the number of combo antennas per site. The antenna spread is classified into 3 types as: side-spread, concentrated cluster, and randomly spread. The elevation on roof is classified as flat or as the number of elevations. And the final factor is plain forward number of combo antennas per site. Accordingly, we propose the increased occupational EM exposure risk for maintenance people on above factors as:

$$XR = E \cdot C \cdot S \cdot ET \quad (6.1)$$

where XR is the increased occupational risk, E is the number of elevations, C is the combo antenna risk ((average combo antenna ratio per site + (1 – avg. combo antenna ratio per site)) x 3), S is the antenna spread risk (side-spread = 1; concentrated antenna cluster = 10; rand.

spread antennas = 3), and ET is exposure time risk $((1 + \text{ratio of co-sited base station ratio in maintenance area}) \times (\text{no. of co-sited base station ratio in maintenance area} / 50))$. The maintenance teams were responsible for 50 sites in their area so we took that number as the nominal value of the occupation [10].

As a conclusion, the people working in the maintenance urban multi-operator multi-technology sites may be exposed EM radiation in dangerous ways not considered before. Thermal effects are still acceptable for short durations, while organ specific exposure and nonthermal effects should be separately studied.

7. ORGAN SPECIFIC SIMULATIONS

The field measurements have taught us a good lesson. There are rare but specific exposures when the standard model may not be adequate as in the BS maintenance occupation. With unseen electrical tilts and unknown number of active antennas hidden in a single radome, there is certainly a risk for uneducated people working in dense combo antenna clusters. For these reasons, the model should be target specific.

For specific simulations such as the EMR effects on eye tissue, we have advanced the base IEEE SAR model in two different ways. Firstly, FEM model is advantages over FDTD for ocular shapes and the standard SAM does not contain an eye specific definition. So, we have utilized a very accurate three dimensional (3D) eye model we have found on the web [78]. This model has been stripped from the inner details and introduced into the SAM from physical volume, intrinsic conductivity and permittivity point of view. Secondly, we still utilized the blood perfusion rate as of the brain's since in our simulation unlike the common practice of increased eye blood perfusion rate of models with specific calculations of eye. In our model, eye is thermally insulated on the surface and instead of acting as a cooling boundary, it is neutral in that sense. There is no need to further detail it at this moment since we will discuss the reasons with the simulation model and simulation results.

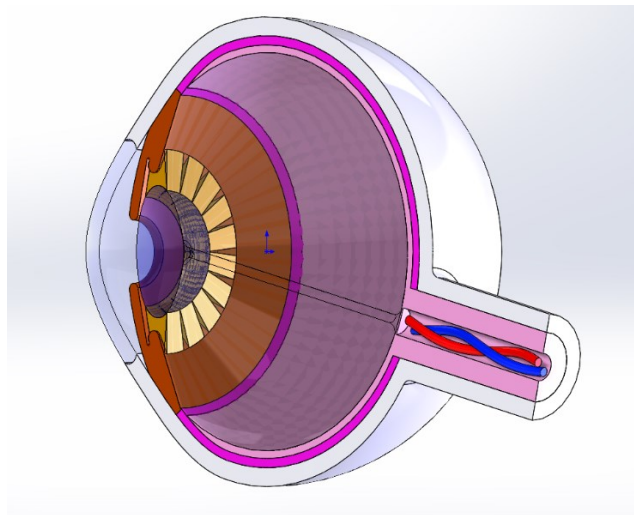


Figure 7.1. An oblique view to the 3D eye model used [78].

The eye model is only utilized as a single volume element to decrease computational load. Thus, we have used two sets of conductivity (σ) and relative permittivity (ϵ_r) to understand the effects representing the eye as if it is sclera only (lower water content) or vitreous humour only (higher water content) (Table 7.1 and Table 7.2).

Table 7.1. Tissue Conductivity Values (S/m).

Frequency (MHz)	Sclera	Vitreous Humour	Brain
800	1.130272	1.608266	0.730524
900	1.166726	1.636162	0.766504
1800	1.601727	2.032478	1.15308
2100	1.789117	2.221833	1.310172
2300	1.925249	2.363649	1.422798
2450	2.033048	2.478094	1.511336
2600	2.145607	2.599401	1.603296

Table 7.2. Tissue Relative Permittivity Values.

Frequency (MHz)	Sclera	Vitreous Humour	Brain
800	55.561417	68.925781	46.251328
900	55.27013	68.90184	45.805496
1800	53.567787	68.573364	43.544899
2100	53.125057	68.417976	43.054611
2300	52.839252	68.301758	42.754364
2450	52.627628	68.208023	42.538925
2600	52.417377	68.108711	42.329929

7.1. Multi-Radio Supporting UE Simulation – with Eyes

The eyes' domains are positioned on a symmetrical base into the SAM model based on the peripheral dimensions as in the Figure 7.2. We have taken certain assumptions in order to simulate a VR headset model. First of all, VR headsets utilize optical elements and there is not enough room for ventilation of the eyes. Secondly, most VR headsets are almost hermetically sealed for a good video experience and limit the airflow inside. The lack of ventilation for light isolation purposes in headset is going to saturate the air in the headset in steady state conditions in terms of vapor pressure, and there will be little or no evaporation from corneal surface. The UE or namely, the smartphone (SP), also produces heat towards the face by its display. Likewise, the oxygen in the encapsulation will be saturated to be useless for eyes as the amount of carbon dioxide reaches a steady state value. In our samplings, we have found out that SP VR headset inner volume was equal or less than 15 cm³.

There is also a verified relation between attention and blinking rate [79-83]. During periods of increased cognitive load and focus on objects in the environment, the blinking rate decreases [80, 83, 84]. Another study found decreased blinking rate during video terminal usage [84]. A VR environment not only increases the focus on objects, but also maximizes the cognitive load on the occipital and frontal lobes [81, 82, 83]. Nonetheless, if emotional stress is also involved, the blinking frequency has a strong correlation with the stress level [82, 85]. Recalling our thermal isolation assumptions, the blinking would have marginal effects in a saturated vapor pressure environment. With the extra effects of decreasing blinking rates [80-84], it is quite a fair approximation, since the vapor pressure saturation may be achieved earlier in real world conditions than simulations. Therefore, by the nature of the application, we assume the blinking rate is going to drop. For these above reasons, we have taken the eye-air boundary as thermal insulation. Finally, we have totally neglected eye movement in VR usage.

ICNIRP sets 1.5 °C increase as a limit for lens protection. 41-43 °C range poses lens opacification risk [86]. On the retinal part, retinal temperature increase is safe at 0.25 °C at most by former retinal prosthesis research [87]. Certain retinal side effects such as retinal whitening, edema, and fundus lesions can be observed with temperature rise over this value

up to 2 °C from cadaver and FEM studies. Therefore, 2 °C can be taken as a damage threshold level for retina [87].

There has been extensive academic research on human eye temperature distribution [88-93]. Infrared detection, which is the most recent and non-invasive empirical technique, has shown that the cornea surface temperature for human eye can be referred as 34.3 °C [89]. Similarly, the retinal blood temperature can be referred as 37 °C [89, 92]. We have set the initial conditions of the simulation respective to these figures, which have a great effect on the outcome for different domains.

Since we simulate two radio transmitters concurrently operating, we utilize the corresponding conductivity and permittivity values for selected tissue of the eye (Figure 7.3 and Figure 7.4 for sclera). The blood perfusion rate of eye has been taken same as brain. In these studies when blood acts as a heat source for eye, taking a higher value of blood perfusion for retinal area may seem reasonable. For our case, retinal blood perfusion is a heat sink instead of being a heat source; thus, we preferred to keep it the same with the brain value.

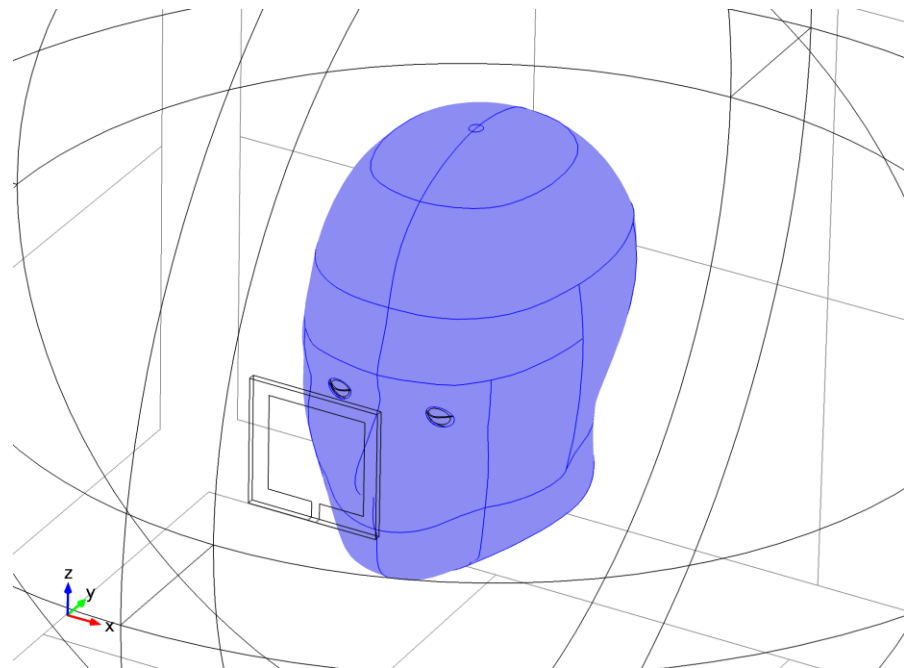


Figure 7.2 Third CDR simulation with 5cm distance radio sources and eyes in the phantom.

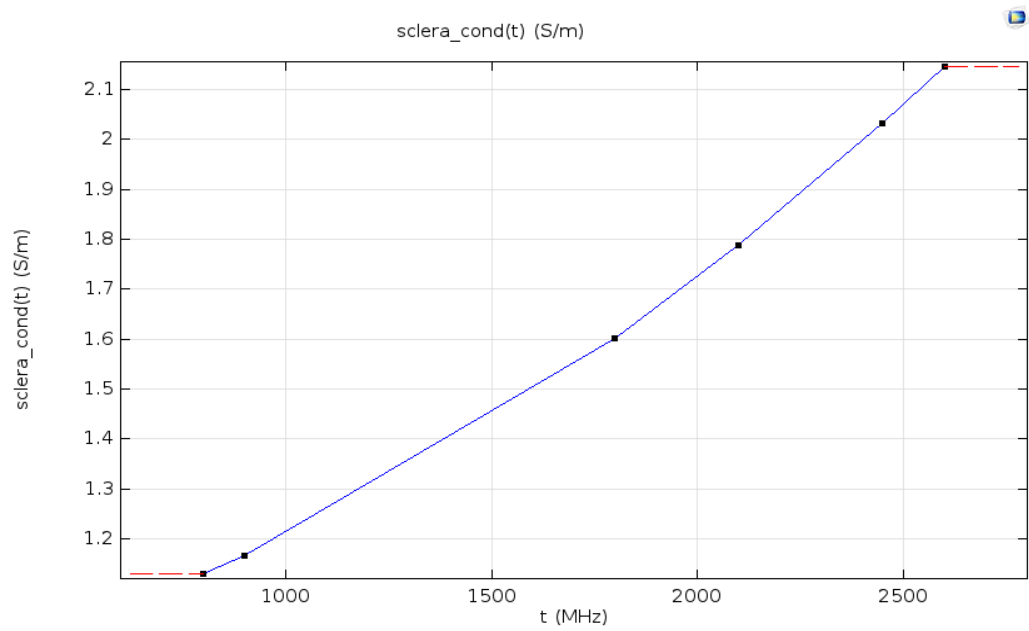


Figure 7.3. Third CDR simulation sclera conductivity of the phantom with frequency.

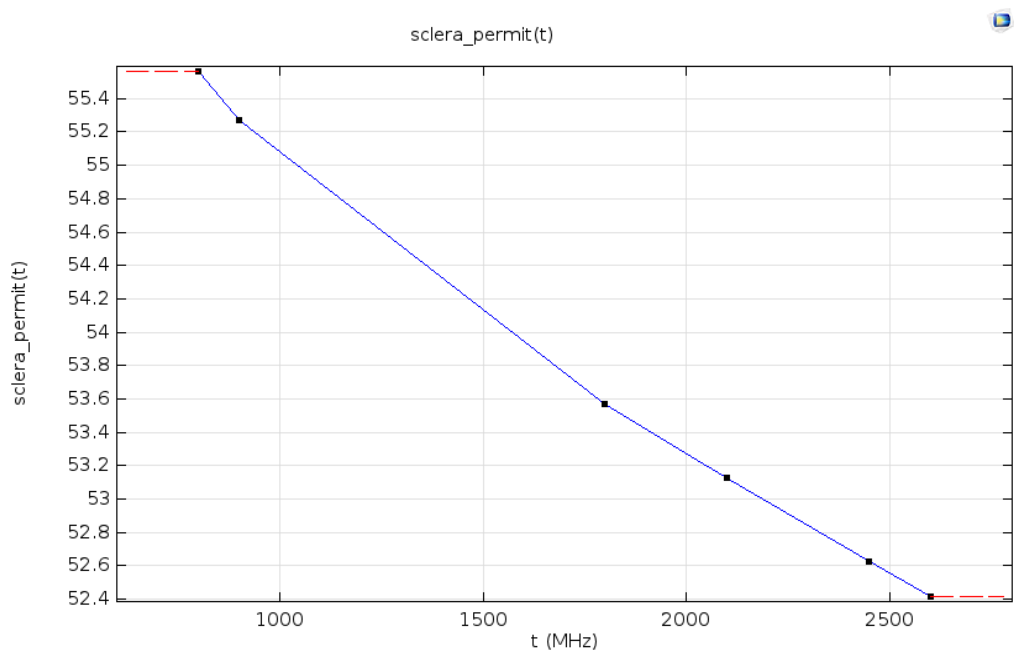


Figure 7.4. Third CDR simulation sclera permittivity of the phantom with frequency.

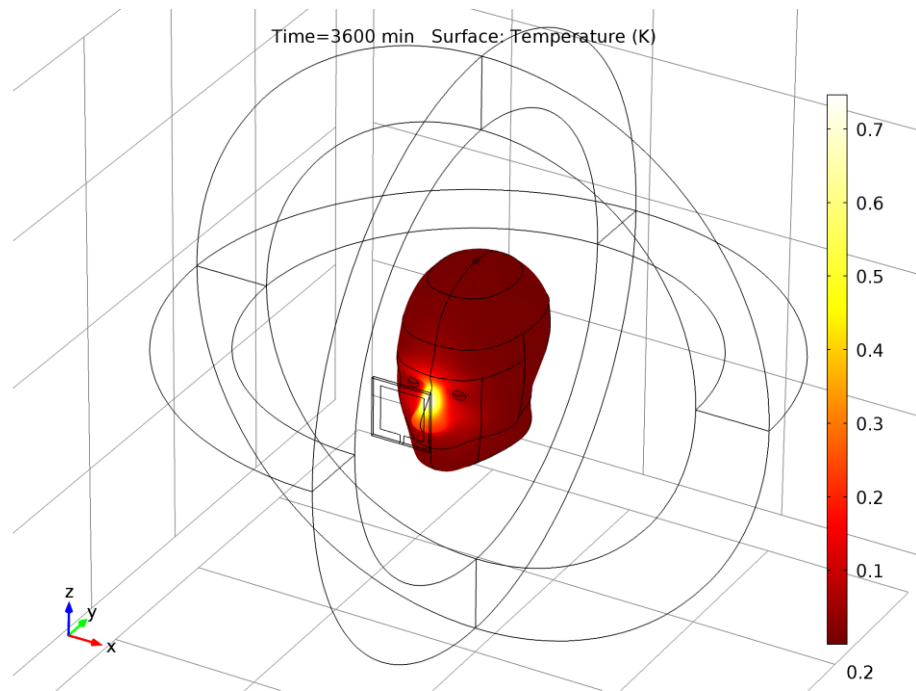


Figure 7.5. Third CDR simulation temperature plot with concurrent 2450 and 2600 MHz sources.

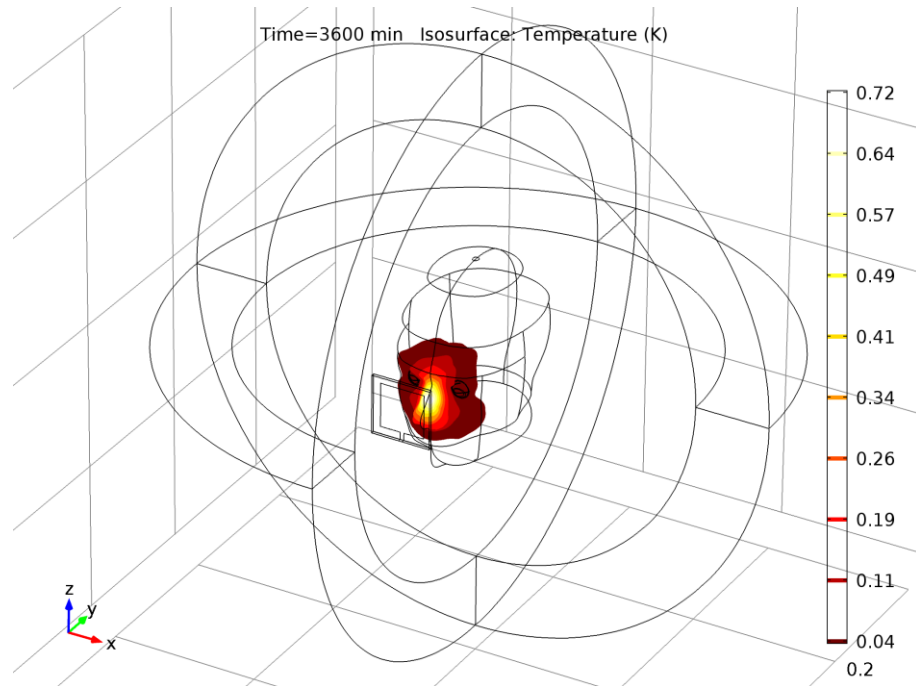


Figure 7.6. Third CDR simulation iso-surface temperature plot with concurrent 2450 and 2600 MHz sources.

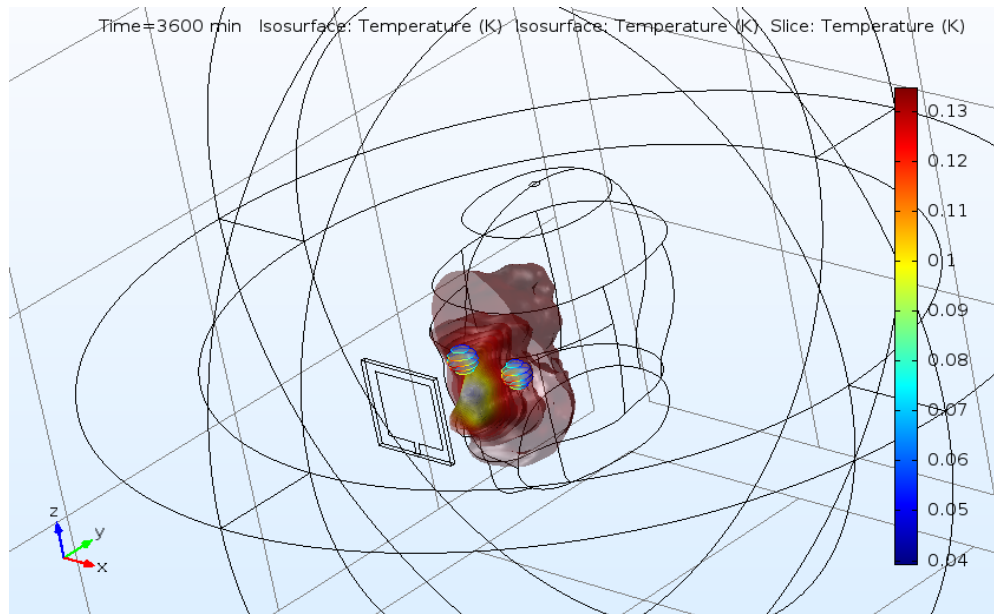


Figure 7.7. Fourth CDR simulation iso-surface temperature plot with concurrent 800 and 2600 MHz sources with transparent view of face and eye domains.

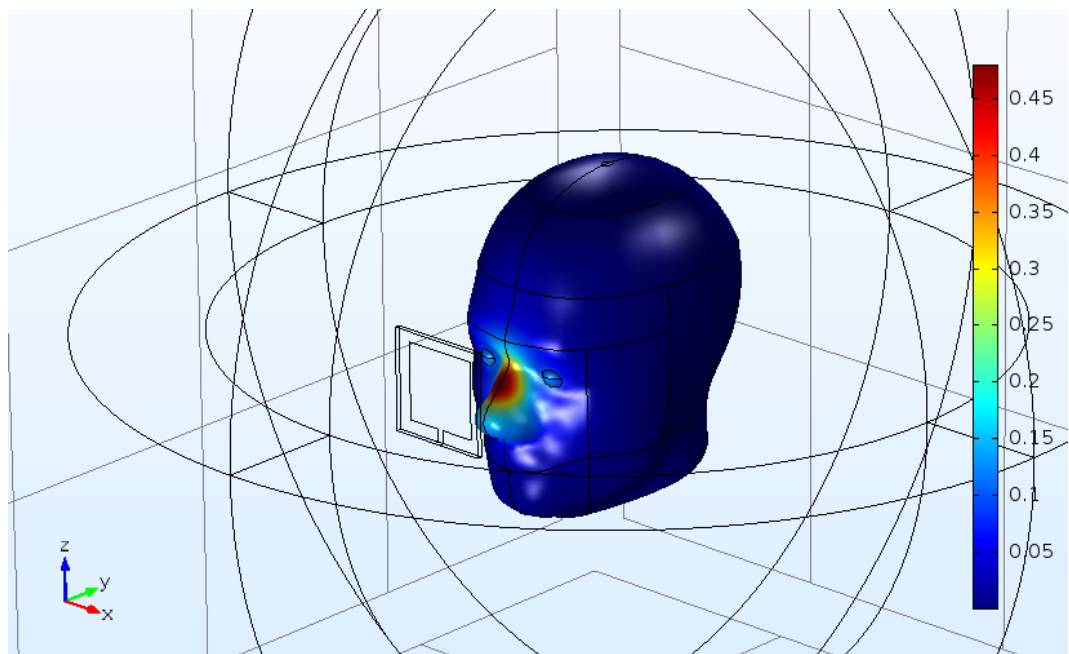


Figure 7.8. Fifth CDR simulation surface temperature plot with concurrent 800 and 2600 MHz sources of face and eye domains.

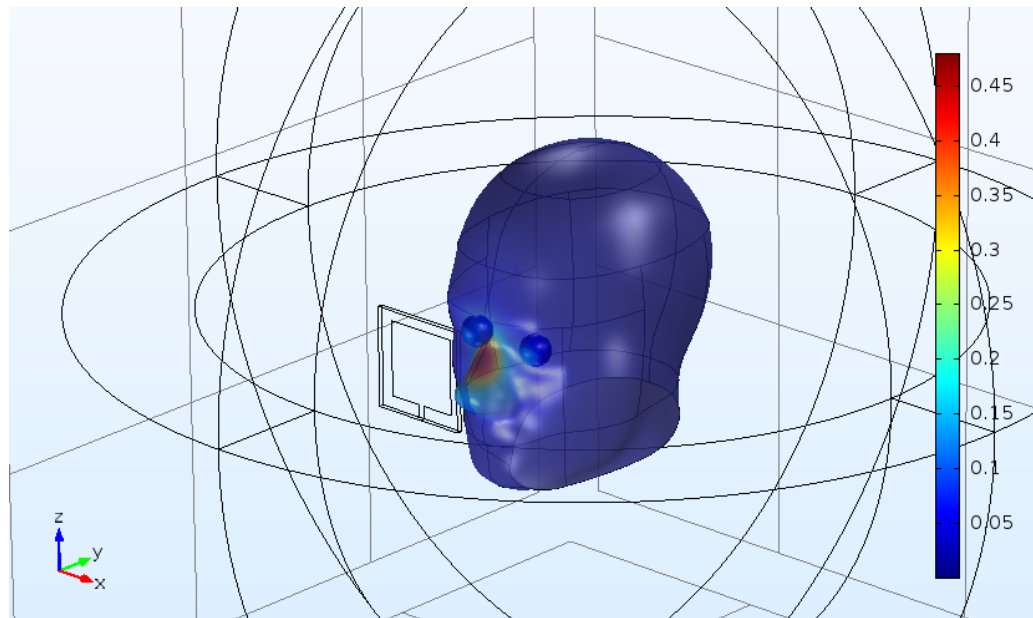


Figure 7.9. Sixth CDR simulation translucent temperature plot with concurrent 800 and 2600 MHz sources of face and eye domains.

The eye is cooled on the retinal side by the blood perfusion, and $0.25\text{ }^{\circ}\text{C}$ is a limit for biological damage in case of retinal implants [87]. So, the retina base temperature can be accepted as $37\text{ }^{\circ}\text{C}$. The other cooling on the front interface is by the cornea. The cornea evaporation rate and blinking rate are the key factor in the cooling process. The cornea temperature is almost fixed around $34.3\text{ }^{\circ}\text{C}$. If there is excessive heat exposure on eye, the lipid layer on cornea is torn and the evaporation rate increases. But this does not work in our case because of the saturated vapor pressure issue.

Sampling the smartphone based virtual reality headsets, we have also simulated distance for 2, 3 and 7 cm from the face in addition to 5 cm. The CDR simulation was kept the same and the results were slightly higher than before. First of all, when the distance was closer, the temperature levels were higher both on cornea and retina. Secondly, we have made the technological check and have found that double radio supporting smartphones always used one radio for the ISM bands. So, the simulations of closer frequencies show more elevation in the eye such as 800-900 MHz or 2450-2100 or 2450-2600 MHz. But more interestingly, since the propagation was closer to the eyes, the eyes' sides toward the nose were awkwardly getting warmer (see Figure 7.11). All the simulation results, for central and oblique antenna scenarios with all the distances can be seen in Figures 7.12 and 7.13.

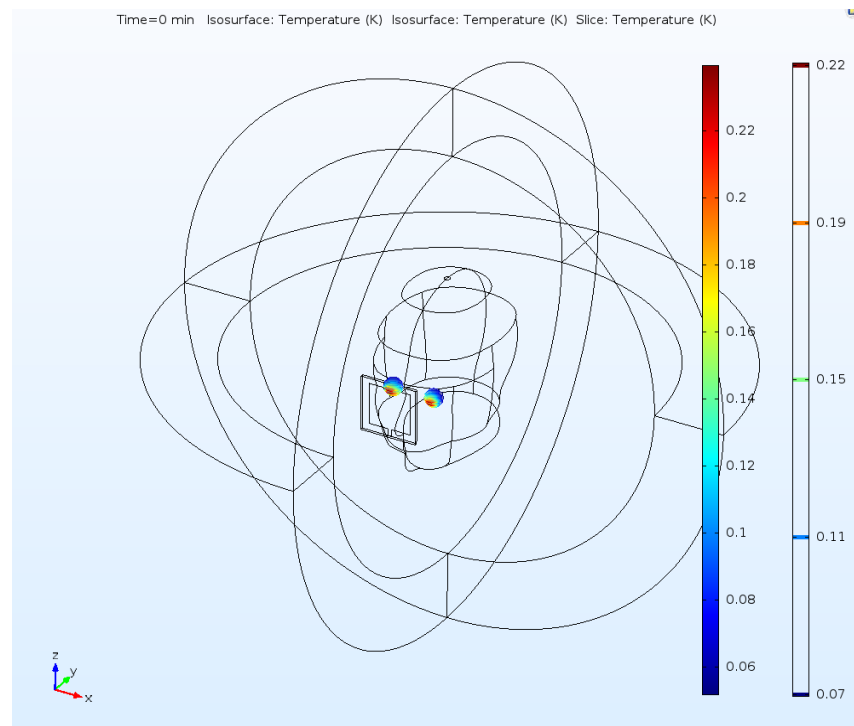


Figure 7.10. Seventh CDR simulation translucent temperature plot with concurrent 2450 and 2600 MHz sources of face and eye domains.

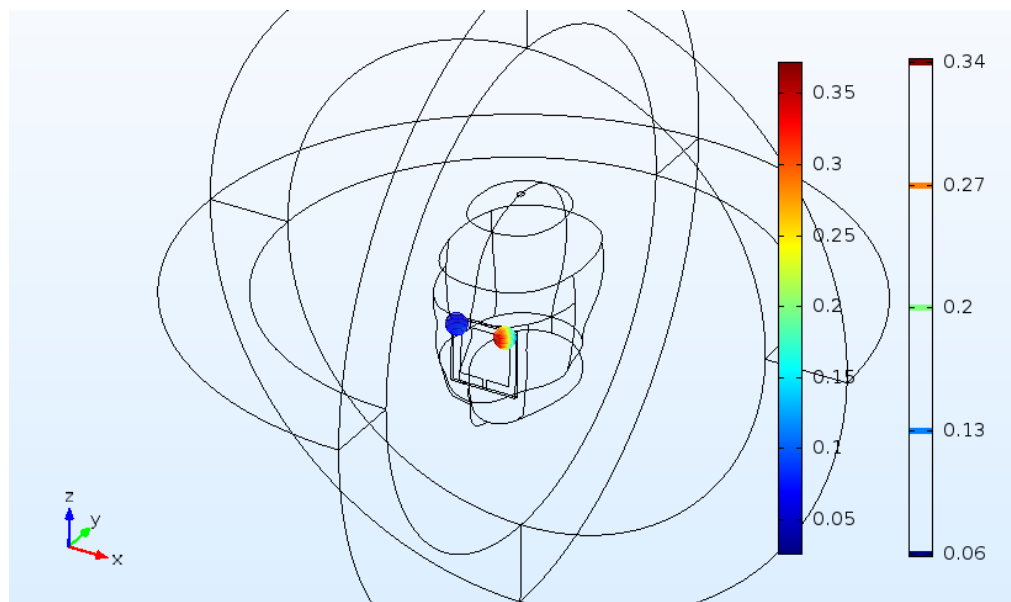


Figure 7.11. Eighth CDR simulation temperature plot with concurrent 2450 and 2600 MHz sources of eye domain with oblique antenna exposure.

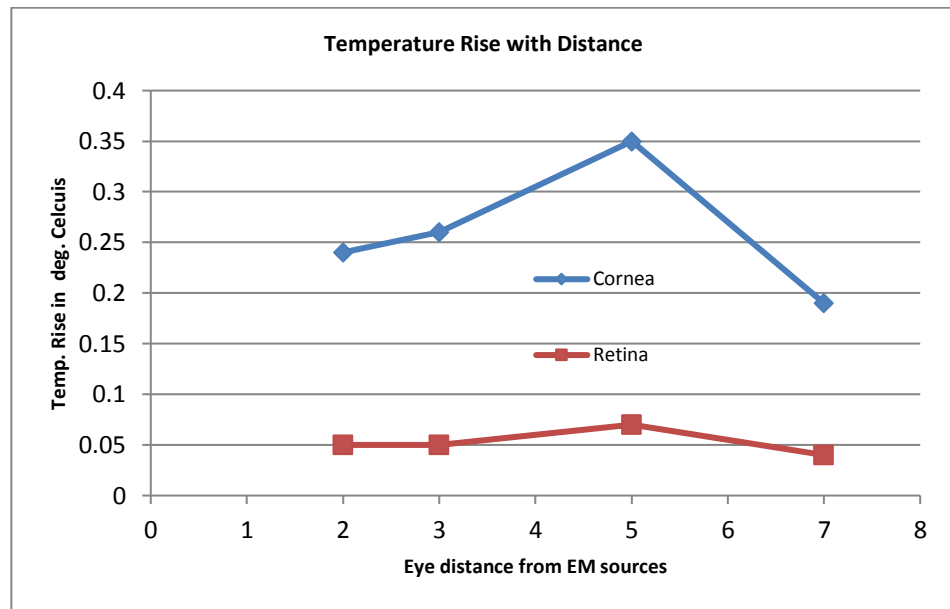


Figure 7.12. Temperature rise plot in human eye modelled as vitreous humour tissue exposed to 2600 MHz-2450 MHz EM sources at varying distances with centralized antennas.

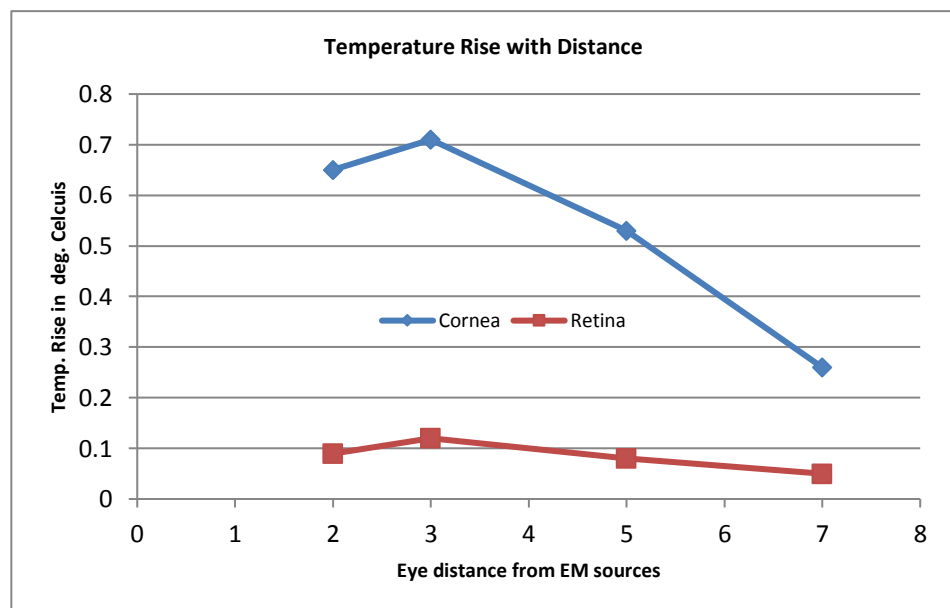


Figure 7.13. Temperature rise plot in human eye modelled as vitreous humour tissue exposed to 2600 MHz-2450 MHz EM sources at varying distances with side antennas.

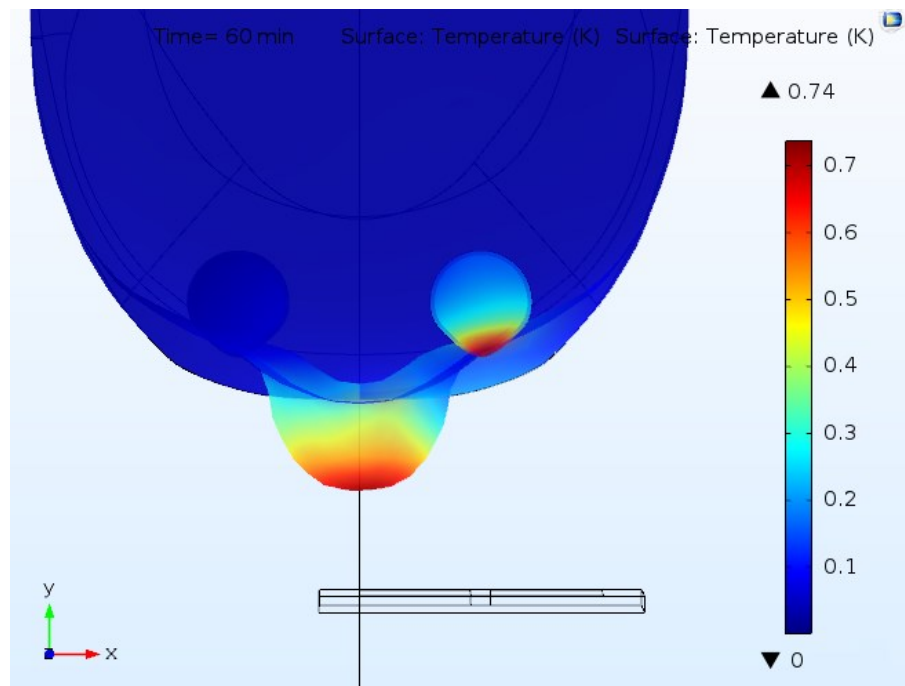


Figure 7.14. Transparent top-down view temperature rise plot in human eye as vitreous humour tissue exposed to 2600 MHz-2450 MHz EM sources on side at 3 cm.

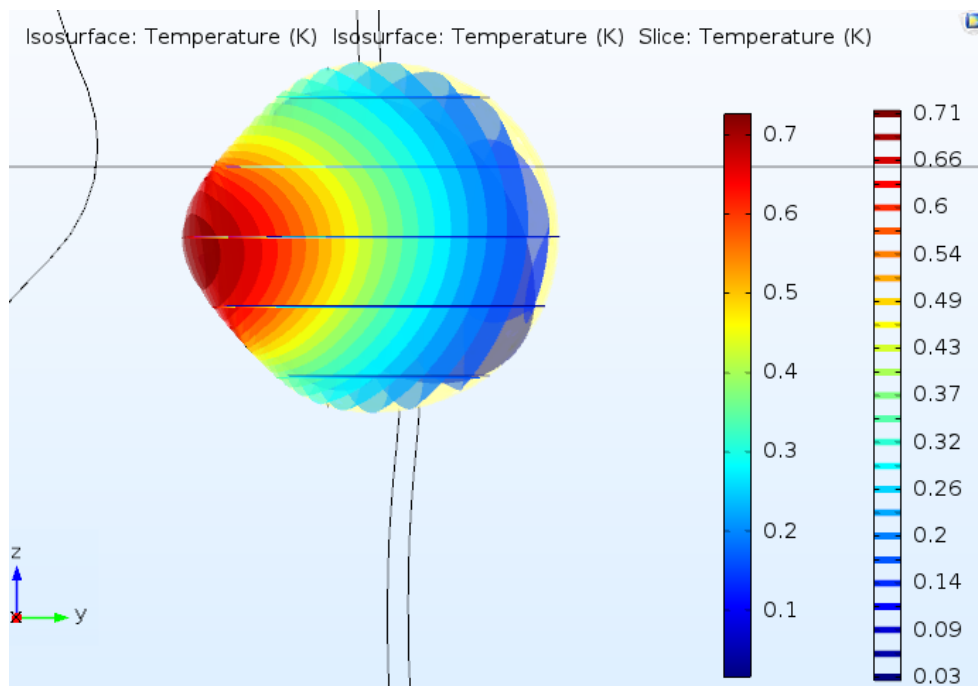


Figure 7.15. Side-view 25 slice iso-surface temperature rise plot in human eye as vitreous humour tissue exposed to 2600 MHz-2450 MHz EM sources on side at 3 cm.

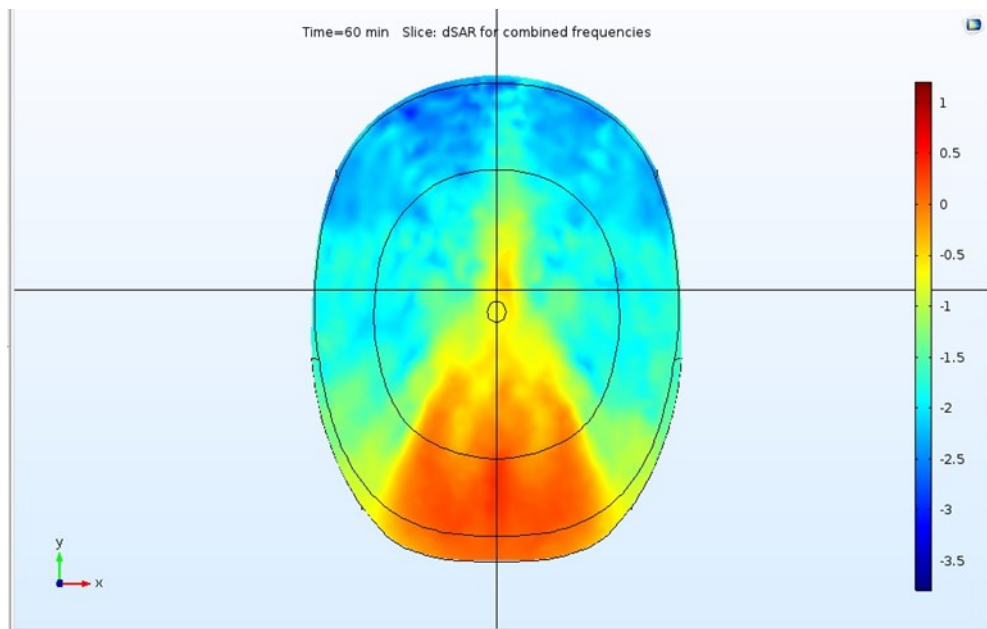


Figure 7.16. Logarithmic SAR values on x-y plane with $z=2.5$ cm by 2600 MHz-2450 MHz CDR with central antennas at 5 cm distance.

The simulations have shown interesting results. The corneal temperature increase has reached 0.35 °C at the distance of 5 cm from face with 2600-2450 MHz pair in the central antennas' scenario (Figure 7.12). In the side antennas scenario, the corneal temperature increase has further reached 0.7 °C at the distance of 3 cm from face with 2600-2450 MHz pair (Figure 7.14). It is important to note down that natural cornea temperature is 34.3 °C. So, there is a total increase of 3.05 °C with the central antennas and 3.40 °C with the side antennas, respectively. To assess this risk, one should consider other factors as blinking rate and evaporation rate. Let us recall that VR applications triggering high attention and high stress through SP VR headset may cause lowered blinking rates and elevated cornea temperatures based on our simulation results [81, 82, 83, 85].

The utilization of SP VR headsets for children may raise further concerns. Children up to age of 7 have bigger eyes relative to their head size, and they are more prone to the effects of EM radiation [86, 94, 95]. Our modified model provides the SAR penetration for the adult human head from SP VR headsets (Figure 7.16). Thus, one can assume higher SAR penetration for child head [94]. It is possible to oversize the eye domain in our model, and one can simulate SP VR headset usage of children to an extent, too. There may be non-thermal effects on hypothalamus, thalamus, and pineal glands (Figure 7.16) [94, 95, 96].

7.2. Conventional Mobile Call's Effect on HPA Axis

Now it is time to seek the answer for the conventional call and its probable effects on HPA axis. The UE is held near the head in a conventional call scenario. For that, the converged model has been modified with an EM source representing the conventional mobile use as in Figure 7.17. That side of the head is mainly exposed to the EMR from the MT. The academia has studied the MT EMR, and have found negative effects over endocrine, nervous and reproductive systems. Certain mechanisms have also been proposed for the explanation such as generation of free radicals, alteration of gene expressions, deoxyribonucleic acid (DNA) damage, and loss of chromosomal stability [97-114].

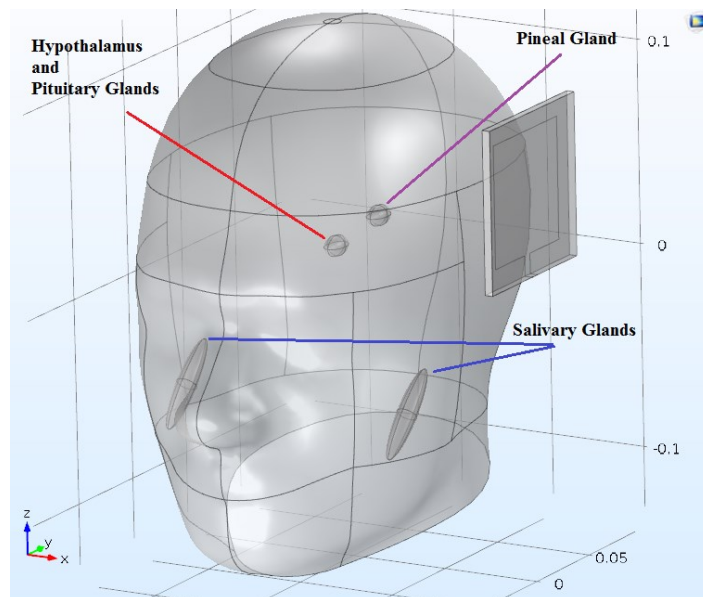


Figure 7.17. Simulation model with conventional call position.

There are also many epidemiological and biological studies of effects of EM over endocrine system and its glands [97-114]. Among these studies, the epidemiological studies make a clear discrimination between mobile user subjects in terms of duration of use. The most frequent outstanding duration is 20 minutes use [100, 109]. In some studies, this value may drop down to 10 minutes, while in others may go up to 60 minutes [100]. A second discriminatory factor is the total daily mobile use time of subjects. 1 hour per day seem to be a good threshold for the heavy user definition [100, 106]. A final discriminatory factor

is the years of mobile phone use of the subject, which often falls between 10-25 years [98, 102, 103, 107, 108].

We have simulated the EM thermal effects and electric field strengths on the salivary glands from the biological and epidemiological studies [97-109] according to these factors. The hypothalamus, pituitary and pineal glands have dielectric and permittivity properties similar salivary glands, but they cannot be investigated without invasive methods. Therefore, we have aimed to simulate the effects over the hypothalamus, pituitary and pineal glands and compare the results with those of salivary glands ones. For that, we have used our former model but with a side EM source. They have simulated the EM electric field strengths and thermal effects for the conventional mobile phone usage, and measured the values over all the glands. The findings on salivary glands are then compared with the findings on the hypothalamus, pituitary, and pineal glands.

Six sets of simulations were conducted with a side EM source on the modified IEEE SAR model using FEM with possible 4G and 5G frequencies at 700, 900, 1800, 2100, 2450, and 3600 MHz. 700 MHz and 3600 MHz are not necessarily common in other studies, but these two bands are the most popular new 5G bands allocated by the regulators; since all other bands are currently busy with 3G and 4G technologies.

The simulations have been solved in time-dependent fashion up to 60 minutes in order to find possible temperature saturation times together with the temperature elevation trend. Stationary solutions have also been solved in order to make sure that 60 minutes of exposure time will cover the final temperature saturation time. As for the electromagnetic source, the output is assumed to be a fixed-power continuous wave from a patch antenna [115].

The temperature elevations, the electric field strength and SAR recordings are shown in Fig. 7.18, Fig. 7.19, and Fig. 7.20, respectively. The HP and the pineal glands have higher temperature elevation, higher electric field strength, and higher SAR values than the salivary gland at 900 MHz. All three parameters are comparatively in similar range at 700 MHz and 1800 MHz. The salivary glands are more prone to EM exposure above 1800 MHz than the HP and the pineal glands.

All temperature elevations figures are in alignment with the literature and the regulations [69, 115-118]. As a result, SAR values do not exceed the standard limits. The temperature elevation saturation times are also under 10 minutes for all frequencies, which is safely within the benchmarks of clinical studies [101, 106, 109].

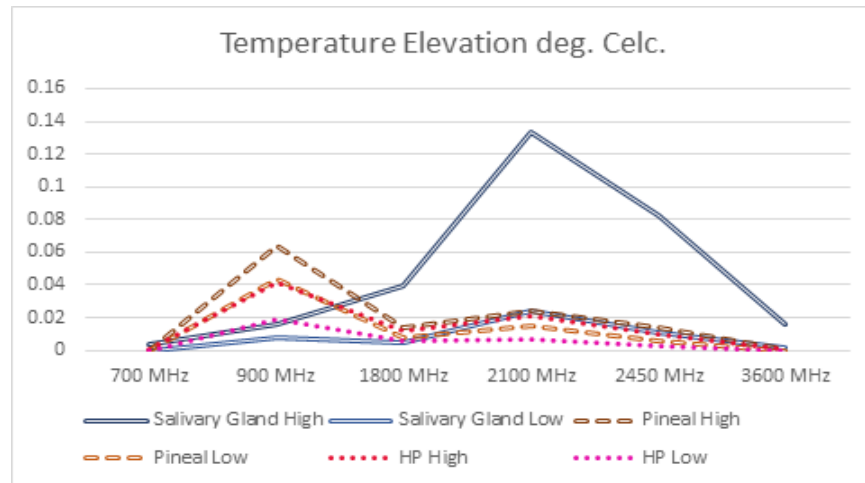


Figure 7.18. Temperature elevation recordings from simulations.

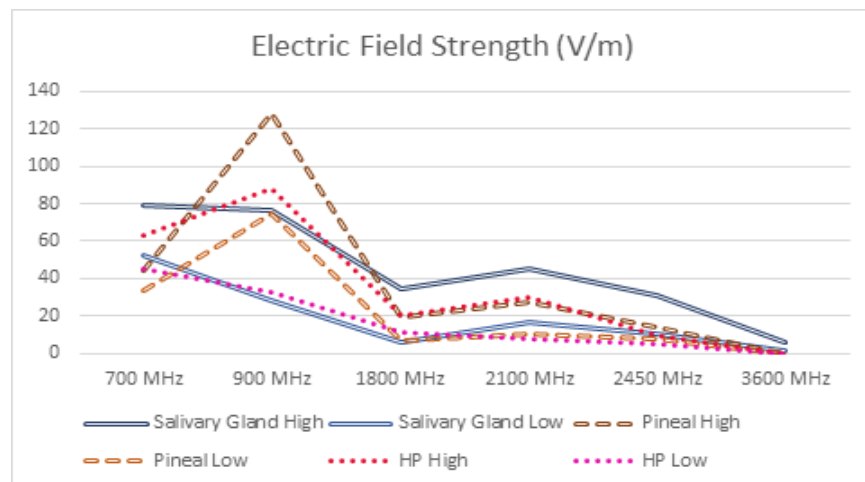


Figure 7.19. Electric field strength recordings from simulations.

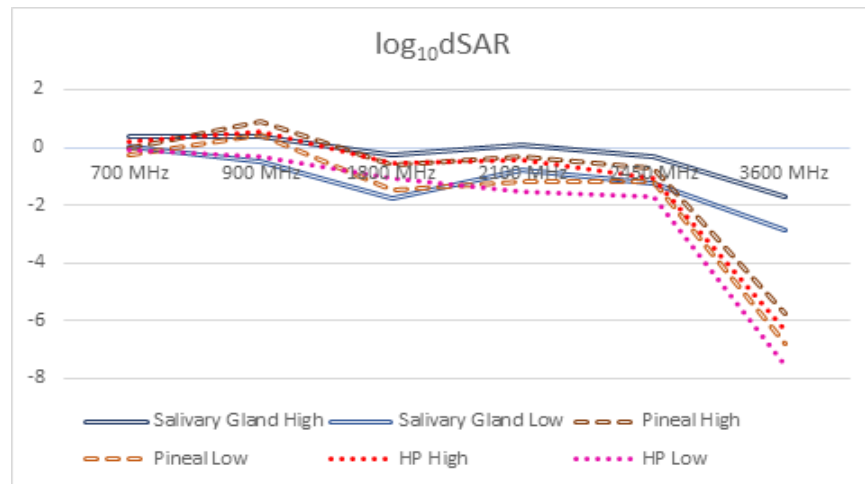


Figure 7.20. Logarithmic SAR recordings from simulations.

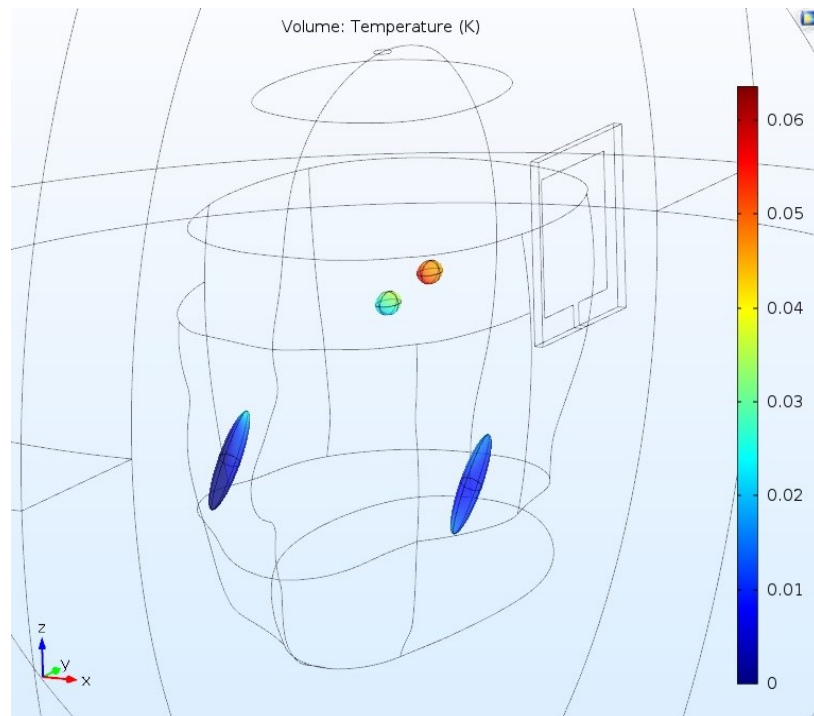


Figure 7.21. Temperature elevation (K) in HP, pineal and salivary glands at 900 MHz.

The cancer studies on brain claim an increasing risk from frequent mobile phone usage [94, 97-105]. Geronikoulou et al. have observed HPA axis response modification after mobile phone usage in children and adolescents [109]. Most of these studies fall into 900-1800 MHz range, where we have also observed similar effects on HP and pineal glands as

of salivary gland. If one considers higher power EM exposure as in [117], the risks would be expected to be higher, too.

7.3. Tumor Detection Possibility by UE Born EM

As a final step of our modified IEEE SAR, we have investigated the possibility of extremely aggressive intracranial tumors. Cancer is the second leading cause of death after ischemic heart disease in the world [119]. If one reconsiders the aging factor, the cancer may even become the most prominent cause of death. Among the cancers, intracranial ones are hardest to reach by topical, by intravenous, and even by surgical methods for the medical doctors. Therefore, radiotherapy and thermotherapy are used in concert with other therapeutic medicine [120, 121]. To increase the efficacy of these therapies, nanomaterials and laser stimulations are proposed [120-123], some of which modify the Blood Brain Barrier (BBB) and Blood Tumor Barrier (BTB) permeability. Some studies also propose blood conductivity improvements by carbon nanotubes and other metallic nanoparticles to increase the conductivity of tumor tissue [120, 123, 125, 126].

Glioblastoma multiforme (GBM) is a very aggressive intracranial cancer with a very high mortality rate [127]. World Health Organization (WHO) classifies GBM as a grade 4 tumor, which is most malignant [128]. This cancer usually grows in a star-like (astrocytic) shape and can only metastasize in brain [119, 125-129]. Therefore, it is of utmost importance to detect this cancer in its early stages.

GBM may trigger some symptoms based on its location and by its pressure. Abnormal breathing and fluctuating pulse, headaches that persist without relief, motor dysfunction, difficulty in speaking and fetching memories, dizziness, eyesight issues, seizures, and vomiting are common to brain tumors. One may expect to observe the symptoms in GBM case rather faster than any other brain tumor, both malignant and benign [126-129].

GBM has lower mitochondrial respiration and has higher glycolysis for ATP generation [126, 127]. This, in turn, increases the glucose needs. That is why, the tumor develops, proliferates, and metastasize through angiogenesis and vascularization [126, 127].

GBM has also different electrical characteristics. Its conductivity and permeability values are higher than other tumors and brain tissue [130].

With corona virus disease 2019 (COVID-19) virus pandemic, we can observe the enormous load on the medical system overall. Most of the medical staff are busy dealing with the COVID-19 patients and the hospitals are releasing other patient to make room for COVID-19 patients. As a result, it is almost impossible to access to common medical services, let alone an advanced medical imaging.

With the social distancing rules and hardened access to medical services, one can foresee the rise in distant medical services after this pandemic. With further expectations of second and third waves of pandemic in the upcoming winter months, the authors believe many countries with adopt new principles in the health care and social services. On the social side, the social trauma will echo through our near future and people will avoid unnecessary social contacts. This further emphasizes the importance of alternative solutions by use of new techniques technology brings forth and new approaches to medical services.

Therefore, we propose the use of mobile phones to detect GBM and alike brain tumors in their early stages [131]. But unlike the breast cancer case, the tumor and the tissue electrical properties are closer to each other [131].

We have used a mobile phone semi-fixed on the side of the head. A hypothetical tumor in ellipsoid shape with the size $1 \times 1.6 \times 1$ cm a-b-c radii is proposed as an early stage GBM. We have modified the IEEE SAR phantom head model with the addition of the GBM tumor. They have simulated the EM thermal effects for the mobile phone use in Finite Element Method (FEM) for two different output levels, in six different depth, and six different lateral positions. The findings on the surface temperature change, normal tissue temperature change, and tumor tissue temperature change are presented. A second group of simulations have been simulated to compare the breast and brain cancer detection scenarios [132].

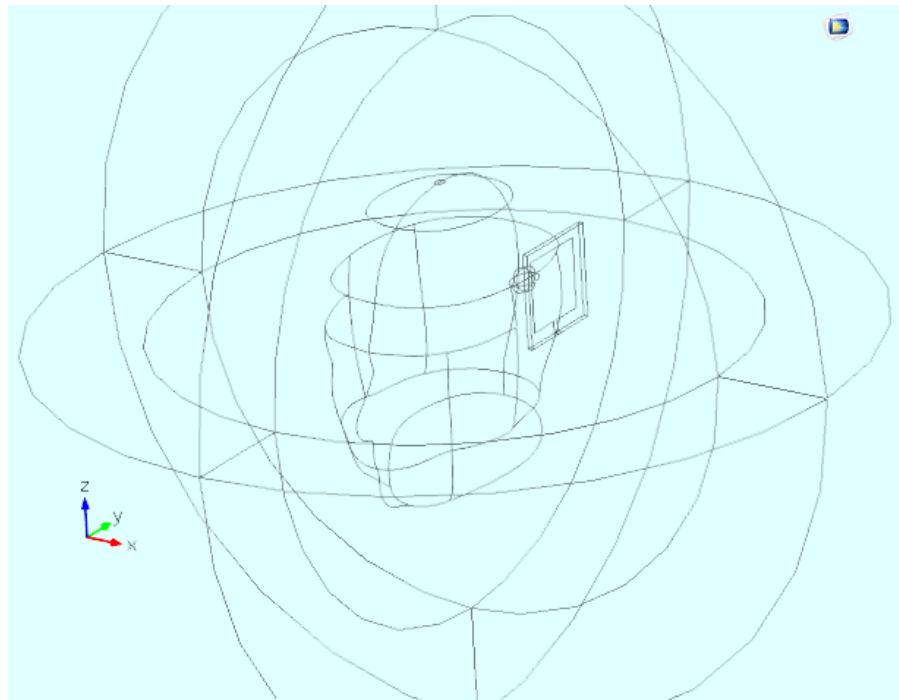


Figure 7.22. Modified IEEE SAR model with GBM tumor.

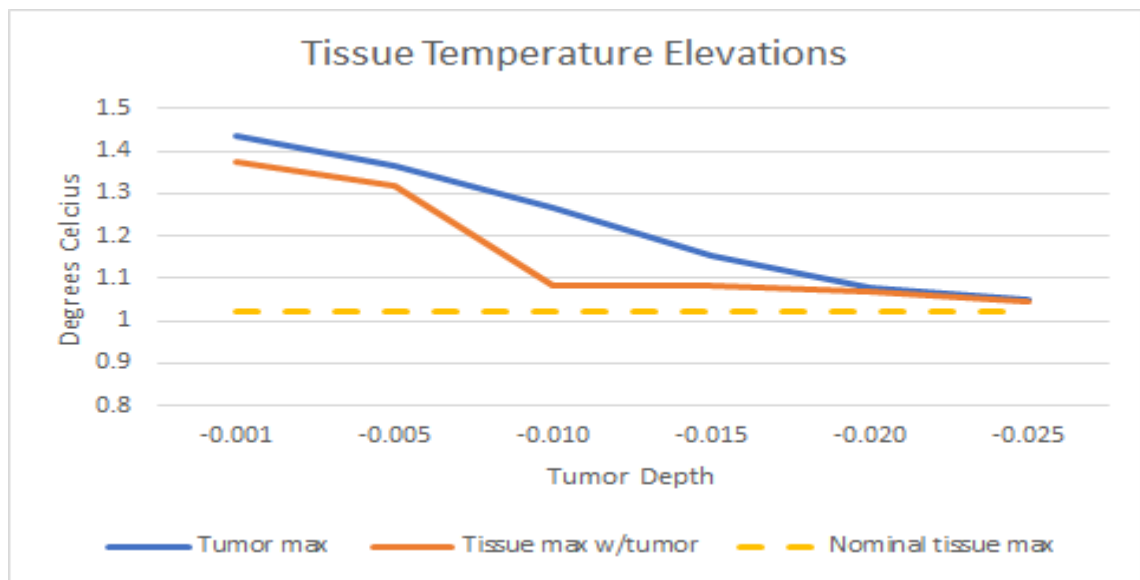


Figure 7.23. Tissue temperature elevations with changing tumor depth at lower power EM exposure.

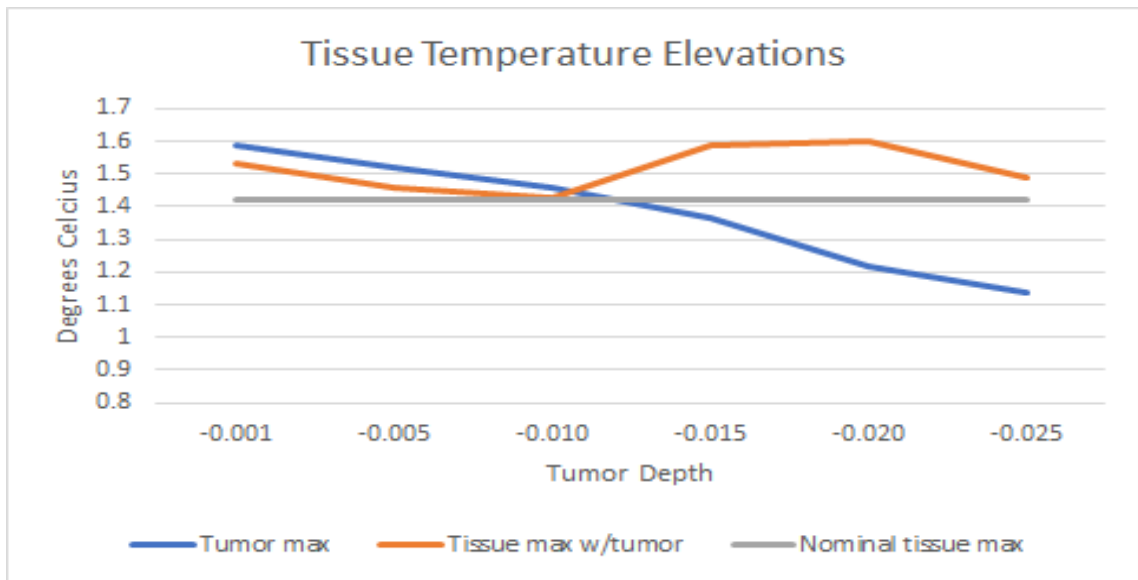


Figure 7.24. Tissue temperature elevations with changing tumor depth at higher power EM exposure.

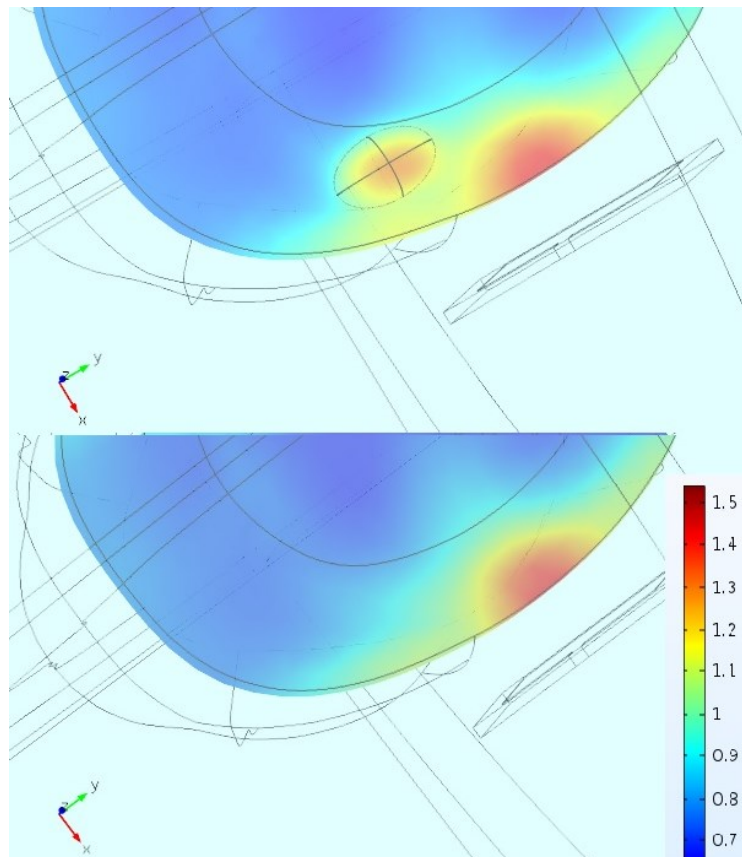


Figure 7.25. Temperature elevation comparison with tumor above and without tumor below at higher power EM exposure.

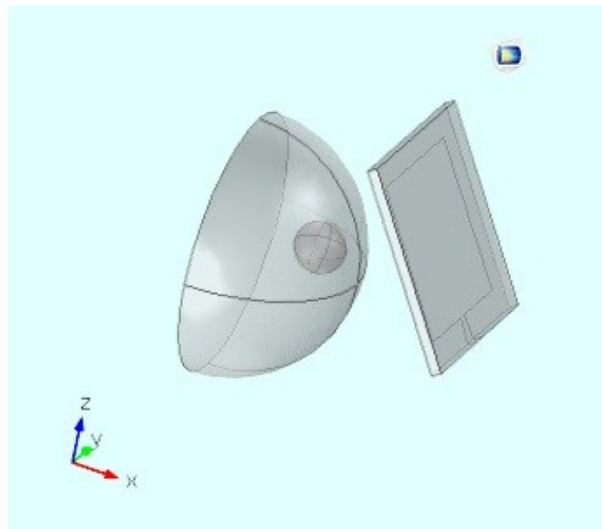


Figure 7.26. Breast model with tumor.

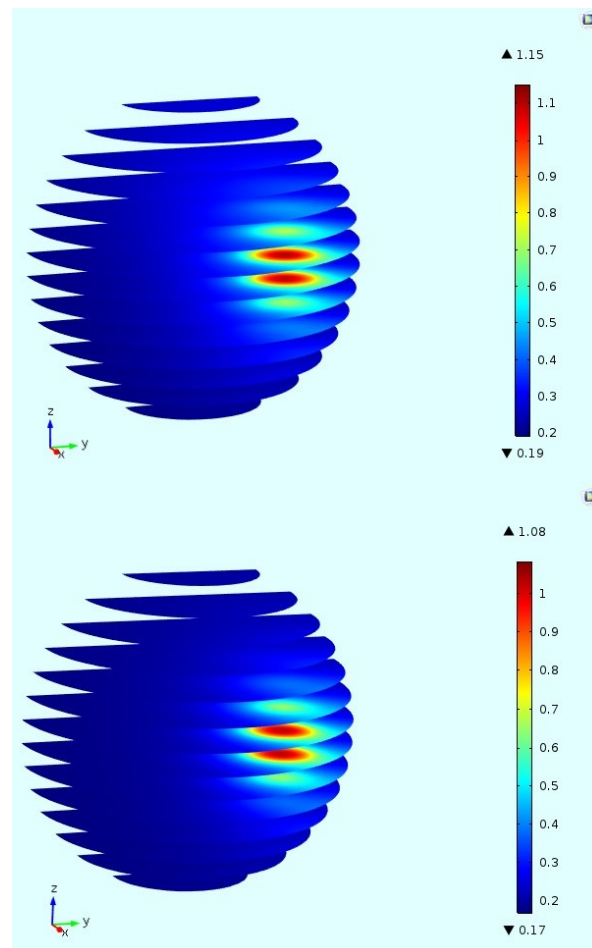


Figure 7.27. Temperature elevation comparison in breast with tumor with higher power (above) and lower power (below) EM exposure.

The tissue temperature elevations for lower and higher power levels are depicted in Figure 7.23 and 7.24 for the aligned exposure onto the tumor. The change in tumor maximum temperature profile with depth and with shift on the antenna axis are shown in Figure 7.25. The tumor temperature elevations are not mirror symmetrical since the head model is not mirror-symmetrical both shape-wise and tissue-wise. For the lower power scenario, the existence of tumor increases the tissue temperature in a diminishing fashion up to 25 mm. Beyond this point the tumor temperature and the tissue maximum temperature converge to their nominal metabolic elevated temperature and maximum tissue temperature under EM exposure without tumor, respectively (Figure 7.23). For the higher power scenario, the existence of tumor increases the tissue maximum temperature in an increasing fashion between 10 to 25 mm (Figure 7.24). The higher power exposure increases both tissue and tumor temperature, but the tissue absorbs more power as the tumor is placed deeper.

We have simulated the second model (Figure 7.26) for comparison reasons. Our figures in temperatures were higher both in absolute numbers and in elevations because of metabolic rate definitions compared to Kunter et al [115]. The rather homogenous structure of breast tissue compared to brain and the higher difference in dielectric values of breast tissue and the tumor have made it more visible and detectable as can be seen in Figure 7.27.

8. DISCUSSION OF OVERALL RESULTS AND CONCLUSIONS

All in all, FEM simulation of concurrent radio utilization is not an easy task. Utilizing realistic parameters, we have achieved sensible results for all scenarios and simulations. In doing so, we have gone through all specifications of 4G/LTE and their corresponding bands. This was the very reason behind choosing 800, 900, 1800, 2100, 2600 and 2600 MHz together with fundamental WI-FI at 2450 MHz. Setting the dynamic parameters for separate frequency bands and for separate tissue areas were also providing a higher accuracy.

In our first group of simulations we have performed, one can see that concurrent radio unit utilization of UEs can trigger elevated temperatures around the ear for the scenario where a tethering mode UE (WI-FI is active) is utilized at the same time for a speech call. And in different usage scenarios certain parts of the head are more exposed than other part.

With the field measurements of multi-technology multi-operator urban BS sites, we have found serious occupational issues, which may pose certain discomfort in the short run and may cause health problems in the long run.

In the second group of simulations we have performed, we have used modified IEEE SAR model according to the target area we wanted to study. In these simulations, we have not only taken the initial conditions of different tissue layers of the eye with their nominal temperatures into account, but also defined specific metabolic rates. In the VR headset EM exposure from CDR on the eye simulation with the modified IEEE model, we have calculated a temperature elevation of 0.7 °C. One can easily neglect the small nature of the value while the normal corneal operational temperature of human eye is around 34.3 °C. So even a slight seemingly change as low as 0.7 °C is critically important, and our findings are an order of magnitude higher, which is around 3.4 °C.

Last but not the least, the simulations in section 7.3 and 7.4 converge on an important aspect. The total body endocrine system is mainly controlled by HPA axis. An oblique

antenna usage with slight look-down position has a direct path through nasal path into pituitary gland, hypothalamus and even to pineal gland. The first two are the main controller of the whole endocrine system with HPA axis. An EM effect on the HPA axis may dramatically affect the total body functions.

8.1. Contributions

In our FEM simulations, we have first time performed CDR scenarios with time-dependent solutions for VR environment with tissue specific EM and metabolic parameters and tissue specific initial conditions. Time-dependent simulation approach has provided us the convergence time of the heating effect for the surface and for inner tissue separately, where the latter is more important for possible heat stress effects into the brain tissue.

In following simulation set-ups, we have addressed this very possibility for the non-thermal effect. The statistically stable clinic and epidemiological non-thermal effects of cellular phone usage on salivary glands are extrapolated onto the HPA axis. The hypothalamus, pituitary, and pineal glands control the circadian rhythm and sustain homeostasis of human body. Only invasive surgical methods can be governed for the clinical results. Therefore, the objective of extrapolating the known response of salivary glands to mobile phone usage over the intracranial glands of hypothalamus, pituitary and pineal glands by simulations has been first time achieved with this dissertation.

This dissertation has opened the way for reconsideration of regulations for finer EMR protection for occupational purposes. Our model modification approach is very instrumental as in the eye and HPA case. Taking into consideration of the fast advent of new technologies and the slow preparation of regulations and time taking epidemiological studies, the IEEE SAR SAM model modification approach can bridge the results of different disciplines of the academia into meaningful recommendations and reasonable exposure limits and regulations within reasonable time.

8.2. Future Path

EMR non-thermal effects should be linked with some energy-time relations. The cooling mechanisms of the body can remove the extensive heat, but the effects are found with stable statistics as in the salivary gland case. This requires a new mathematical approach to the subject. SAR alone is definitely not enough. Miniscule EMF can have subtle effects on human metabolism with ICR, NMR, and so on. So, a mechanism based on the external energy exposure in certain regions having the effects in terms of energy, electrical forces, magnetic forces or any of their combination should be matched with the empirical results of the different branches of academia.

REFERENCES

1. Zhang, J., A. Sumich, and G. Y. Wang, “Acute effects of radiofrequency electromagnetic field emitted by mobile phone on brain function”, *Bioelectromagnetics*, Vol. 38, pp. 329-338, 2017.
2. Yee, K., “Numerical solution of initial boundary value problems involving Maxwell's equations in isotropic media”, *IEEE Transactions on Antennas and Propagation*, Vol. 14, No. 3, pp. 302-307, 1966.
3. Harrington, R. F., “Matrix methods for field problems”, *Proceedings of the IEEE*, Vol. 55, No. 2, pp. 136-149, 1967.
4. Weiland, T., “A discretization model for the solution of Maxwell's equations for six-component fields”, *Archiv für Elektronik und Uebertragungstechnik*, Vol. 31, pp. 116-120, 1977.
5. Courant, R., “Variational methods for the solution of problems of equilibrium and vibrations”, *Bulletin of the American Mathematical Society*, Vol. 49, pp. 1-23, 1943.
6. Prasad, M., P. Kathuria, P. Nair, A. Kumar, and K. Prasad, “Mobile phone use and risk of brain tumours: a systematic review of association between study quality, source of funding, and research outcomes”, *Neurological Sciences*, Vol. 38, No. 5, pp. 797-810, 2017.
7. Grudzinski, E., H. Trzaska, *Electromagnetic Field Standards and Exposure Systems*, SciTech Publishing, New Jersey, 2014.
8. Dlugosz, T., H. Trzaska, “Proximity Effects in the Near Field EMF Metrology”, *IEEE Trans. on Instrumentation and Measurement*, Vol. 3, No. 58, pp. 626-630, 2009.

9. Dlugosz, T., H. Trzaska, “How to Measure in the Near Field and in the Far Field”, *Communication and Network*, Vol. 2, No. 1, pp. 65-68, 2010.
10. Uluaydın, N. K., T. Dlugosz, S. Ş. Şeker, “Electromagnetic radiation exposure of multioperator co-sited urban base stations”, *Turkish Journal of Electrical Engineering and Computer Science*, Vol. 27, No. 4, pp. 3077-3087, 2019.
11. Keeton, W. T., “Magnets interfere with pigeon homing”, *Proceedings of the National Academy of Sciences*, Vol. 68, No.1, pp. 102-106, 1971.
12. Vanselow, K. H., K. Ricklefs, and F. Colijn, “Solar driven geomagnetic anomalies and sperm whale (*Physeter macrocephalus*) strandings around the North Sea: an analysis of long term datasets”, *Open Maritime Biology Journal*, Vol. 3, pp. 89–94, 2009.
13. Goodman, R., A. S. Henderson, “Exposure of salivary gland cells to low-frequency electromagnetic fields alters polypeptide synthesis”, *Proceedings of the National Academy of Sciences of the United States of America*, Vol. 85, pp. 3928-3932, 1988.
14. Burda, H., S. Begall, J. Černevý, J. Neef, and P. Nemeč, “Extremely low-frequency electromagnetic fields disrupt magnetic alignment of ruminants”, *Proceedings of the National Academy of Sciences of the United States of America*, Vol. 106, No. 14, 2009.
15. Wegner, R. E., S. Begall, and H. Burda, “Magnetic compass in the cornea: Local anaesthesia impairs orientation in a mammal”, *Journal of Experimental Biology*, Vol. 209, pp. 4747–4750, 2006.
16. Arrhenius, S., “Cosmic influences on physiological phenomena”, *Skandinavisches Archiv Für Physiologie*, Vol. 8, p. 367, 1898.

17. Andrault, D., J. Monteux, M. Le Bars, and H. Samuel, “The deep Earth may not be cooling down”, *Earth and Planetary Science Letters*, Vol. 443, pp.195-203, 2016.
18. Schumann, W. O., “On the damping of electromagnetic self-oscillations in the system earth–air–ionosphere”, *Zeitschrift für Naturforschung*, Vol. 7, pp. 149-154, 1952.
19. Schumann, W. O., H. König, “Über die Beobachtung von Atmosphericis bei geringsten Frequenzen”, *Naturwissenschaften*, Vol. 41, No. 8, pp. 183–184, 1954.
20. König, H.L., F. A. Popp, G. Becker, and W. Peschka, *Electromagnetic Bio-information*, Urban and Schwarzenberg, Munich, 1979.
21. Cajochen, C., S. Altanay-Ekici, M. Münch, S. Frey, V. Knoblauch, and A. Wirz-Justice, “Evidence that the lunar cycle influences human sleep”, *Current Biology*, Vol. 23, No. 15, pp. 1485-1488, 2013.
22. Alabdulgader, A., R. McCraty, M. Atkinson, Y. Dobyms, A. Vainoras, M. Ragulskis, and V. Stolc, “Long-term study of heart rate variability responses to changes in the solar and geomagnetic environment”, *Scientific Reports*, Vol. 8, No. 1, pp. 1-14, 2018.
23. Dimitrova, S., “Relationship between human physiological parameters and geomagnetic variations of solar origin”, *Advances in Space Research*, Vol. 37, No. 6, pp. 1251-1257, 2006.
24. Nina, A., M. Radovanović, B. Milovanović, A. Kovačević, J. Bajčetić, and L.Č. Popović, “Low ionospheric reactions on tropical depressions prior hurricanes”, *Advances in Space Research*, Vol. 60, No. 8, pp.1866-1877, 2017.

25. Canbay, C., "The essential environmental cause of multiple sclerosis disease", *Progress In Electromagnetics Research*, Vol. 101, pp. 375-391, 2010.
26. Papathanasopoulos, P., P. Preka-Papadema, A. Gkotsinas, N. Dimisianos, A. Hillaris, C. Katsavrias, G. Antonakopoulos, X. Moussas, E. Andreadou, V. Georgiou, and P. Papachristou, "The possible effects of the solar and geomagnetic activity on multiple sclerosis", *Clinical Neurology and Neurosurgery*, Vol. 146, pp. 82-89, 2016.
27. Zhadin, M. N. "Review of Russian literature on biological action of DC and low-frequency AC magnetic fields." *Bioelectromagnetics*, Vol. 22, No. 1, pp. 27-45, 2001.
28. Pivovarenko, Y., "±Water: Demonstration of Water Properties, Depending on its Electrical Potential", *World Journal of Applied Physics*, Vol. 3, No. 1, pp. 13-18, 2018.
29. Dobrzyńska, I., E. Skrzydlewska, and Z. A. Figaszewski, "Changes in electric properties of human breast cancer cells", *The Journal of Membrane Biology*, Vol. 246, No. 2, pp. 161-166, 2013.
30. Gascoyne, P. R., X. B. Wang, Y. Huang, and F. F. Becker, "Dielectrophoretic separation of cancer cells from blood", *IEEE Trans. on Industry Applications*, Vol. 33, No. 3, pp. 670-678, 1997.
31. Garner, A. L., G. Chen, N. Chen, V. Sridhara, J. F. Kolb, R. J. Swanson, S. J. Beebe, R. P. Joshi, and K. H. Schoenbach, "Ultrashort electric pulse induced changes in cellular dielectric properties", *Biochemical and Biophysical Research Communications*, Vol. 362, No. 1, pp. 139-144, 2007.
32. Chernet, B.T., D.S. Adams, M. Lobikin, and M. Levin, "Use of genetically encoded, light-gated ion translocators to control tumorigenesis", *Oncotarget*, Vol. 7, No. 15, p. 19575, 2016.

33. Marlow, M. S., J. Dogan, K. K. Frederick, K. G. Valentine, and, A. J. Wand, “The role of conformational entropy in molecular recognition by calmodulin”, *Nature Chemical Biology*, Vol. 6, No. 5, p. 352, 2010.
34. Kasinath, V., K. G. Valentine, and A. J. Wand, “A ¹³C labeling strategy reveals a range of aromatic side chain motion in calmodulin”, *Journal of the American Chemical Society*, Vol. 135, No. 26, pp. 9560-9563, 2013.
35. Özkucur, N., S. Perike, P. Sharma, and R. H. Funk, “Persistent directional cell migration requires ion transport proteins as direction sensors and membrane potential differences in order to maintain directedness”, *BMC Cell Biology*, Vol. 12, No. 1, p. 4, 2011.
36. Adams, D. S., M. Levin, “Endogenous voltage gradients as mediators of cell-cell communication: strategies for investigating bioelectrical signals during pattern formation”, *Cell and Tissue Research*, Vol. 352, No. 1, pp .95-122, 2013.
37. Bolzoni, F., S. Giraud, L. Lopiano, B. Bergamasco, M. Fasano, and P. R. Crippa, “Magnetic investigations of human mesencephalic neuromelanin”, *Biochimica et Biophysica Acta (BBA)-Molecular Basis of Disease*, Vol. 1586, No. 2, pp. 210-218, 2002.
38. Nicolaus, B. J., “A critical review of the function of neuromelanin and an attempt to provide a unified theory”, *Medical Hypotheses*, Vol. 65, No. 4, pp. 791-796, 2005.
39. Ivanhoe, F., “Coevolution of Human Brain Size and Paleolithic Culture in the Northern Hemisphere: Relation to Geomagnetic Intensity”, *Journal of Bioelectricity*, Vol.1, No. 1, pp. 13-57, 1982.
40. Ivanhoe, F., and E. A. Hammel, “Macrodonia in Pleistocene humans from Europe as a feature of physiological acromegalosis: association with

- geomagnetic dipole field intensity”, *Human Evolution*, Vol. 5, No. 1, pp. 21-53, 1990.
41. Levin, M., “Bioelectromagnetics in morphogenesis”, *Bioelectromagnetics*, Vol. 24, No. 5, pp. 295-315, 2003.
 42. Teixeira, P. D., G. C. Couto, I. C. Furigo, E. O. List, J. J. Kopchick, and J. Donato Jr., “Central growth hormone action regulates metabolism during pregnancy”, *American Journal of Physiology-Endocrinology and Metabolism*, Vol. 317, No. 5, pp. E925-E940, 2019.
 43. Zhang, B., W. Song, P. Pang, Y. Zhao, P. Zhang, I. Csabai, G. Vattay, and S. Lindsay,” Observation of giant conductance fluctuations in a protein”, *Nano Futures*, Vol. 1, No. 3, p.035002, 2017.
 44. Liboff, A. R., “Ion cyclotron resonance: Geomagnetic strategy for living systems?”, *Electromagnetic Biology and Medicine*, Vol. 38, No. 2, pp.143-148, 2019.
 45. Liboff, A. R., “Toward an electromagnetic paradigm for biology and medicine”, *Journal of Alternative & Complementary Medicine*, Vol. 1, No. 10, pp. 41-47, 2004.
 46. Liboff, A. R., *Bioengineering and biophysical aspects of electromagnetic fields*, 3rd ed., CRC Press, New York, 2007.
 47. Liboff, A. R., “The Warburg hypothesis and weak ELF biointeractions”, *Electromagnetic Biology and Medicine*, No. 14, pp. 1-4, 2020.
 48. Mukherjee, S., *Analytical Modeling of Heterogeneous Cellular Networks*, Cambridge University Press, New York, 2014.

49. Ghosh, A. J. Zhang, J. G. Andrews, and R. Muhamed, *Fundamentals of LTE*, Pearson Education, Massachusetts, 2010.
50. Calderón, C., D. Addison, T. Mee, R. Findlay, M. Maslanyj, E. Conil, H. Kromhout, A.K. Lee, M.R. Sim, M. Taki, and N. Varsier, “Assessment of extremely low frequency magnetic field exposure from GSM mobile phones”, *Bioelectromagnetics*, Vol. 35, No. 3, pp. 210-221, 2014.
51. Pedersen, G. F., J. B. Andersen, “RF and ELF exposures from cellular phone handsets: TDMA and CDMA systems”, *Radiation Protection Dosimetry*, Vol. 83, No. 1-2, pp. 131-138, 1999.
52. Gunnarsson, F., F.Gustafsson, “Control theory aspects of power control in UMTS”, *Control Engineering Practice*, Vol. 11, No. 10, pp. 1113-1125, 2003.
53. Wannstrom, J., *Carrier Aggregation Explained*, 2013, <http://www.3gpp.org/technologies/keywords-acronyms/101-carrier-aggregation-explained> , last accessed on 25 September 2020.
54. ETSI, *LTE; Evolved Universal Terrestrial Radio Access (E-UTRA); User Equipment (UE) radio transmission and reception (3GPP TS 36.101 version 13.2.1 Release 13)*, 2016, http://www.etsi.org/deliver/etsi_ts/136100_136199/136101/13.02.01_60/ts_136101v130201p.pdf , last accessed on 25 September 2020.
55. Uluaydin, N. K., S. S. Seker, and A. Y. Citkaya, “Application of EM Broadband Backlobe Absorber for Antennas”, *31st International Review of Progress in Applied Computational Electromagnetics (ACES)*, Williamsburg, March 22-26, IEEE, 2015.
56. Turkish Regulation: *Elektronik Haberleşme Cihazlarından Kaynaklanan Elektromanyetik Alan Şiddetinin Uluslar Arası Standartlara Göre Maruziyet Limit Değerlerinin Belirlenmesi, Kontrolü ve Denetimi Hakkında Yönetmelik*,

2011, no. 27912 <http://www.mevzuat.gov.tr/> , last accessed on 25 September 2020.

57. International Commission on Non-Ionizing Radiation Protection, ICNIRP, “Guidelines for Limiting Exposure to Time-Varying Electric, Magnetic, and Electromagnetic Fields (Up To 300 GHz)”, *Health Physics*, Vol. 74, No. 4, pp. 494-522, 1998.
58. International Commission on Non-Ionizing Radiation Protection, ICNIRP, “Guidelines for limiting exposure to electromagnetic fields (100 kHz to 300 GHz)”, *Health Physics*, Vol. 118, No. 5, pp. 483-524, 2020.
59. Pall, M. L., “Microwave frequency electromagnetic fields (EMFs) produce widespread neuropsychiatric effects including depression”, *Journal of Chemical Neuroanatomy*, Vol. 75, pp. 43-51, 2016.
60. Maxwell, J. C., “VIII. A dynamical theory of the electromagnetic field.” *Philosophical transactions of the Royal Society of London*, Vol. 155, pp. 459-512, 1865.
61. Malmivuo J., R. Plonsey, *Bioelectromagnetism - Principles and Applications of Bioelectric and Biomagnetic Fields*, Oxford University Press, New York, 1995.
62. Hirata, A., M. Morita, and T. Shiozawa, “Temperature increase in the human head due to a dipole antenna at microwave frequencies”, *IEEE Trans. on Electromagnetic Compatibility*, Vol. 45, No. 1, pp. 109-116, 2003.
63. Pennes, H. H., “Analysis of tissue and arterial blood temperatures in the resting human forearm”, *Journal of Applied Physiology*, Vol. 1, No. 2, pp.93-122, 1948.
64. Babuška, I., U. Banerjee, and J. E. Osborn, “Generalized finite element methods—main ideas, results and perspective”, *International Journal of Computational Methods*, Vol. 1, No. 01, pp. 67-103, 2004.

65. Autuori B., K. Bruyère-Garnier, F. Morestin, M. Brunet, J. P. Verriest, “Finite element modeling of the head skeleton with a new local quantitative assessment approach”, *IEEE Trans. on Biomedical Engineering*, Vol. 53, No. 7, pp. 1225-1232, 2006.
66. Weil C. M., “Absorption Characteristics of Multilayered Sphere Models Exposed UHF/Microwave Radiation”, *IEEE Transactions*, Vol. 22, No. 6, 1994.
67. Stratton J. A., *Electromagnetic Theory*, McGraw Hill, New York, 1941.
68. Van der Hulst, H.C., *Light Scattering by Small Particles*, Dover Publications, New York, 1981.
69. C95.1-1991. IEEE standard for safety levels with respect to human exposure to radio frequency electromagnetic fields, 3 kHz to 300 GHz, IEEE standard, 1991 (revised version 2005).
70. Beard, B.B., W. Kainz, “Review and standardization of cell phone exposure calculations using the SAM phantom and anatomically correct head models”, *Biomedical Engineering Online*, Vol. 3, No. 1, p. 34, 2004.
71. Durney, C.H., D.A. Christensen, *Basic Introduction to Bioelectromagnetics*, CRC Press LLC, New York, 2000.
72. Federal Communications Commission (FCC), *Body Tissue Dielectric Parameters*, 2020, <https://transition.fcc.gov/oet/rfsafety/dielectric.html> , last accessed on 25 September 2020.
73. The Foundation for Research on Information Technologies in Society (ITIS), *Tissue Properties*, 2020, <https://itis.swiss/virtual-population/tissue-properties/database/dielectric-properties/> , last accessed on 25 September 2020.

74. Schmid, G., G. Neubauer, and P. R. Mazal, “Dielectric properties of human brain tissue measured less than 10 h postmortem at frequencies from 800 to 2450 MHz”, *Bioelectromagnetics*, Vol. 24, No. 6, pp. 423-430, 2003.
75. Levoy M., *The Stanford volume data archive* (MRI data originally from Univ. of North Carolina), 2014, <http://graphics.stanford.edu/data/voldata/> , [25 September 2020].
76. Baltrėnas P., R. Buckus, “Measurements and analysis of the electromagnetic fields of mobile communication antennas”, *Measurement*, Vol. 46, No. 10, pp. 3942-3949, 2013.
77. Haipeng Z., Q. Zheng, Test for electromagnetic environment of mobile communication base station. In: *Electromagnetic Compatibility, IEEE 2016 Asia-Pacific International Symposium*; Shenzhen, China; 2016. pp. 1164-1167.
78. Dyer B., *Human Eye Model*, 2011, <https://grabcad.com/library/human-eye-model> , last accessed on 25 September 2020.
79. T. Sakai, R. Yoshida, H. Tamaki et al., “Electrodermal activity based study on the relationship between visual attention and eye blink”, *9th International Conference In Sensing Technology (ICST)*, Auckland, New Zealand, , pp. 596-599, IEEE, 2015.
80. Yoshida, R., T. Sakai, Y. Ishi, T. Nakayama, T. Ogitsu, H. Takemura, E. Yamaguchi, S. Inagaki, Y. Takeda, M. Namatame, and M. Sugimoto, “Electrodermal activity-based feasibility study on the relationship between attention and blinking”, *International Journal on Smart Sensing and Intelligent Systems*, Vol. 9, No. 1, pp.21-31, 2016.
81. Zaini, N. H., M. Z. Azemin, M. H. Ithnin, and M. I. Tamrin, “Short Term Effect of Virtual Reality Headset on Blink Rate and Inter-Blink Interval”, *Journal of Engineering and Science Research*, Vol. 4, No. 1, 2020.

82. Maffei, A., A. Angrilli, “Spontaneous blink rate as an index of attention and emotion during film clips viewing”, *Physiology & Behavior*, Vol. 204, pp. 256-263, 2019.
83. Ledger, H., “The effect cognitive load has on eye blinking”, *The Plymouth Student Scientist*, Vol. 6, pp. 206-223, 2013.
84. Schlote, T., G. Kadner, and N. Freudenthaler, “Marked reduction and distinct patterns of eye blinking in patients with moderately dry eyes during video display terminal use”, *Graefe's Archive for Clinical and Experimental Ophthalmology*, Vol. 242, pp. 306-312, 2004.
85. Haak, M., S. Bos, S. Panic, and L. J. M. Rothkrantz, “Detecting stress using eye blinks and brain activity from EEG signals”, In: *Proceedings of the 1st Driver Car Interaction and Interface*, November 26-28, Eurosis, Oostende, 2009.
86. De Santis, V., M.Feliziani, “Effects of thermoregulatory mechanisms on the eye thermal elevation produced by intense RF exposures”, *International Symposium on Electromagnetic Compatibility*, Detroit, August 18-22, IEEE, Hamburg, 2008.
87. Opie, N.L., A. N. Burkitt, H. Meffin, and D. B. Grayden, “Heating of the eye by a retinal prosthesis: modeling, cadaver and in vivo study”, *IEEE Trans. on Biomedical Engineering*, Vol. 59, pp. 339-345, 2012.
88. Diao, Y., S. W. Leung, Y. He, W. Sun, K. H. Chan, Y. M. Siu, and R. Kong, “Detailed modeling of palpebral fissure and its influence on SAR and temperature rise in human eye under GHz exposures”, *Bioelectromagnetics*, Vol. 37, No. 4, pp. 256-263, 2016.

89. Ng, E. Y. K., E. H. Ooi, "FEM simulation of the eye structure with bioheat analysis", *Computer Methods and Programs in Biomedicine*, Vol. 82, pp. 268-276, 2006.
90. Schmid, G., G. Neubauer, P. R. Mazal, "Dielectric properties of human brain tissue measured less than 10 h postmortem at frequencies from 800 to 2450 MHz", *Bioelectromagnetics*, Vol. 24, pp. 423-430, 2003.
91. Ooi, E. H., W. T. Ang, E. Y. K. Ng, "Bioheat transfer in the human eye: a boundary element approach", *Engineering Analysis with Boundary Elements*, Vol. 31, 494-500, 2007.
92. Karampatzakis, A., T. Samaras, "Numerical modeling of heat and mass transfer in the human eye under millimeter wave exposure", *Bioelectromagnetics*, Vol. 34, pp. 291-299, 2013.
93. Li, C., Q. Chen, Y. Xie, and T. Wu, "Dosimetric study on eye's exposure to wide band radio frequency electromagnetic fields: Variability by the ocular axial length", *Bioelectromagnetics*, Vol. 35, pp. 324-336, 2014.
94. Gandhi, O.P., "Yes the children are more exposed to radiofrequency energy from mobile telephones than adults", *IEEE Access*, Vol. 3, pp. 985-988, 2015.
95. Mohammed, B., J. Jin, A. M. Abbosh, K. S. Bialkowski, M. Manoufali, and S. Crozier, "Evaluation of Children's Exposure to Electromagnetic Fields of Mobile Phones Using Age-Specific Head Models With Age-Dependent Dielectric Properties", *IEEE Access*, Vol. 5, pp. 27345-27353, 2017.
96. Sangün, Ö., B. Dündar, S. Çömlekçi, and A. Büyükgebiz, "The Effects of Electromagnetic Field on the Endocrine System in Children and Adolescents", *Pediatric Endocrinology Reviews*, Vol. 13, pp. 531-45, 2015.

97. de Siqueira, E. C., F. T. A. de Souza, R. S. Gomez, C. C. Gomes, and R. P. de Souza, "Does cell phone use increase the chances of parotid gland tumor development? A systematic review and meta-analysis," *Journal of Oral Pathology & Medicine*, Vol. 46, No. 7, pp. 480-483, 2017.
98. Siqueira, E. C., F. T. A. de Souza, E. Ferreira, R. P. Souza, S. C. Macedo, E. Friedman, M. V. Gomez, C. C. Gomes, and R. S. Gomez, "Cell phone use is associated with an inflammatory cytokine profile of parotid gland saliva", *Journal of Oral Pathology & Medicine*, Vol. 45, No. 9, pp. 682-686, 2016.
99. Shivashankara, A. R., J. Joy, V. Sunitha, M.P. Rai, S. Rao, S. Nambranathayil, and M. S. Baliga, "Effect of cell phone use on salivary total protein, enzymes and oxidative stress markers in young adults: a pilot study", *Journal of Clinical and Diagnostic Research*, Vol. 9, No. 2, p.BC19, 2015.
100. Arbabi-Kalati, F., S. Salimi, A. Vaziry-Rabiee, and M. Noraei, "Effect of mobile phone usage time on total antioxidant capacity of saliva and salivary immunoglobulin A", *Iranian Journal of Public Health*, Vol. 43, No. 4, p. 480, 2014.
101. Aydogan, F., İ. Unlu, E. Aydin, N. Yumusak, E. Devrim, E. E. Samim, E. Ozgur, V. Unsal, A. Tomruk, G. G. Ozturk, and N. Seyhan, "The effect of 2100 MHz radiofrequency radiation of a 3G mobile phone on the parotid gland of rats", *American Journal of Otolaryngology*, Vol. 36, No. 1, pp.39-46., 2015.
102. Prasad, M., P. Kathuria, P. Nair, A. Kumar, and K. Prasad, "Mobile phone use and risk of brain tumours: a systematic review of association between study quality, source of funding, and research outcomes", *Neurological Sciences*, Vol. 38, No. 5, pp. 797-810, 2017.
103. Bortkiewicz, A., E. Gadzicka, and W. Szymczak, "Mobile phone use and risk for intracranial tumors and salivary gland tumors-A meta-analysis",

International Journal of Occupational Medicine and Environmental Health, Vol. 30, No. 1, pp.27-43, 2017.

104. Grell, Kathrine, K. Frederiksen, J. Schüz, E. Cardis, B. Armstrong, J. Siemiatycki, D. R. Krewski, M. L. McBride, C. Johansen, A. Auvinen, and M. Hours, “The intracranial distribution of gliomas in relation to exposure from mobile phones: analyses from the INTERPHONE study”, *American Journal of Epidemiology*, pp.1-11, 2016.
105. Wang, Y., X. Guo, “Meta-analysis of association between mobile phone use and glioma risk”, *Journal of Cancer Research and Therapeutics*, Vol. 12, No. 8, p. 298, 2016.
106. Al-Qahtani, K., “Mobile Phone Use and the Risk of Parotid Gland Tumors: A Retrospective Case-Control Study”, *The Gulf Journal of Oncology*, Vol. 1, No. 20, pp. 71-78, 2016.
107. Hardell, L., M. Carlberg, “Mobile phone and cordless phone use and the risk for glioma—Analysis of pooled case-control studies in Sweden, 1997–2003 and 2007–2009”, *Pathophysiology*, Vol. 22, No. 1, pp. 1-13, 2015.
108. Carlberg, M., L. Hardell, “Decreased survival of glioma patients with astrocytoma grade IV (glioblastoma multiforme) associated with long-term use of mobile and cordless phones”, *International Journal of Environmental Research and Public Health*, Vol. 11, No. 10, pp. 10790-10805, 2014.
109. Geronikolou, S. A., A. Chamakou, A. Mantzou, G. Chrousos, and C. KanakaGantenbein, “Frequent cellular phone use modifies hypothalamic–pituitary–adrenal axis response to a cellular phone call after mental stress in healthy children and adolescents: A pilot study”, *Science of The Total Environment*, No. 536, pp. 182-188, 2015.

110. Gabriel, S., R. W. Lau, and C. Gabriel, "The dielectric properties of biological tissues: II. Measurements in the frequency range 10 Hz to 20 GHz", *Physics in Medicine & Biology*, Vol. 41, No. 11, p. 2251, 1996.
111. Mandala, M., V. Colletti, L. Sacchetto, P. Manganotti, S. Ramat, Alessandro Marcocci, and L. Colletti, "Effect of bluetooth headset and mobile phone electromagnetic fields on the human auditory nerve", *The Laryngoscope*, Vol. 124, No. 1, pp. 255-259. 2014.
112. Eskander, E. F., S. F. Estefan, and A. A. Abd-Rabou, "How does long term exposure to base stations and mobile phones affect human hormone profiles?", *Clinical Biochemistry*, Vol. 45, No. 1-2, pp. 157-161, 2012.
113. Shahabi, S., I. H. Taji, M. Hoseinnezhaddarzi, F. Mousavi, S. Shirchi, A. Nazari, H. Zarei, and F. Pourabdolhossein, "Exposure to cell phone radiofrequency changes corticotrophin hormone levels and histology of the brain and adrenal glands in male Wistar rat", *Iranian Journal of Basic Medical Sciences*, Vol. 21, No. 12, p. 1269, 2018.
114. Uluaydin, N. K., O. Cerezci, S. Seker, "Can Mobile Phone Usage Affect Hypothalamus-Pituitary-Adrenal Axis Response?.", *10th Annual Computing and Communication Workshop and Conference (CCWC)*, Las Vegas, USA, pp. 773-776, IEEE, 2020.
115. Kunter, F. C., C. Gündüz, and S. S. Seker, "Temperature Increase and Specific Absorption Rate Distribution in Human Breast from Cell Phone Radiation," *Journal of Medical Imaging and Health Informatics*, Vol. 8, No. 6, pp. 1186-1191, 2018.
116. Citkaya, Y., S. S. Seker, "FEM modeling of SAR distribution and temperature increase in human brain from RF exposure", *International Journal of Communication Systems*, Vol. 25, No. 11, pp. 1450-1464, 2012.
117. Sârbu, A., A. Bechet, T. Bălan, D. Robu, P. Bechet, and S. Miclăuş, "Using CCDF statistics for characterizing the radiated power dynamics in the near field

of a mobile phone operating in 3G+ and 4G+ communication standards”, *Measurement*, Vol. 134, pp. 874-887, 2019.

118. Federal Communications Commission (FCC), *Specific Absorption Rate for Cellular Phones*, <https://www.fcc.gov/general/specific-absorption-rate-sar-cellular-telephones> , last accessed on 4 August 2020.
119. World Health Organization (WHO), *Cancer*, https://www.who.int/health-topics/cancer#tab=tab_1 , last accessed on 25 September 2020.
120. Lichtor, T., *Molecular Considerations and Evolving Surgical Management Issues in the Treatment of Patients with a Brain Tumor*, InTech, Rijeka, 2015.
121. Gupta, K., T. C. Burns, “Radiation-induced alterations in the recurrent glioblastoma microenvironment: therapeutic implications”, *Frontiers in Oncology*, Vol. 8, p. 503, 2018.
122. Oei, A. L., L. E. M. Vriend, P. M. Krawczyk, M. R. Horsman, N. A. P. Franken, and J. Crezee, “Targeting therapy-resistant cancer stem cells by hyperthermia”, *International Journal of Hyperthermia*, Vol. 33, No. 4, pp. 419-427, 2017.
123. Repasky, E.A., S. S. Evans, and M. W. Dewhirst, “Temperature matters! And why it should matter to tumor immunologists”, *Cancer Immunology Research*, Vol. 1, No. 4, pp. 210-216, 2013.
124. Grauer, O., M. Jaber, K. Hess, M. Weckesser, W. Schwindt, S. Maring, J. Wölfer, and W. Stummer, “Combined intracavitary thermotherapy with iron oxide nanoparticles and radiotherapy as local treatment modality in recurrent glioblastoma patients”, *Journal of Neuro-oncology*, Vol. 141, No. 1, pp.83-94, 2019.
125. Gupta, R., D. Sharma, “Manganese-Doped Magnetic Nanoclusters for Hyperthermia and Photothermal Glioblastoma Therapy”, *ACS Applied Nano Materials*, Vol. 3, No. 2, pp. 2026-2037, 2020.

126. Salehi, A., M. Paturu, M. Caine, R. Klein, and A.H. Kim, “Laser Therapy Enhances Blood-Brain Barrier and Blood-Tumor Barrier Permeability in a Mouse Model of Glioblastoma”, *Neurosurgery*, Vol. 66, No. Supplement_1, p. nyz310_635, 2019.
127. Benos, L., L. A. Spyrou, and I. E., Sarris, “Development of a new theoretical model for blood-CNTs effective thermal conductivity pertaining to hyperthermia therapy of glioblastoma multiforme”, *Computer Methods and Programs in Biomedicine*, Vol. 172, pp. 79-85, 2019.
128. Zhou, Y., .Y Zhou, T. Shingu, L. Feng, Z. Chen, M. Ogasawara, M.J. Keating, S. Kondo, and P. Huang, “Metabolic alterations in highly tumorigenic glioblastoma cells preference for hypoxia and high dependency on glycolysis”, *Journal of Biological Chemistry*, Vol. 286, No. 37, pp. 32843-32853, 2011.
129. National Brain Tumor Society (NBTS-USA), *Tumor Types: Understanding Brain Tumors*, <https://braintumor.org/brain-tumor-information/understanding-brain-tumors/tumor-types/#glioblastoma-multiforme>, last accessed on 25 September 2020.
130. Louis, D.N., A. Perry, G. Reifenberger, A. Von Deimling, D. Figarella-Branger, W. K. Cavenee, H. Ohgaki, O.D. Wiestler P., Kleihues, and D. W. Ellison, “The 2016 World Health Organization classification of tumors of the central nervous system: a summary”, *Acta Neuropathologica*, Vol. 131, No. 6, pp. 803-820, 2016.
131. Cedars Sinai Center (CSC), *Brain Tumors and Brain Cancer*, <https://www.cedars-sinai.edu/Patients/Health-Conditions/Brain-Tumors-and-Brain-Cancer.aspx>, last accessed on 25 September 2020.
132. Proescholdt, M.A., A. Haj, C. Doenitz, A. Brawanski, Z. Bomzon, and H. S. Hershkovich, “The dielectric properties of brain tumor tissue”, In: American Association for Cancer Research, *Proceedings: AACR Annual Meeting 2019*, Atlanta, March 29-April 3, AACR, Philadelphia, 2019.